Reflective Variable Optical Attenuators

and Fibre Ring Lasers for

Wavelength-Division Multiplexing Systems

LIU He Liang

A thesis submitted in partial fulfillment of the

requirements for the Degree of Doctor of Philosophy

Department of Electrical Engineering,

The Hong Kong Polytechnic University

December, 2005

CERTIFICATE OF ORIGINALITY

I hereby declare that this thesis is my own work and that, to the best of my knowledge

and belief, it reproduces no material previously published or written, nor material which

has been accepted for the award of any other degree or diploma, except where due

acknowledgement has been made in the text.

_____(Signed)

  HE LIANG LIU (Name of student)

ACKNOWLEDGMENTS

ABSTRACT

Wavelength division multiplexing (WDM) optical fibre system is an important enabling technology to fulfill the demands for bandwidth in the modern information age. The main objective of this project is to study novel devices with the potential to enhance the performance of WDM systems. In particular, a novel reflective variable optical attenuator (RVOA) used for dynamic gain equalization (DGE) and fibre lasers based on an entirely new type of erbium-doped fibres with ultrawide tuning range were investigated theoretically and experimentally.

We proposed a new type of RVOA device which could be potentially integrated with arrayed waveguide grating (AWG) to reduce the cost of DGE substantially. Initially, fibre-based RVOAs, fabricated with optical fibre components such as fibre coupler and Faraday rotator mirror, were investigated theoretically and experimentally. Larger attenuation range up to 22 dB was realized for fibre coupler-based ROVA with a Faraday rotator mirror and its polarization-dependent loss is about 0.5 dB. Then polymeric waveguide-based RVOAs were investigated theoretically and experimentally. Using an epoxy Novolak resin as core material and an UV-cured resin (Norland's NOA61) as cladding material, a polymeric waveguide RVOA was successfully fabricated. The dynamic 15 dB attenuation range was achieved and the PDL was less than 0.2 dB. The measured insertion loss of the polymeric waveguide

RVOA was too large (about 18 dB) and was mainly induced by coupling loss, material loss and poor alignment.

In addition, a novel low-loss waveguide crossing design technique based on MMI structure was proposed and investigated by simulations using a two-dimensional beam propagation method. The low-loss waveguide crossing propagation can be achieved when a slab is introduced to the image reformed region of MMI structure, where any perturbations immediately outside the waveguide would have little effect to the propagation of the optical field. The advantage of the new low-loss MMI waveguide crossing technique is shown by comparing with the common taper width waveguide crossing technique. The application of MMI structure in small angle intersection was also demonstrated and angle intersection as small as 20° with low insertion loss (< 0.15 dB) can be realized with MMI structure technology. This technique is very useful in the design of compact RVOA array with high channel-count.

In the second part of the study, fibre ring lasers with continuous wavelength tuning over wide wavelength range and fibre ring lasers with discrete wavelength tuning were investigated. Tunable lasers are important devices in WDM systems because they could be employed as reserved sources and therefore avoiding the need to stock large inventory of lasers to cover the ITU-wavelength grid. In this project, erbium ions doped bismuth oxide glass fibres instead of the common silicate fibres were used. Due to the high solubility of erbium ions in bismuth oxide based erbium-doped fibre

(Bi-EDF), a stable and short-cavity fibre ring laser was realized by employing only 0.85 m of Bi-EDF.   Ultrawide continuous wavelength tuning range over 100 nm was obtained by using a tuning MEMS filter or scanning fibre FP filter.   A very narrow linewidth, single-longitudinal mode fibre ring laser, using an unpumped EDF acting as saturable absorber in the cavity, was realized.   The linewidth of the fibre ring laser was measured by two optical mixing methods and about 1.17 kHz linewidth was measuring by the delayed self-heterodyne technique.

In addition, two types of wavelength-switchable fibre ring laser based on polarization wavelength selection were investigated.   The principle of polarization wavelength selection to attain the switchable function was explained.   The first type employs an unbiased FP-LD to act as the polarization and etalon filter.   Eight lasing wavelengths switchable from 1552.98 nm to 1560.80 nm with a separation of 1.1 nm, which is defined by the FP mode of the FP-LD, were achieved.   The second design used only 0.85 m of Bi-EDF as gain medium.   Thirty-five switching wavelengths can be achieved in the range of 1545 nm to 1573 nm with a wavelength separation of 0.8 nm, which is defined by the free-spectral range of the F-P etalon filter.   The laser exhibits high output power of about 0 dBm, high SMSR better than 45 dB and output power flatness of 3 dB.   Excellent wavelength and power stability of 1 pm and less than 0.15 dB, respectively, were obtained during a 2-hour stability test.

Contents

Contents

Chapter 1

Introduction

1.1 Motivation for the Project

In the modern information age, more and more people use the Internet, consuming large mounts of bandwidth due to increasing data transfers involving voices, images and videos. At the same time, businesses are relying increasingly on Intranets and Internets for their day-to-day operations. Furthermore, the ultimate vision of the information age is that information can be obtained from anywhere at anytime by anyone [1]. All these factors are driving the demand for networks of higher and higher capacities but at lower and lower costs. To fulfill the increasing demands for bandwidth, a wavelength division multiplexing (WDM) optical system is an attractive key technology to invariably reduce the cost of bandwidth [2]. Furthermore, the WDM system provides an economical mean to upgrade its capacity to handle higher bit-rates.

In WDM systems, data are transmitted simultaneously at multiple carrier wavelengths over a single fibre. In the last few years, the number of wavelength was increased

significantly from tens to hundreds. Large inventory of laser sources operating at ITU wavelengths are stored to ensure minimal down time of the service. The most secure WDM system is "one-to-one" protection. This means that a spare laser is kept for each channel wavelength. This is not practical due to the overwhelming cost and large inventory volume. An economical and practical approach is to stock wide wavelength-tunable lasers instead of fixed wavelength DFB lasers. Moreover, with the advent of dynamic optical networks requiring wavelength switching and routing, tunable lasers could play a key role as an enabling technology in optical networks.

Another issue about WDM system is system reach, which is defined as the distance between optical-electrical-optical (OEO) regeneration. In the early generation of WDM systems, system reach is only about five to six spans, which is defined as the distance between two adjacent optical amplifiers. With the rapid development of the WDM systems, ultra long-haul (ULH) system (15 to 20 spans) or extreme long-haul (ELH) system (80 to 100 spans) is needed to reduce the system OEO regeneration [3]. In ULH or ELH systems, many erbium-doped fibre amplifier (EDFA) modules are needed to compensate for fibre loss, which will induce large power difference between different channels (wavelengths) due to the non-uniform spectral gain of EDFA modules. Consequently, some channels will experience low optical signal-to-noise ratio (OSNR), limiting the transmission length of the system. Gain flattening of EDFAs is thus essential to ensure similar OSNR for all wavelength

channels. Equal OSNR for all channels is difficult to attain, particularly over broad wavelength range because the noise figures introduced by EDFAs to the different channels are not equal. In long-haul WDM systems, dynamic gain equalizers (DGEs) are thus required to flatten the gain of EDFAs. DGEs are transmissive optical devices that alter the attenuation of each individual wavelength channel of a WDM system. Dynamic gain equalization is a key technology for ULH or ELH systems. With the advent of dynamic optical networks requiring optical power dynamic control automatically, DGE could be an important enabling technology [4].

The three main objectives in this project are:

(1) to study and to develop wide wavelength tunable fibre lasers. Emphases were placed on wide tunable range to cover the C- and/or L-band wavelength range. A wavelength-tunable fibre ring laser with over 100 nm tuning range was developed in this project by using novel active fibre that based on bismuth oxide glass fibre doped with high concentration of erbium ions.

(2) to develop stable wavelength-switchable fibre lasers. By using the polarization wavelength selection principle, two configurations of switchable fibre ring laser were developed in this project. One fibre ring laser was made with unbiased Fabry-Perot laser diode (FP-LD) and exhibit eight switchable wavelengths. The other fibre ring laser was constructed with polarizer and exhibit 35 switchable wavelengths.

(3) to study and develop a reflective variable optical attenuator (RVOA) that is compatible to array waveguide (AWG) for the DGE application. Fibre optics

components and polymer waveguide technologies were used to realize the novel RVOA. In addition, a novel low-loss waveguide crossing technique was proposed which could be employed to integrate RVOAs to AWG so as to attain multi-channel attenuation adjustment within a single chip.

1.2 Original Achievements

The following original findings and developments were achieved in this research project:

1. Development of a novel RVOA device and its application in DGE. A fibre coupler RVOA was fabricated and its application in DGE was proposed. Then a polymer waveguide RVOA, which can be integrated with AWG to reduce the cost of DGE greatly, was fabricated and its preliminary results were measured.

2. Propose an entirely new low-loss waveguide crossing technique based on multimode interference (MMI) structure. A comparison with the common taper width technique using the two-dimensional beam propagation method (BPM) simulation revealed that our proposed MMI structure waveguide crossing technique offers more benefits for the design of waveguide DGE. Its performance in angle waveguide crossing was also simulated and a small

crossing angle can be obtained.

3. Development of a wide wavelength tunable range fibre ring laser by using a short length of bismuth oxide based erbium-doped fibre (Bi-EDF). Over 100 nm of wavelength tuning range was obtained using a tunable MEMS filter or scanning fibre Fabry-Perot filter in the cavity. A single-longitudinal mode fibre ring laser was realized by employing an unpumped silica-based erbium-doped fibre (Si-EDF) as a saturable absorber. The linewidth of the laser was measured to be about 1.17 kHz by using the delayed self-heterodyne technique.

4. Development of two configurations of wavelength-switchable fibre ring lasers by using the polarization wavelength selection principle. The first configuration used an unbiased FP-LD and the output could be switched between 8 different wavelengths with 1.1 nm spacing and the second used a Fabry-Perot etalon filter, a polarizer, a programmable electric-actuated polarization controller. The laser's output could be switched between 35 different wavelengths with 0.8 nm spacing. Wavelength switching of the two types of lasers was achieved by suitably changing the polarization state inside the cavity.

1.3   Organization of the Thesis

The thesis is organized as follows:

Chapter 1   is the introduction to this research study and thesis.   The motivation of this project and the layout of the thesis are described in this chapter. Also, the original achievements in this research study are also listed.

Chapter 2   covers the studies and experiments of the reflective variable optical attenuator and its application in dynamic gain equalizer.   The background review of different planar light-wave circuit (PLC) variable optical attenuators is explained and then followed by the proposed novel RVOA and its application in DGE.   In the initial stage, fibre coupler-based RVOAs were demonstrated and measured.   Finally, the design and fabrication of polymer waveguide RVOA and its preliminary results were given.

Chapter 3   describes the proposed low-loss waveguide crossing technique.   The principle of the novel low-loss waveguide crossing design technique is explained, simulated and followed by the introduction of MMI structure. The advantages of the novel low-loss waveguide crossing design

technique based on MMI structure are demonstrated by making comparison to the common taper width structure technique. Also included at the end of this chapter is its application in small angle waveguide crossing, which is essential to reduce the premium wafer space and thus the potential to lower manufacturing cost.

Chapter 4   is dedicated to fibre ring lasers and their theoretical modeling and narrow linewidth measurement. Started with a brief background review of fibre ring laser, the theoretical modeling of fibre ring laser is explained. Furthermore the optical mixing techniques to measure the narrow linewidth of fibre ring laser are introduced and theoretical analyzed. Two different laser linewidth measurement techniques, namely the heterodyne method and delayed self-heterodyne method, are explained in detail.

Chapter 5   describes a wide wavelength-tunable fibre ring laser. It begins with a brief description of the characteristics of bismuth oxide based erbium-doped fibres and fusion technique of Bi-EDF to silicate fibres. The experiment and performance of the widely tunable, over 100 nm, fibre ring laser employing tunable MEMS filter and tunable fibre Fabry-Perot filter are reported. The principle and performance of employing unpumped Si-EDF in the ring cavity to realize

single-longitudinal mode operation with a narrow linewidth of about 1.17 kHz, measured by the delayed self-heterodyne technique, are explained.

Chapter 6   describes two types of wavelength-switchable fibre ring laser developed in this project. With the aid of the Jones matrix approach, the polarization wavelength selection principle is explained, which is essential to understand the wavelength switching function. Eight wavelengths switchable fibre ring laser ring using an unbiased FP-LD in the cavity is described. Finally, the use of Bi-EDF to realize short cavity laser that could generates 35 switchable wavelengths is explained.

Chapter 7   outlines the conclusions of this study and several suggestions for further works.

Since RVOA and fibre ring laser are two distinct topics, their research backgrounds and technology overviews are dealt with in separate chapters instead of a single introductory background chapter. The background of RVOA and the work done in this project are described in chapter 2 and 3. The research backgrounds and modeling of fibre ring laser are reported in chapter 4 while the works done in this project are covered in chapter 5 and 6.

References:

1. R. Ramaswami, and K. N. Sivarajan, "Optical Networks-a practical perspective," by Morgan Kaufmann Publishers, Inc. USA, 1998.

2. G. P. Agrawal, "Fiber-Optic Communication Systems," by John Wiley & Sons, Inc. New York, 1997.

3. S. Bahri, and J. Nagel "Third-generation DWDM: extreme long-haul systems," *Lightwave Magazine*, Jul. 2001.

4. M. Li and S. Peng, "Dynamic gain equalization in fiber-optic communication systems" *LEOS 2002, 15th Annual Meeting of the IEEE Lasers and Electro-Optics Society*, vol. 2, pp. 879-880, 10-14 Nov. 2002.

Chapter 2

Reflective Variable Optical Attenuator and Its Application in Dynamic Gain Equalizer

2.1 Introduction

Variable Optical Attenuators (VOAs) are important optical devices used in optical systems. They are commonly used to reduce crosstalk in switching networks by equalizing the signal power levels in wavelength-multiplexed systems to reduce the optical signal-to-noise (OSNR) deterioration. VOAs are also employed to attenuate optical power to prevent saturation of photodetectors or protect them from optical damage [1, 2]. The increasing complexity of wavelength division multiplexing (WDM) optical networks calls for an increasing need for reliable, low cost VOAs that can adjust the power level of the optical signals of all wavelength channels, independently and dynamically, with high accuracy and repeatability. Dynamic gain equalizer (DGE) modules are particularly important for ultra or extremely long-haul WDM transmission systems for the equalization of non-uniform channel power levels of the different wavelength channels. Conventional DGE are usually constructed with two AWG modules and one VOA array inserted between the AWGs [3]. This is

because most VOAs are transmissive devices. However, if reflective VOAs

(RVOAs) are used, then DGE can be attained by using just one AWG module, which

could greatly simplify the design as well as reduce the cost of DGE. Matching

AWGs are no longer needed and the number of optical connections can be halved.

In this chapter, different kinds of reported VOA designs, especially planar light-wave

circuit, which seems to be a more promising technology in VOA design, are reviewed.

The different structures of the newly proposed reflective variable optical attenuator,

for DGE application will also be described in this chapter. Two kinds of RVOA, i.e.

fibre coupler-based RVOA and polymer waveguide RVOA, were fabricated and their

characteristics were measured.

2.2   Review of the VOA Technologies

Many different approaches have been reported for practical implementation of

variable optical attenuators. These include planar light-wave circuit (PLC) VOA

[4-12], micro-electromechanical systems (MEMS) VOA [13-15], Faraday rotators

VOA [16], liquid crystal VOA [17-18] and acousto-optic VOA [19-20]. Since PLC

VOAs have small footprint and can be integrated with other components, it is a more

promising technology for VOA design. In this section, different VOA configurations

integrated on PLC are reviewed. VOA structures comprising a Mach-Zehnder

interferometer (MZI) [4-6], asymmetric Y-branch waveguide [7-9], bending

waveguide [10-11], and higher mode excitation [12] were reported. PLC VOA is usually fabricated using polymer or silica on silicon substrates. Polymeric VOA is particularly attractive due to its low electrical power consumption, low cost and ease of fabrication.

2.2.1   MZI VOA

A common interferometric approach to fabricate VOA involves MZI design based on directional couplers, since it offers the potential for extremely low power consumption. By thermo-optically or electro-optically tuning at least one of the arms to induce a phase shift between the two arms before they recombine, the output optical power can be accurately controlled. Using the polymeric OASIC^{TM} materials from Telephotonics Inc. and using UV photolithography technology, N. S. Lagali fabricated 8-channel VOA arrays based on the MZI approach [4]. The heater was fabricated by depositing a gold layer over the waveguide cladding and subsequent wet etching to define their shape. The chip size for the 8-channel array was 7x20 mm^2, which can be made smaller by designing a more compact MZI structure. Figure 2.1 (a) shows the measured attenuation characteristic for the two outer VOAs. The fibre-to-fibre insertion loss is 1.4-1.8 dB and a dynamic attenuation range larger than 25 dB, with the best device having a range of almost 30 dB. The power consumption of 25 dB attenuation is only about 1.5 mW, which is much lower than MZI-based VOA made on silica-based planar light-wave circuits which exhibit a

power consumption of 0.9 W to introduce 20-dB attenuation [5]. The attenuation of

the VOAs is spectrally flat to within 1 dB over the C-band at all attenuation levels.

The polarization dependent loss was measured to be 0.1 dB at minimum attenuation

and increases to 1.4 dB at maximum attenuation. The 10%-90% rise and fall

response time of the VOA are 7.7 ms and 8.1 ms, respectively, as shown in Figure 2.1

(b). The response time can in general be further reduced by optimizing the optical

layer thicknesses. L. Eldada reported a polymeric VOA with PDL smaller than 0.25

dB across the entire attenuation range, a value that is lower than that achieved in any

other material system [6].
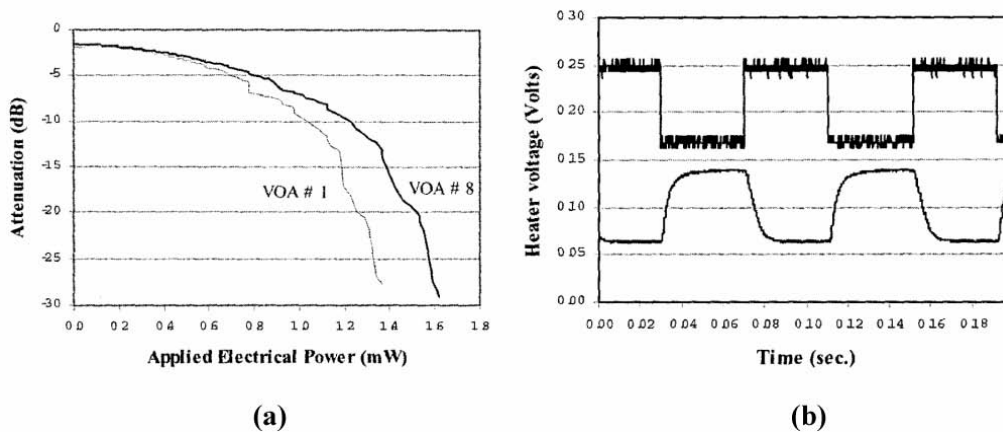
Fig. 2.1   (a) VOA attenuation characteristics of two VOAs in an 8-channel array.
(b) Time-dependent switching characteristic of the VOA array. [4]

2.2.2   Y-branch VOA

For more compact functional VOA, S. S. Lee, et al [7] proposed and fabricated an asymmetric linear Y-branch waveguide VOA and an optical power tap, using perfluorocyclobutane (PFCB) as cladding material and Benzocylclobutane (BCB) as core material, as shown in Figure 2.2 (a) and (b). The branching angle of the asymmetric Y-branch is 0.16^o, and the stripe widths of the wide and narrow waveguides are 6 and 5 μm, respectively. The core layer thickness and rib height of the channel waveguides are 5.5 and 1.5 μm, respectively, ensuring single mode operation. The wide arm waveguide is used for the main output port. The optical power tap, which is formed by attaching a curved waveguide to the main port to tap a fraction of its power, serves as an output monitoring port. The tapped power is fed back to an electrical driving source to maintain a constant optical output [8]. The narrow arm is connected to a tapered S-bend waveguide to enlarge the distance between the two waveguides of the branch. With no electrical power, the optical power launched from the input waveguide is predominantly coupled to the wide arm of the branch. When electrical power is supplied to the electrode to induce the thermo-optic effect, the effective refractive index of the wide arm is decreased, and so the input optical power is transferred gradually to the narrow arm. As a result, the optical output decreases with applied electrical power enabling an efficient attenuation of the input optical power.
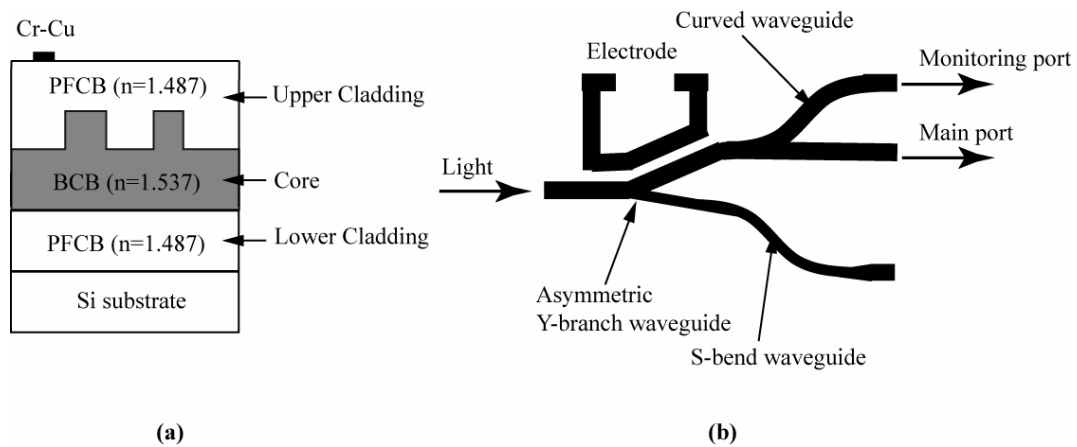
Fig. 2.2   (a) Cross-section of the Y-branch VOA.   (b) Structure of the Y-branch VOA. [7].

By utilizing the modal evolution effect in asymmetric branches, the attenuator has enhanced fabrication tolerance and reduced wavelength sensitivity.   As shown in Figure 2.3 (a), the attenuator exhibited a dynamic range of more than 20 dB at 1550 nm with an electrical power of 200 mW.   By etching away the silicon substrate under the asymmetric Y-branch waveguide, which increases the temperature gradient in waveguide, the electrical power consumption can reduce to 25 mW [9].   The polarization dependent loss (PDL) was negligibly small when no electrical power was applied and increased up to 2 dB for the attenuation of 10 dB.   However, by using an electronic feedback control, the slowly changing input polarization on attenuation setting can be reduced from 2 dB to 0.9 dB.   Figure 2.3 (b) shows that rise time of about 1 ms can be achieved and the wavelength uniformity was less than 1.2 dB over the range of 1530–1560 nm.

(a)   **(b)**
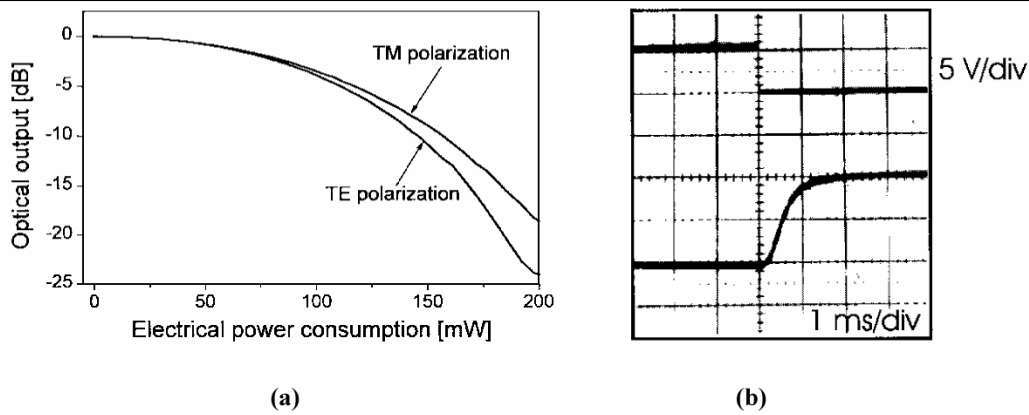
Fig 2.3   (a) Attenuation vs. electrical power consumption for TE and TM polarizations.
(b) Optical response of the attenuator to an electrical square wave. [7]

2.2.3   Bending Structure VOA

S. M. Garner and S. Caracci reported a compact VOA [10], which is based on modified waveguide bends as shown in Figure 2.4 (a).   It consists of a curved waveguide with an electrode heater deposited above it.   Light propagates through the bend with low loss when no electrical power is applied to the heater.   When electrical power is applied, due to the negative thermo-optic coefficient of polymer, the refractive index of the cladding nearer the heater is reduced more than that close to the substrate, resulting in a vertical index gradient.   This vertical index gradient pushes the optical mode away from the upper cladding to the lower cladding.   The waveguide bend itself distorts the mode horizontally.   The overall effect reduces the optical mode confinement within the core and results in radiation loss.   In effect, the controllable thermal gradient produces a variable loss coefficient throughout the bend length.   Further enhancement of the attenuation response can be achieved by reducing the waveguide width in the curved region (bend width).   Figure 2.4 (b)

shows the experimental attenuation results of 5 mm bend length waveguides for different bend widths. When an electrical power of 250 mW is applied, the attenuation of the 3 μm bend width device is more than 40 dB, which is greater than the attenuation of 5 μm and 7 μm bend width devices by about 20 dB. When no electrical power is applied, the fibre-to-fibre insertion loss and PDL are 1.57 dB and 0.12 dB, respectively. No PDL change was observed when electrical power was applied. However, the wavelength dependence of the mode confinement causes wavelength dependence in attenuation. At an average attenuation level of 15 dB, there is a 4-dB response difference between wavelengths of 1530 nm and 1570 nm, which restrict the device to operate in single wavelength channel.

(a) **(b)**
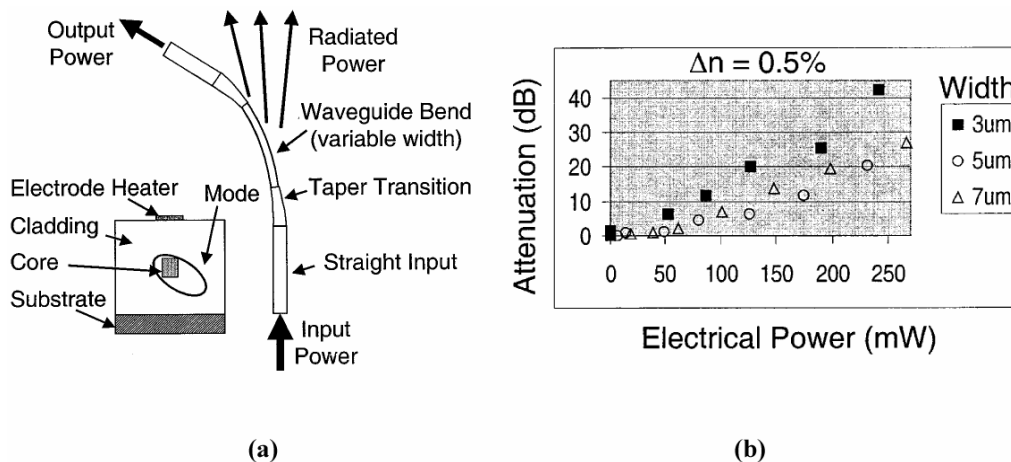
Fig. 2.4   (a) Top view and cross section of a VOA design reported in [10].   (b) Attenuation response for varying bending widths [10]

Y. T. Lu, et al [11] proposed a bending polymer waveguide VOA with an S-shaped structure. Its double bending design, incorporated with the thermal-optical property of polymer, provides optimal optical attenuation within a small waveguide length.

Figure 2.5 (a) shows the cross section of the S-shaped waveguide VOA. The operating principle of the optical loss mechanism in such a buried-type S-shaped waveguide VOA is based on the index variation of the core under a change in temperature, which is different with the vertical index gradient principle bending VOA reported by Garner and Caracci [10]. The effective index of the fundamental mode will be changed when the refractive index of the core is varied. Consequently, the field distribution of the mode inside the core is changed. The tuning range of the thermal-dependent index of the polymer determines the variation of the mode field. The bending design of the waveguide provides sufficient attenuation to meet the requirements of WDM networks. The design of the S-shaped structure is shown in Figure 2.5 (b). Its attenuation range in the optical communication windows of 1.31 and 1.55 μm are 20 and 30 dB, respectively and the PDL was very small.
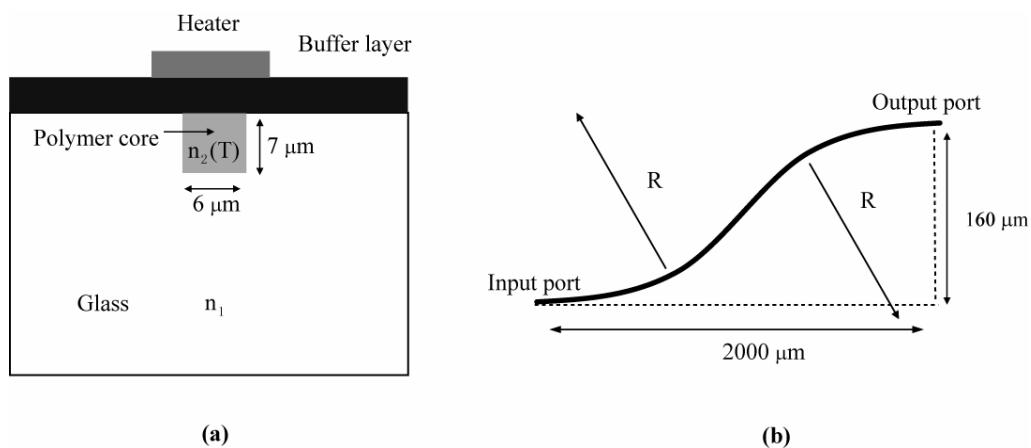
Fig. 2.5   (a) Cross section of the waveguide VOA reported in [11].   (b) S-shaped waveguide structure, where R is the radius of the bending curvature [11]

2.2.4   Higher Order Mode Excitation and Filter VOA

Y. O. Noh, et al [12] fabricated a novel VOA based on higher order mode excitation and single mode filtering mechanisms. It consists of input and output single mode waveguides, two tapering regions, a multimode waveguide region, and an electrode deposited on the multimode waveguide with an angle α as shown in Figure 2.6. The core and cladding are made of polymeric materials and are sold by ZenPhotonics Co. under the trade name of ZP1010[TM] and ZP2145[TM], respectively. The refractive index difference between the core and the cladding is 0.7%. The cross-section of the waveguide is 7×7 μm^2, which supports single mode operation. The multimode waveguide width is 40 μm, which supports at least six waveguide modes. At first the light is expanded adiabatically from the single mode waveguide into the multimode waveguide. Due to the negative thermo-optic effect of the polymer, the refractive index under the heater becomes lower and reflects some of the propagating light at an angle of 2α with respect to the horizontal axis. The reflected light is coupled to the higher-order guiding modes. These higher order modes are successively filtered out by the output tapering region and single mode waveguide, which induce the attenuation. As the applied voltage increases, the amount of reflected light increases, leading to larger attenuation.
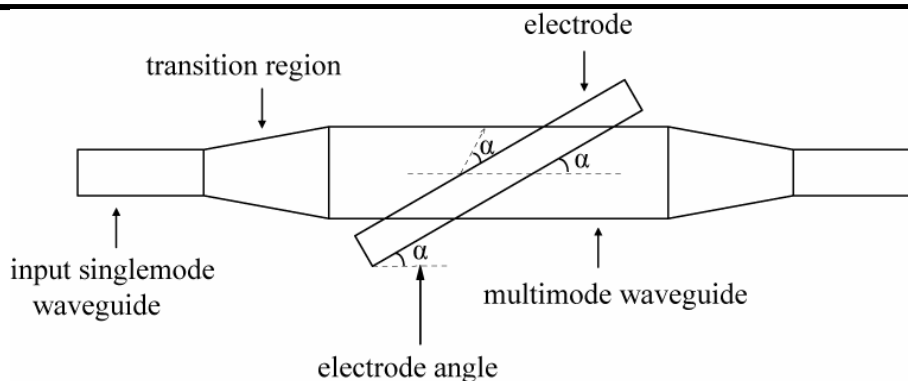
Fig. 2.6   Schematic diagram of higher mode excitation VOA [12]

The length, the width and the angle of the heater are optimized to give a maximum

attenuation for a given temperature change and are selected as 3,800 μm, 7.2 μm, and

1.6^{o}, respectively.   Using the beam propagation method (BPM), the attenuation

characteristics of the VOA was calculated and is shown in Figure 2.7 (a), at the

operating wavelength of 1550nm.   The solid line is the attenuation characteristic of

the TE mode and the dotted line is that of the TM mode.   The attenuation curves for

both modes are almost the same, with a difference of less than 1 dB even at 30 dB

attenuation.   The measured attenuation characteristics of the fabricated devices are

shown in Figure 2.7 (b).   When an electrical power of 80 mW was applied, the

attenuation of the device was about 30 dB.   The measured characteristics were in

good agreement with the simulation results.   However, the polarization dependence

is less than 0.2 dB at 0-dB attenuation and 1 dB at 10-dB attenuation, which is higher

than the simulated results.   Such discrepancy may arise from a slight difference in

the confinement factors of the TE and TM modes in the fabricated devices.   The rise

and fall times were measured to be about 5 ms and the insertion loss of the device was

less than 2 dB.

<center>(a)   (b)</center>
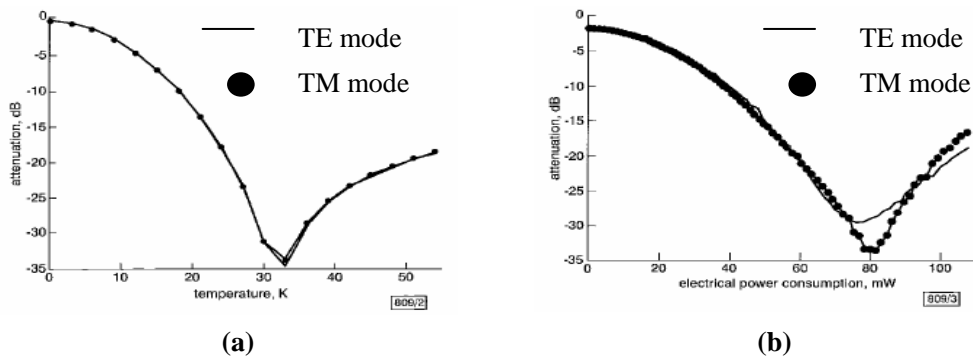
Fig. 2.7   (a) Calculated result of attenuation characteristics against temperature.   (b) Measured
attenuation characteristics against applied electrical power. [12]

2.3   Novel Reflective Variable Optical Attenuator

We proposed a novel reflective variable optical attenuator, which works in reflection

mode and therefore has only one port that serves as the input as well as the output.

RVOA can be used in some special devices to simplify their design and to reduce their

cost.   A dynamic gain equalizer used to equalize non-uniform channel power levels

of ultra or extreme long haul WDM systems could benefit by using RVOA.   Figure

2.8 (a) shows a conventional DGE that employed two AWG modules and a VOA array.

One AWG module is used to demultiplex the WDM signal and then each signal

passing through the VOA array is independently attenuated to attain the same output

power and the second AWG module is used to multiplex all wavelength channels into

a single output.   Figure 2.8 (b) shows a proposed DGE design using RVOA, one AWG and a circulator.   In this approach, the demultiplexed WDM optical signals are attenuated independently and then reflected back to the same AWG module, where they are multiplexed and then routed to the output via the circulator.   This approach eliminates the need for two matching AWGs and reduces the number of VOA-to-AWG couplings by half, leading to a simpler DGE module design which is potentially low cost.   Furthermore, if the RVOA is implemented using waveguide technology, it opens the possibility of integrating RVOA and AWG on a single wafer. This would eliminate the costly VOA-to-AWG couplings, leaving only one optical coupling between the circulator and the DGE module.   The cost reduction of DGEs that adopt this approach should be quite substantial, particularly for large channel count.

In this work, we investigated two types of RVOA.   One is based on fibre coupler and the other is based on polymer waveguide.   The polymer waveguide RVOA offers many advantages over the fibre coupler RVOA.   Polymeric waveguide-based RVOA also requires lower electrical power consumption and potential of mass production.

(a)

(b)
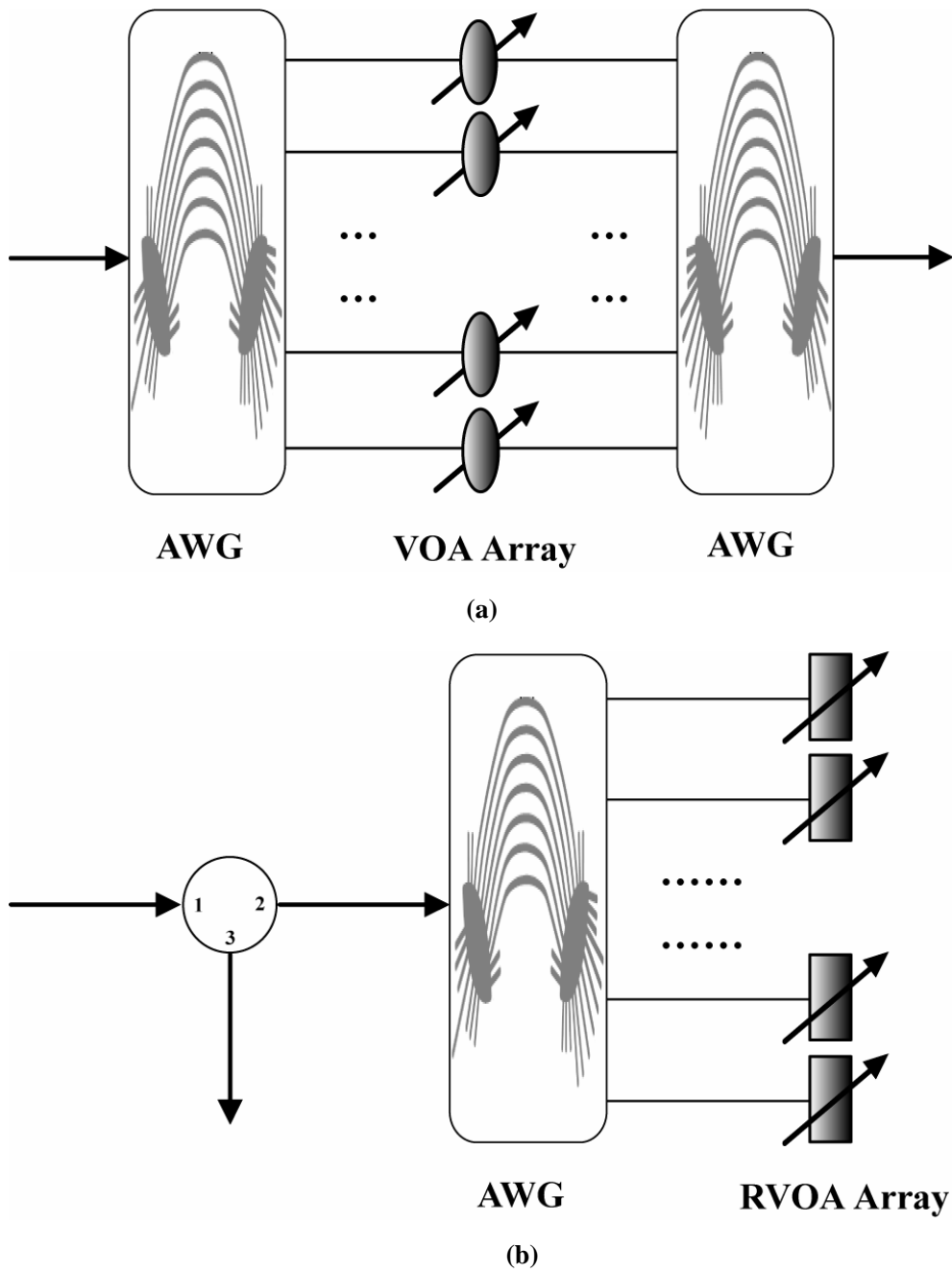
Fig. 2.8 Dynamic gain equalizers for WDM systems: (a) Conventional design using two AWGs and a VOA array. (b) A proposed design using a novel RVOA array, one AWG and a circulator.

2.3.1   Fibre Coupler-based RVOA
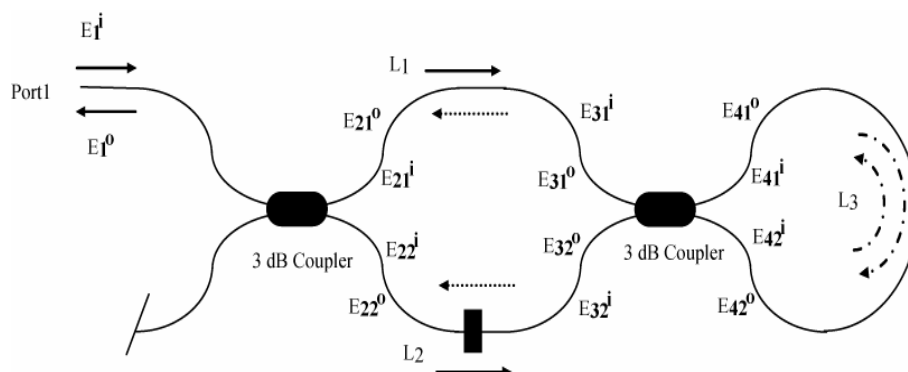
Fig. 2.9   Structure of the proposed fibre coupler-based RVOA

Figure 2.9 shows the fibre coupler-based RVOA, which consists of two 3-dB couplers and one piezoelectric transducer (PZT) for stretching one arm of the 3-dB coupler to alter the optical path length.   The device behaves as a Mach-Zehnder interferometer as well as a reflector.   When signal is launched to the input of the RVOA, the optical power is divided into two beams of equal intensity by the first 3-dB coupler.   Both beams are then reflected back by the second 3-dB coupler, which functions as a fibre loop reflector [21].   The two reflected beams interfere in the first 3-dB coupler and the output is taken from the same input port.   The optical attenuation is varied by altering the arm length with different voltages applied to the PZT.

We also proposed another configuration of RVOA as shown in Figure 2.10 (a) to achieve large adjustable attenuation range.   This is because the beams interference twice, the dynamic attenuation range of the RVOA is doubled.   The PDL of fibre

coupler-based RVOA is expected to be large, because normal fibre coupler has birefringence as a result of fibre twisting and tapering during the fabrication of fused fibre couplers. The PDL, however, could be reduced if a Faraday rotator mirror was employed, as shown in Figure 2.10 (b).

(a)

(b)
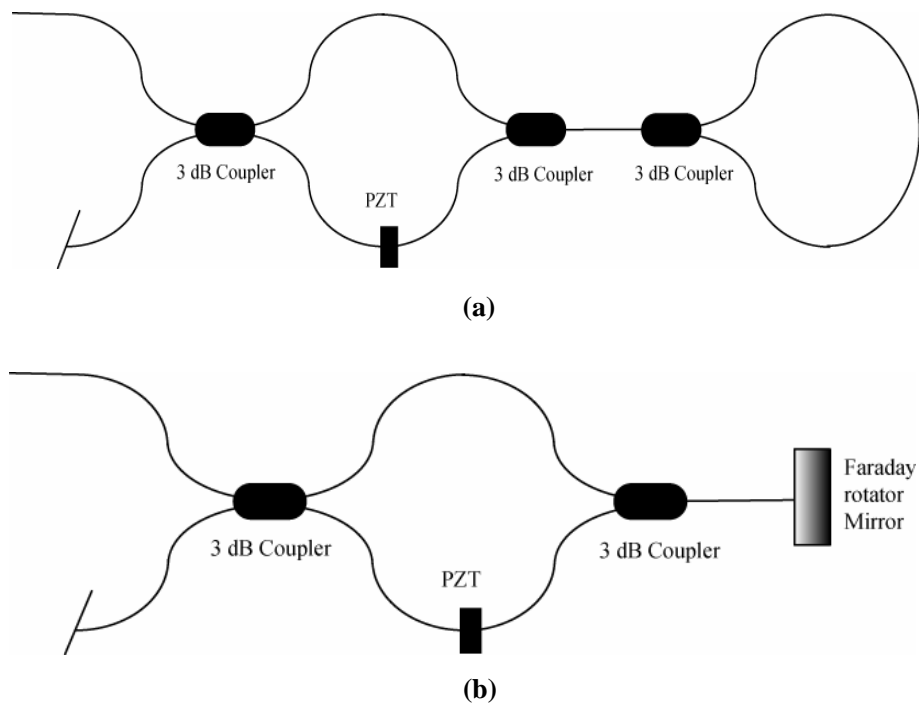
Fig. 2.10   (a) Large attenuation range fibre coupler-based RVOA.   (b) Low PDL fibre
             coupler-based RVOA by using a Faraday rotator mirror.

2.3.1.1   Theoretical Modeling of the Fibre Coupler-based RVOA

In analyzing the fibre coupler-based RVOA, it is assumed that the state of polarization remains constant throughout the device and that the loss through the fibre is so small that it can be neglected. The transfer matrix method described in Ref. [22] was used to analyze the optical fibre coupler. Using this approach, seven linear matrix

equations can be set up to establish the relationships between the sixteen complex

electric fields propagating in both sides of the couplers, which are described by

Equation 2.1. The coupling ratio and excess coupling loss of the couplers are

denoted by K_i and γ_i, where i=1, 2.

Using the nomenclature shown in Figure 2.9 and the transfer matrix formulation, the

relationships between the sixteen complex electric fields are given by: [22]

$$\begin{pmatrix} E_{21}^{o} \\ E_{22}^{o} \end{pmatrix} = (1-\gamma_1)^{1/2} \begin{pmatrix} \sqrt{K_1} & -j\sqrt{1-K_1} \\ -j\sqrt{1-K_1} & \sqrt{K_1} \end{pmatrix} \begin{pmatrix} E_{1}^{i} \\ 0 \end{pmatrix}, \qquad (2.1a)$$

$$\begin{pmatrix} E_{31}^{i} \\ E_{32}^{i} \end{pmatrix} = \begin{pmatrix} \exp(-\dfrac{j2\pi n L_1}{\lambda_0}) & 0 \\ 0 & \exp(-\dfrac{j2\pi n L_2}{\lambda_0}) \end{pmatrix} \begin{pmatrix} E_{21}^{o} \\ E_{22}^{o} \end{pmatrix}, \qquad (2.1b)$$

$$\begin{pmatrix} E_{41}^{o} \\ E_{42}^{o} \end{pmatrix} = (1-\gamma_2)^{1/2} \begin{pmatrix} \sqrt{K_2} & -j\sqrt{1-K_2} \\ -j\sqrt{1-K_2} & \sqrt{K_2} \end{pmatrix} \begin{pmatrix} E_{31}^{i} \\ E_{32}^{i} \end{pmatrix}, \qquad (2.1c)$$

$$\begin{pmatrix} E_{41}^{i} \\ E_{42}^{i} \end{pmatrix} = \begin{pmatrix} 0 & 1 \\ 1 & 0 \end{pmatrix} \begin{pmatrix} \exp(-\dfrac{j2\pi n L_3}{\lambda_0}) & 0 \\ 0 & \exp(-\dfrac{j2\pi n L_3}{\lambda_0}) \end{pmatrix} \begin{pmatrix} E_{41}^{o} \\ E_{42}^{o} \end{pmatrix}, \qquad (2.1d)$$

$$\begin{pmatrix} E_{31}^{o} \\ E_{32}^{o} \end{pmatrix} = (1-\gamma_2)^{1/2} \begin{pmatrix} \sqrt{K_2} & -j\sqrt{1-K_2} \\ -j\sqrt{1-K_2} & \sqrt{K_2} \end{pmatrix} \begin{pmatrix} E_{41}^{i} \\ E_{42}^{i} \end{pmatrix}, \qquad (2.1e)$$

$$\begin{pmatrix} E_{21}^{i} \\ E_{22}^{i} \end{pmatrix} = \begin{pmatrix} \exp(-\dfrac{j2\pi n L_1}{\lambda_0}) & 0 \\ 0 & \exp(-\dfrac{j2\pi n L_2}{\lambda_0}) \end{pmatrix} \begin{pmatrix} E_{31}^{o} \\ E_{32}^{o} \end{pmatrix}, \qquad (2.1f)$$

$$\begin{pmatrix} E_{1}^{o} \\ E_{12}^{o} \end{pmatrix} = (1-\gamma_1)^{1/2} \begin{pmatrix} \sqrt{K_1} & -j\sqrt{1-K_1} \\ -j\sqrt{1-K_1} & \sqrt{K_1} \end{pmatrix} \begin{pmatrix} E_{21}^{i} \\ E_{22}^{i} \end{pmatrix}. \qquad (2.1g)$$

And

$$I = (E)(E^*)$$ (2.2)

From (2.1) and (2.2), we obtain

$$\frac{I_1^o}{I_1^i} = (A + B - C)^2 - 4A(B - C)\sin^2(\frac{\delta}{2}) + 4B * C\sin^2(\delta),$$ (2.3)

where δ is the phase difference between the two arms of lengths L_1 and L_2 and is given by:

$$\delta = \frac{2n\pi(L_2 - L_1)}{\lambda_0}.$$ (2.4)

The constants A, B and C are given by:

$$A = 2(1 - 2K_1)K_1^{1/2}(1 - K_1)^{1/2}(1 - \gamma_1)^2,$$ (2.5a)

$$B = 2K_2^{1/2}(1 - K_2)^{1/2}(1 - K_1)(1 - \gamma_1)(1 - \gamma_2), \text{ and}$$ (2.5b)

$$C = 2K_2^{1/2}K_1(1 - K_2)^{1/2}(1 - \gamma_1)(1 - \gamma_2).$$ (2.5c)

Since both K_1 and K_2 are equal to 1/2.   So the RVOA equation is given by:

$$\frac{I_1^o}{I_1^i} = (1-\gamma_1)^2 (1-\gamma_2)^2 \sin^2(\delta) . \tag{2.6}$$

It can be seen from Equation 2.3 and Equation 2.5 that coupler with unequal splitting ratio will introduce excess coupler loss in the RVOA. However, nowadays the splitting ratio error of fused fibre couplers can be made very small, resulting to a small reduction in both the insertion loss and the adjustable attenuation range.

Equation 2.6 is obtained under the assumption that the state of polarization of two split beam is equal and remains constant throughout the device, and complete interference occurs. This assumption can not be realized in reality for fused fibre couplers. Complete interference of the two split beams does not occur and therefore the RVOA equation can be rewritten as:

$$\frac{I_1^o}{I_1^i} = (1-\gamma_1)^2 (1-\gamma_2)^2 \left[(1-\eta) \sin^2(\delta) + \eta \right], \tag{2.7}$$

where η is the non-interference part of the input light and attributes to the reduction in the adjustable attenuation range of the RVOA.

In the case of the RVOA shown in Figure 2.10, the signal passes through the Mach-Zehnder interferometer twice and the equation can be written as:

$$\frac{I_1^o}{I_1^i} = (1-\gamma_3)(1-\gamma_1)^4(1-\gamma_2)^4 \left[(1-\eta)\sin^2(\delta/2) + \eta\right]^2$$

$$\approx (1-\gamma_3)(1-\gamma_1)^4(1-\gamma_2)^4 \left[(1-\eta)^2\sin^4(\delta/2) + \eta^2\right]$$

(2.8)

where γ_3 is the reflection loss of the mirror shown in Figure 2.10 (b). The main difference of the RVOAs in Figure 2.9 and Figure 2.10 (a) and (b) is that the light passes through the unbalanced arms twice but the beams interfere only once for the RVOA shown in Figure 2.9. However, for the two RVOAs shown in Figure 2.10 (a) and (b), the beams interfere twice. Consequently, the RVOAs in Figure 2.10 (a) and (b) exhibit larger attenuation range than the RVOA in Figure 2.9.

2.3.1.2 Measurement Setup of the Fibre Coupler-based RVOA
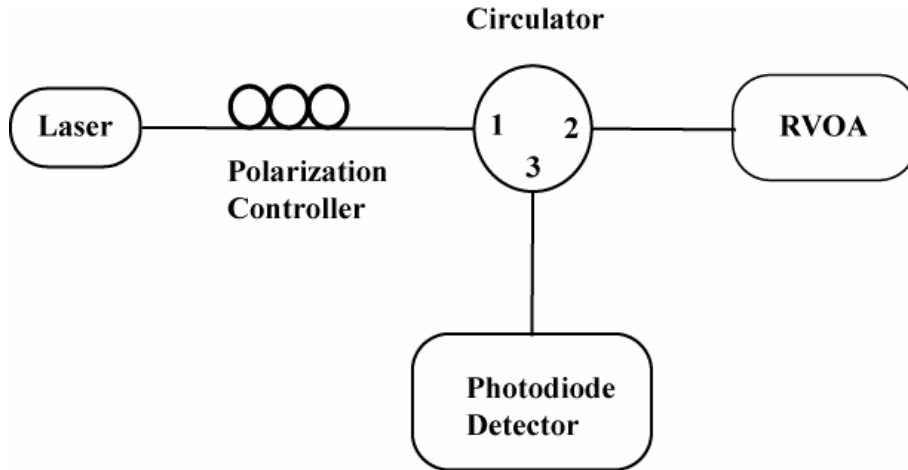
Fig. 11   Measurement setup of the RVOA.

The experimental setup used to measure the performance of the fibre coupler-based RVOA is shown in Figure 2.11. The polarization controller (PC) is used to vary the

polarization of the input light to evaluate the PDL of the RVOA. Light from the

laser diode with wavelength of 1550.64 nm and output power of 0 dBm is launched

into the RVOA via port 1 and port 2. The light propagated in the RVOA and then

reflected back to the port 2 of the circulator and output from port 3. The power of

the light reflected from the RVOA is measured with an optical power meter to

determine the adjustable attenuation of the RVOA. The optical bandwidth of the

RVOA can be measured with a LED or tunable laser.

2.3.1.3 Results and Discussions

The measured relationship of the attenuation loss and the voltage of Faraday rotator

mirror RVOA, 3-coupler RVOA and 2-coupler RVOA is shown in Figure 2.12 by the

diamond dots, the triangle dots and the circle dots, respectively. It is clearly shown

in Figure 2.12 that the RVOA with Faraday rotator mirror and the 3-coupler RVOA

have almost double the attenuation range than the 2-coupler RVOA. The simulation

results of those RVOAs are also shown in Figure 2.12 by solid lines under the

assumption that 10% of the input light energy did not interference due to

non-polarization-maintained coupler and fibre. The 2-coupler RVOA resembles the

$\log(\sin^2)$ function and the Faraday rotator mirror RVOA and 3-coupler RVOA

resemble the $\log(\sin^4)$ function according the Equation 2.7 and 2.8. An exact

$\log(\sin^2)$ and $\log(\sin^4)$ function cannot be produced because the linear expansion of

the PZT is not linearly proportional to the applied voltage. The peaks of the Faraday

rotator mirror RVOA and 3-coupler RVOA occurring at different voltages are due to the different initial phase differences of the input test signal, which is induced from the different polarizations of the test input signal. The insertion loss of 2-coupler RVOA, 3-coupler RVOA and Faraday rotator mirror RVOA is about 0.7 dB, 2.2 dB and 2.5 dB, respectively, which is due to the unequal splitting ratio and excess loss of couplers and Faraday rotator mirror. The attenuation range is about 9 dB for the 2-coupler RVOA, which is adequate for use in dynamic gain equalizer for WDM systems, and is about 22 dB for the 3-coupler RVOA and Faraday rotator mirror RVOA.
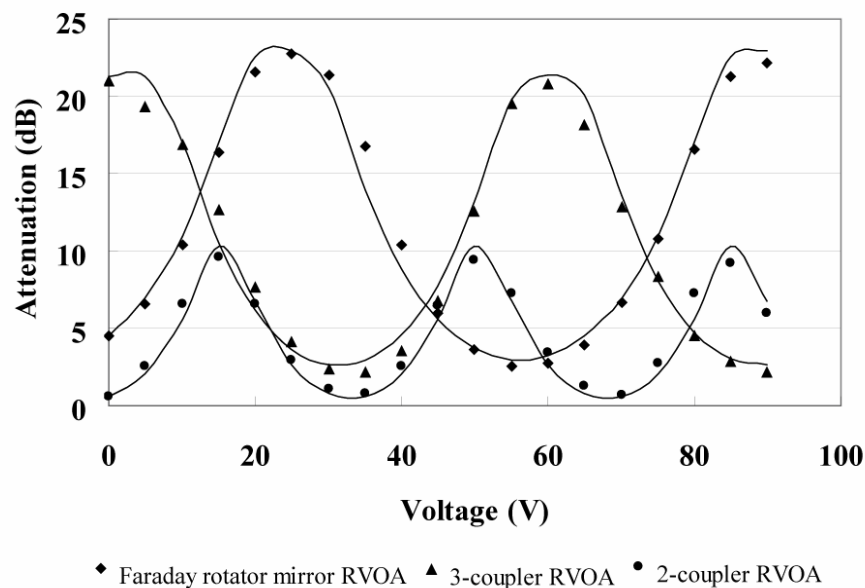
Fig. 2.12   Measured results of the three designs of fibre coupler-based RVOAs.   Solid lines are calculated results.

Using the tunable laser to replace the LD in Figure 2.11, we can measure the operation bandwidth of the RVOA, which is inversely proportional to the optical path

difference of the Mach-Zehnder interferometer and can be deduced from Equation 2.7.

For example, when the optical path difference is 1 mm, the RVOA bandwidth is about

0.2 nm and when the optical path difference changes to 0.1 mm, the bandwidth is

about 2 nm.   By accurately controlled the optical path difference, the bandwidth of

this kind of RVOA can be made large enough to be used for single optical wavelength

attenuation.   But it cannot be used to attenuate many WDM wavelengths

simultaneously.

The polarization dependent loss (PDL) of the RVOA is also measured by varying the

polarization of the input light.   The PDL of the 2-coupler RVOA and 3-coupler

RVOA is about 5 dB.   This is because normal fibre coupler has birefringence

because of twisting of the fibre when tapering the fibre coupling.   Using a Faraday

rotator mirror to rotate the polarization of the reflected optical signal by 90-degree to

compensate the birefringence of the 3-dB coupler and fibre, the PDL decreased to

about 0.5 dB.

2.3.2   Polymeric Waveguide-based RVOA

Polymeric waveguide-based RVOA offers the advantages of small size and

compatibility to AWGs.   We proposed and designed a novel waveguide RVOA based

on polymeric waveguide.   The tunable coupler structure instead of the non-balanced

MZ structure was used to realize the RVOA function due to its short length feature.

2.3.2.1 Waveguide Design

The material employed for the core of the waveguide is a negative tone epoxy Novolak resin (ENR) polymer from MicroChem Corp. ENR is more than a hundred times more sensitive to electron-beam exposure than poly(methylmethacrylate) (PMMA) and the polymeric material used for the cladding layer is the UV-cured resin Norland Optical Adhesive 61 (NOA61). In this work, the ENR strip waveguides were fabricated by e-beam exposure. Figure 2.13 shows the cross-section of a waveguide in the ROVA device structure. A silicon wafer was used as the substrate to provide mechanical support. To fabricate the waveguide, a 2.5-µm-thick SiO_2 was grown on the substrate to form a spacer between the substrate and waveguide core. A layer of 6-µm-thick NOA61 was first spin-coated on the substrate to form a cladding layer. The thickness of the layer is determined by the speed of the spinner. The lower cladding layer was made thick enough to prevent light in the core layer from coupling into the silicon substrate. It was then cured for 10 min using UV light at 365 nm wavelength. To improve the adhesion, the sample was baked at 50 °C for 12 h in an oven. Then a 2.7-um thick core ENR polymer was spin-coated on top of the lower cladding layer. A pre-bake time of 5 min at 90 °C was applied to all samples before exposure to electron-beam to write the waveguide. All the pattern exposures were performed using a Leica EBL-100L nanowriter system at 50 KeV. The beam current was measured by a Faraday cup and kept at 40 pA and the electron-beam spot diameter was 70 nm. The post-exposure bake time was fixed at 3

min.   After exposure and post-exposure baking, the ENR was developed for 20 s in

propylenglygol–monomethylether–acetate (PGMEA) and then rinsed in fresh

PGMEA again to form the stripe channel waveguides.   The width of the waveguide

is 2.7 µm.   Finally, a 4-µm thick UV-cured NOA61 layer was spin-coated on top of

the core layer to form the upper cladding.   The refractive indexes of ENR and

NOA61 at the 1550 nm wavelength are 1.575 and 1.54, respectively.   Under these

conditions, the waveguide supports single mode operation.
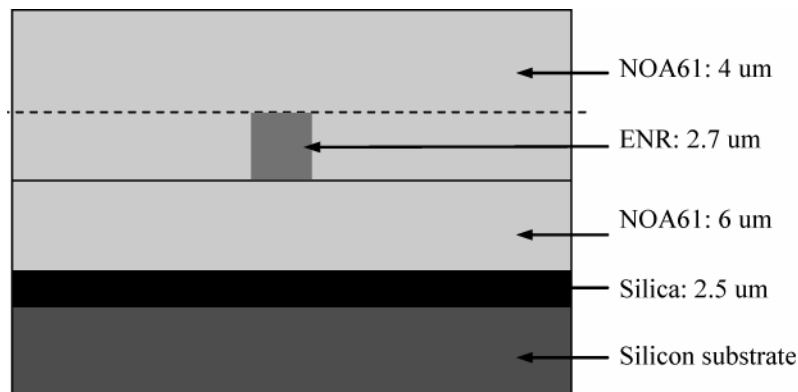
Fig. 2.13   Cross-section of the polymeric waveguide-based RVOA

The directional coupler can be made in different kinds of design, such as close

position coupling [23], Y-branch power splitter [24] and multimode interference

structures [25].   For simplicity, we choose the close position coupling method to

make the 3-dB coupler.   The waveguide separation distance is 5 µm.   Using BPM

simulation, the coupling waveguide region length was calculated to be 1.694 mm for 3

dB coupling at 1550 nm wavelength.   Because of the large refractive index contrasts

of 2.2% between the core and cladding materials, the radius of the curve waveguides

can be as small as 2 mm, yet introduce insignificant micro-bending loss. The total

effective area occupied by the RVOA is about 4x7 mm^2. The detail pattern is

illustrated in Figure 2.14 (a) and a photograph of the RVOA is shown in Figure 2.14

(b).
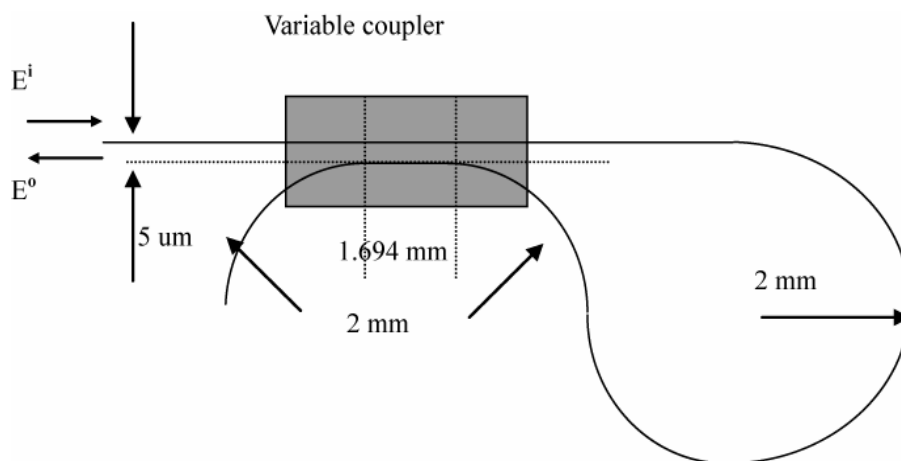
(a)
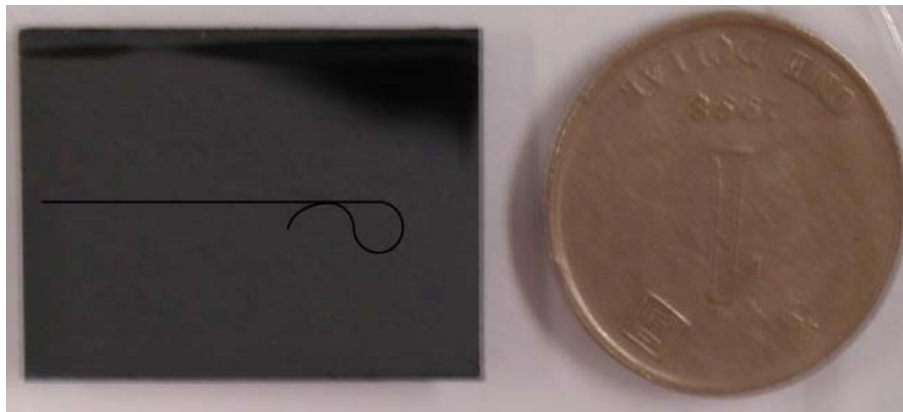
(b)

Fig. 2.14   The pattern structure of the polymer waveguide-based RVOA: (a) The designed
pattern of the RVOA.   (b) Photograph of the RVOA.

2.3.2.2   Theoretical Analysis

The proposed polymeric waveguide-based RVOA can be considered as a tunable coupler with its two output ports connected.   Ignoring the coupling loss of the fibre and waveguide and applying the same principle as the fibre coupler-based RVOA, we can obtain the relationship of the output, I^o, vs. input, I^i, for the waveguide-based RVOA as follows [22]

$$\frac{I^o}{I^i} = 4K(1-K)(1-\gamma)^2,$$ (2.9)

where $K = \cos^2(\kappa L)$ and γ are the coupling ratio and excess coupling loss of the waveguide coupler, respectively. L is the length of coupling waveguide and κ is the mode-coupling coefficient, which is determined by the core and cladding refractive index, waveguide width and separation distance.   The refractive index of the polymer material is sensitive to temperature (typical value of ENR is $-1.6*10^{-4}/^oC$) and the mode-coupling coefficient κ also varies with temperature, which subsequently induces change in the output power.   Using the BPM simulation, we can obtain the κ value for different temperatures, therefore the output loss versus temperature of the waveguide-based RVOA can be obtained by using Equation 2.9.

2.3.2.3 Preliminary Measurement Results

Figure 2.15 shows the power distribution of light in the RVOA waveguide. Figure 2.15 (a) is image of the output signal from the same cross section line waveguide taken with an IR camera and Figure 2.15 (b) is the simulation result using BPM technique. The power distribution of light in the waveguide confirms single mode operation.

(a)   **(b)**
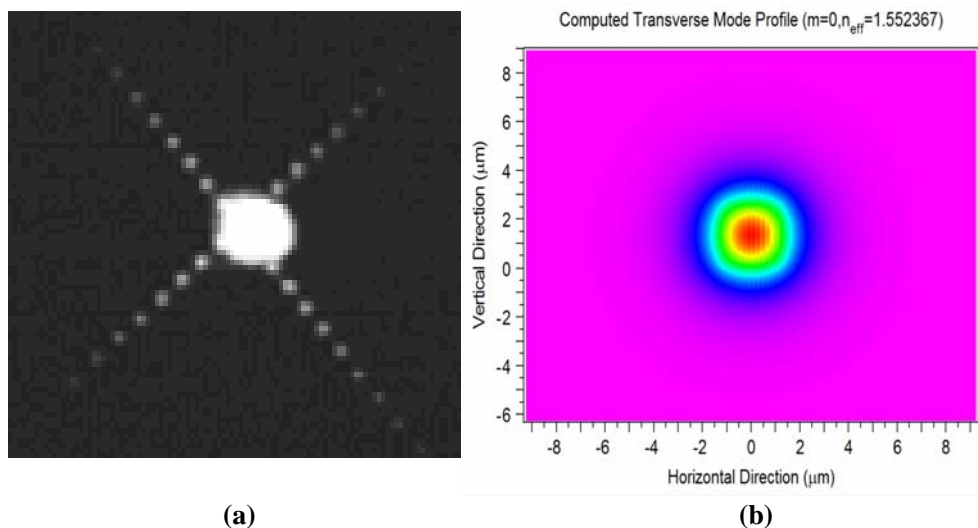
Fig. 2.15   The (a) measured and (b) simulated power distribution of the waveguide

The measured relationship of the RVOA attenuation versus temperature is shown in Figure 2.16. The calculated insertion loss of the RVOA under the different temperatures is also shown in Figure 2.16 by solid lines using the BPM simulation without including the coupling loss and material loss. Index-matching liquid with refractive index between the refractive index of the SMF and waveguide is needed when measuring the insertion loss to reduce the facet reflection. We select the 1.512

refractive index matching liquid. The minimum insertion loss of the waveguide

RVOA is about 18 dB, which is quite large and is attributed to many factors. One is

the coupling loss between the waveguide and single mode fibre due to the mode

mismatching and in our case, the coupling loss is about 3.5 dB, which can be reduced

greatly by using a tapered waveguide. The other is the propagation loss due to the

ENR material (about 0.5 dB/cm) and in our case the propagation loss is about 2 dB.

Misalignment between the SMF and the core waveguide can also induce additional

coupling loss. The dynamic range of waveguide RVOA is about 15 dB, which is

adequate for DGE module. When changing the polarization condition with a PC, we

measured the PDL which is less than 0.2 dB.
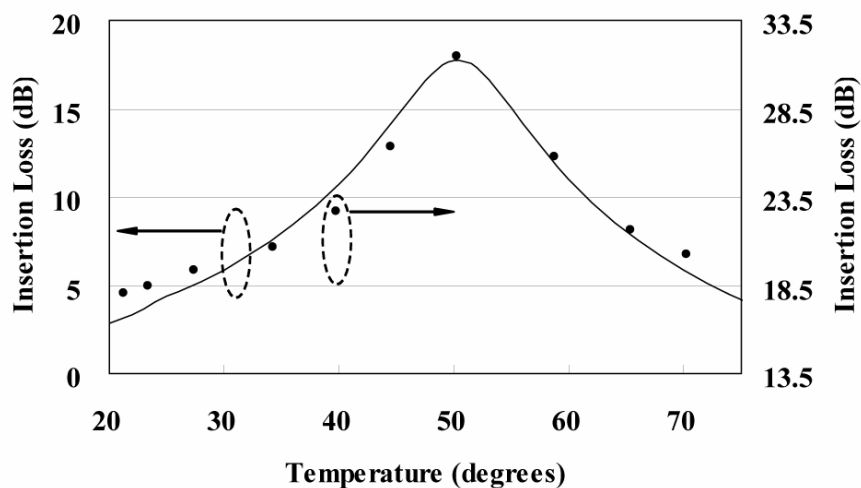
Fig. 2.16   Measured insertion loss of the RVOA at different temperatures.   Solid line is the calculted results.

2.4   Chapter Summary

In this chapter, the background of different types of VOA designs, especially one with a planar light-wave circuit, which appears to be a more promising technology in VOA design were reviewed.   Our proposed reflective variable optical attenuator (RVOA) and its application in DGE are described.

The theoretical analysis of the fibre coupler-based RVOA was given and the experiment results of three different fibre coupler-based RVOAs were presented. The attenuation range is about 9 dB for 2-coupler RVOA and is more than 22 dB for 3-coupler RVOA and Faraday rotator mirror RVOA.   Fibre couplers exhibit birefringence due to the twisting and tapering of the fibre during fabrication, leading to large PDL of up to 5 dB.   However, this can be reduced to about 0.5 dB by using the Faraday rotator mirror in the configuration.

Another proposed RVOA based on polymeric waveguides was also investigated in this work.   A polymeric waveguide-based RVOA was fabricated with negative tone ENR polymer as the core material and UV-cured resin NOA61 polymer as the cladding layer material.   The cross section of the RVOA was $2.7\text{x}2.7$ μm^2 and support single mode operation.   The total effective area occupied by the RVOA is about $4\text{x}7$ mm^2.   A dynamic range of 15 dB attenuation was achieved and the PDL was measured to be less than 0.2 dB.   The insertion loss of waveguide is about 18 dB,

which is too large and is mainly due to coupling loss, rough edges of waveguide and

misalignment between the waveguide and fibre pigtail.

Reference

1. S. Masuda, "Variable attenuator for use in single-mode fiber transmission systems," *Appl. Opt.*, vol. 19, no. 14, pp. 2435–2438, Jul. 1980.

2. K. Oh, W. Shin, Y. S. Jeong, and J. W. Lee, "Development of microoptical waveguide on microactuating platform technologies for reconfigurable optical networking", *J. Lightwave Technol.*, vol. 23, no. 2, pp. 533-542, Feb. 2005.

3. M. Li and S. Peng, "Dynamic gain equalization in fiber-optic communication systems" *LEOS 2002, 15th Annual Meeting of the IEEE Lasers and Electro-Optics Society*, vol. 2, pp. 879-880, 10-14 Nov. 2002.

4. N.S. Lagali, J.F.P. van Nunen, D. pant, and L. Eldada, "Ultra-low power and high Dynamic Range Variable Optical Attenuator Array," *ECOC 2001, 27th European Conference on Optical Communication*, vol. 3, pp. 430-431, 30 Sept. -- 4 Oct. 2001.

5. Kawai, T., Koga M., Okuno M., Kitoh T., "PLC type compact variable optical attenuator for photonic transport network," *Electron. Lett.*, vol. 34, pp. 264-265, 1998.

6. Louay Eldada, "Polymer Integrated Optics: Promise vs. Practicality," *Photonics West 2002, Proc SPIE (Organic Materials and Devices IV)*, vol. 4642, pp. 11–22, 19-25 Jan. 2002.

7. Sang-Shin Lee, Yong-Sung Jin, Yung-Sung Son, and Tae-Kyung Yoo, "Polymeric Tunable Optical Attenuator with an Optical Monitoring Tap for

WDM Transmission Network," *IEEE Photon. Technol. Lett.*, vol. 11, pp.590-592, 1999

8. Yong-Sung Jin, Sang-Shin Lee, Yung-Sung Son, "Feedback controlled variable optical attenuator for channel power regulation in WDM systems," *Electron. Lett.*, vol. 35, pp.916-917, 1999.

9. Sang-Shin Lee, Jong-Uk Bu, Seung-Yeob Lee;,Ki-Chang Song, Chil-Geun Park, Tae-Sik Kim, "Low-power consumption polymeric attenuator using a micromachined membrane-type waveguide," *IEEE Photon. Technol. Lett.*, vol.12, pp.407-409, 2000.

10. Sean M. Garner and Steve Caracci, "Variable Optical Attenuator for Large-Scale Integration," *IEEE Photon. Technol. Lett.*, vol.14, pp.1560-1562, 2002

11. Ying-Tsung Lu, Huang-Chen Guo, Hseng-Tsong Wang, and Sien Chi, "Polymer-based S-shaped Waveguide VOA for Applications in the Broadband DWDM Network," *Microwave and Optical Technol. Lett.*, vol. 39, No. 1, 2003

12. Y.O. Noh, M.S. Yang, Y.H. Won, and W.Y. Hwang, "PLC-type Variable Optical Attenuator Operated at Low Electrical Power," *Electron. Lett.*, vol.36, No. 24, 2000

13. H. Maaty, A.Bashir, B. Saadany, and D. Khalil, "Modeling and Characterization of a VOA with Different Shutter Thickness," *Third Workshop on Photonics and Its Application at Egyptian Engineering Faculties and Institutes*, pp.117 –122, 5 Jan. 2002

14. Barber B., Giles C.R., Askyuk, V., Ruel, R., Stulz, L., and Bishop, D., "A fiber

connectorized MEMS variable optical attenuator," *IEEE Photon. Technol. Lett.*, Vol. 10, pp.1262-1264, 1998.

15. Che-Heung Kim, Namkyoo Park, and Yong-Kweon Kim, "MEMS reflective type variable optical attenuator using off-axis misalignment," *Optical MEMs Conference Digest. 2002 IEEE/LEOS International Conference,* pp.55-56, 2002

16. N. Fukushima, H. Onaka, M. Shirasaki, Y. Suzuki, and T. Tokumasu, "Non-mechanical Variable Attenuator Module Using Faraday Effect," *OAA'96 Technical Digest,* FD9, July 1996.

17. Katsuhiko Hirabayashi, Masato Wada, and Chikara Amano, "Liquid Crystal Variable Optical Attenuators Integrated on Planar Lightwave Circuits," *IEEE Photon. Technol. Lett.*, Vol. 13, No. 6, pp.609-611, 2001

18. Ramanitra, H., Chanclou, P., Vinouze, B., and Dupont, L. "Fibred optical variable attenuator using liquid crystal dispersed in polymer," *Electron. Lett.*, Vol.38, pp.1122-1123, 2002.

19. Qun Li, Amy A. Au, Chien-Hung Lin, E. R. Lyons, and H. P. Lee, "An Efficient All-Fiber Variable Optical Attenuator via Acoustooptic Mode Coupling," *IEEE Photon. Technol. Lett.*, Vol. 14, No. 11, pp.1563-1565, 2002.

20. Mughal, M.J., Riza, and N.A., "Compact acoustooptic high-speed variable attenuator for high-power applications," *IEEE Photon. Technol. Lett.*, Vol.14, pp.510-512, 2002.

21. Davia B. Mortimore, "fiber loop reflectors," *J. Lightwave Technology*, Vol. 6, pp.1217-1224, Jul. 1988.

22. Masood Tabib-Azar, "Integrated Optics - Microstructures and Sensors," Kluwer Academic Publishers, Massachusetts, 1995.

23. Junya Kobayashi, Tohur Matsuura, Shigekuni Sasaki, and Tohru Maruno, "Directional Couplers Using Fluorinated Polyimide Waveguides," *J. Lightwave Technology*, vol. 16, pp. 610-614, 1998

24. Chih-Wei Hsu, Hsuen-Li Chen, and Way-Seen Wang, "Compact Y -Branch Power Splitter Based on Simplified Coherent Coupling," *IEEE Photon. Technol. Lett.*, vol. 15, pp. 1103-1105, 2003

25. David S. Levy, Robert S., York M. Li., and Richard M. O., "A New Design for Ultracompat Multimode Interference-Based 2x2 Couplers," *IEEE Photon. Technol. Lett.*, vol. 10, pp. 96-98, 1998.

Chapter 3

Low-loss Waveguide Crossing Technique

3.1 Introduction

In Section 2.3 of the previous chapter, we introduced a novel single-channel waveguide-based RVOA fabricated with polymeric materials. A multi-channel RVOA or RVOA array is more attractive for gain equalization of EDFAs in DWDM systems. This could be implemented more readily with the polymer waveguide-based RVOA approach rather than with the fused fibre coupler approach. However, to fabricate RVOA array with high channel count, the waveguides will inevitably intersect each other. Therefore, it is important to study the effect of crossing waveguides and the associated insertion loss. As wafer space is a premium, the size of the crossing waveguides will be translated directly to device cost. Ideally, the structure of a crossing waveguide technique should occupy small wafer space and has low insertion loss. Taper width technology [1] is often used for designing waveguide crossing structures. Recently, Stuart [2] introduced multimode interference (MMI) lenses in waveguides to achieve low-loss slab propagation. Although the self-imaging properties of MMI are well-known and commonly

employed in planar lightwave circuits [3] to make compact power splitters [4,5], combiners, and Mach Zehnder interferometers [6] with good tolerance to fabrication errors, the application of MMI structures to attain low-loss waveguide crossing has only recently been studied.
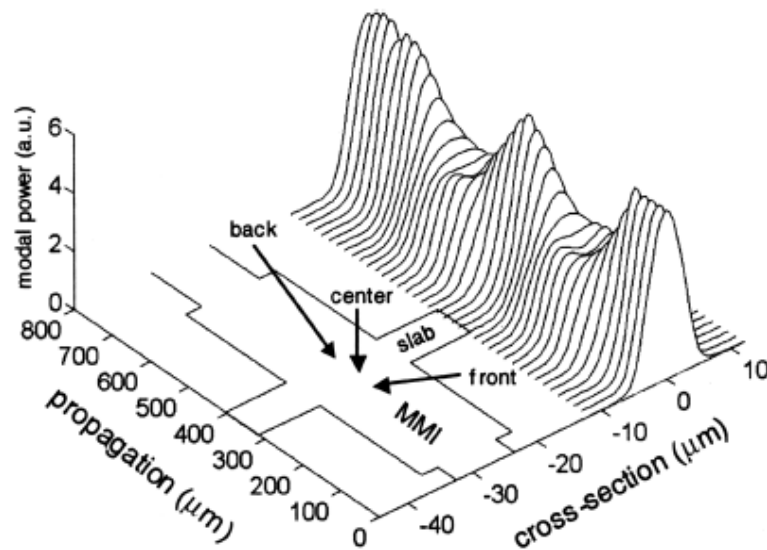
Fig. 3.1   A 9 μm-wide feed waveguide couple to a 14 μm-wide MMI waveguide and then back to a 9 μm-wide waveguide [2].   In the right of the picture, the power distribution along the waveguide is shown.

In Stuart's reported technique, a nearly ideal 2-D focusing Gaussian beam is realized by using the fundamental mode and the next higher even mode with $1:\sqrt{0.058}$ power ratio and -0.73π phase difference in a MMI structure as shown in Figure 3.1. Then this focusing Gaussian beam propagates along the MMI waveguide through focusing before the focal length (or centre) and diverging after the focal length.   The cross slab can be introduced in the centre of waveguide without interfering the Gaussian beam.   In this technique, strong relationship exists between the index delta,

MMI waveguide length, MMI waveguide width and the slab width for low-loss slab propagation and therefore presents a restriction to the slab width for a given index delta.

In this chapter, we introduce an alternative design technique also using MMI structures to attain low-loss slab propagation to relax the aforementioned restriction. The self-imaging property of the MMI structure will be explained and the simulation results showing the evolution of the 1/e width of the optical field propagation along the MMI length using the Rsoft$^{®}$ BeamProp's two-dimensional beam propagation method (BPM) [7, 8] will be described. Then the proposed new design technique using MMI structures for the realization of low-loss waveguide crossing and the simulation results will be presented to demonstrate its advantages over the taper technique. Finally, the application of the proposed technique to realize low-loss small angle intersection will be described.

3.2   MMI Structure and Its Application in Waveguide Crossing

The self-imaging property of the multimode interference (MMI) waveguide means that an input field profile can be reproduced in single or multiple images at periodic intervals along the propagation direction of the guide [3]. With this effect, MMI structure can be used to realize the low-loss waveguide crossing when the waveguide crossing is in the self-imaging place of the MMI waveguide, as shown in Figure 3.2.

Consider the waveguide shown in Figure 3.2, with a cladding refractive index, n_{ci}, of 1.5 and index delta (n_{core} - n_{ci})/n_{ci} of 2%, where n_{core} is the core refractive index, at a wavelength of 1.55 µm. The initial waveguide has a width of 5 µm, which connects abruptly to the MMI region and excites the higher order modes. The width of the MMI region is 7.5 µm and supports the three lowest TE modes. However, a fundamental mode propagates from the initial waveguide to the MMI region only excites the even modes, i.e. TE_0 and TE_2, due to the structure symmetry. Using overlap integral for the modes of the initial waveguide and MMI region, the coupling efficiency from the TE_0 of the initial waveguide to the TE_0 and TE_2 modes of the MMI region were found to be 95% and 4.8%, respectively. The total coupling efficiency from the initial waveguide to the MMI region is therefore 99.8%, indicating a loss of only 0.009 dB to the unguided modes. The effective refractive index of the TE_0 and TE_2 modes in the MMI waveguide is 1.5277 and 1.5100, respectively. Therefore, for 1.55 µm wavelength light, the beat length, L_B, between the two even modes of the MMI waveguide is given by $2\pi/(\beta_0 - \beta_2)$ and in our case is 87.6 µm. As a consequence of the self-imaging properties of multimode waveguides, the two modes would reform the image of the excitation mode periodically at mL_B, where m is an integer, behaving similar to that of a self-focusing graded index waveguide.
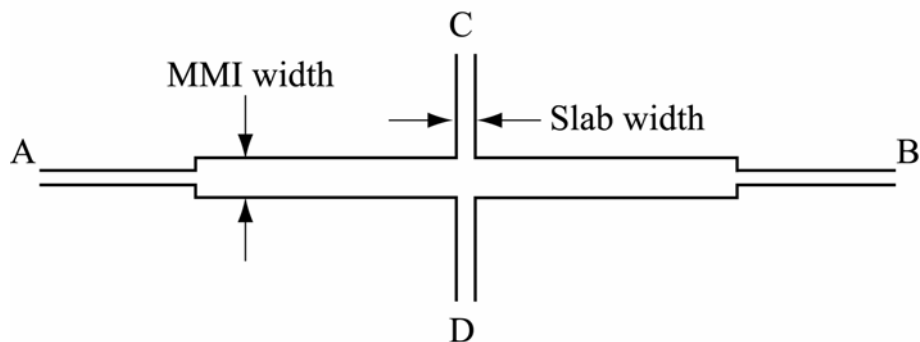
Fig. 3.2   A 5 μm-wide feed waveguide couple to a 7.5 μm -wide MMI waveguide and then back to a 5 μm -wide waveguide [A-B].   In the middle of the MMI waveguide, a crossing waveguide [C-D] is inserted.

Figure 3.3 shows the 1/e width of the optical field propagating in the single mode waveguide and the MMI waveguide as shown in Figure 3.2, obtained using two-dimensional BPM simulations [7].   The length of the initial waveguide is 50 μm and the length of the MMI waveguide is 175.2 μm (2 times of L_B).   The 1/e width of an optical field changes periodically, which increases and then decreases to the smallest value in the middle of the MMI waveguide, which is the single image reformed position.   The smallest 1/e width of the optical field is 5.19 μm, which is slightly larger than the 5.08 μm, the 1/e width of the optical field in the initial 5 μm width waveguide, but is more than 44 % smaller than the width of the MMI waveguide.   At that position, the waveguide width (i.e. the MMI structure width) is larger than the 1/e width of the optical field and little optical power exists around the sides of the waveguide.   Therefore, any perturbations immediately outside the waveguide around this region would have little effect to the propagation of the optical field and low-loss slab propagation could be achieved when a slab is introduced to this region.   If we assume optical field with 1/e width less than the MMI structure

width could propagate through the middle region of MMI waveguide with negligible loss, even though there is no lateral guiding mechanism, then a slab region introduced into this region could have widths of up to about 50 μm, as observed from Figure 3.3, which can be used to realize low –loss waveguide crossing.
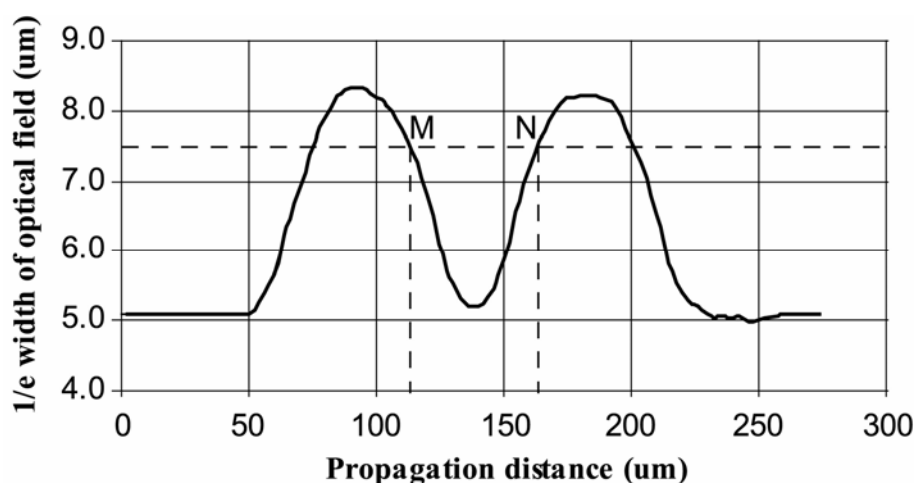
Fig. 3.3   Evolution of the 1/e width optical field propagating from A to B of the waveguide shown in Figure 3.1

3.3   Waveguide Crossing Using MMI Structure

According to our proposed new waveguide crossing technique, which use an MMI structure, low-loss crossing can be achieved by placing the cross waveguide in the position where the 1/e width of the feed optical field is smallest, i.e. at mL_B, as shown in Figure 3.3.   To make short waveguide length, the L_B length position (i.e. $m = 1$) of the MMI is selected for intersection.   Figure 3.4 shows the two-dimensional BPM simulation results which indicates that low-loss slab crossing of less than 0.1 dB can be achieved even with slab width as wide as 80 μm.   However, for slab crossing

without the MMI structure, loss of more than 0.1 dB would occur even with slab

width of 8 μm.   This simulation results show that the slab width can be varied over a

fairly large range without introducing significant insertion loss.
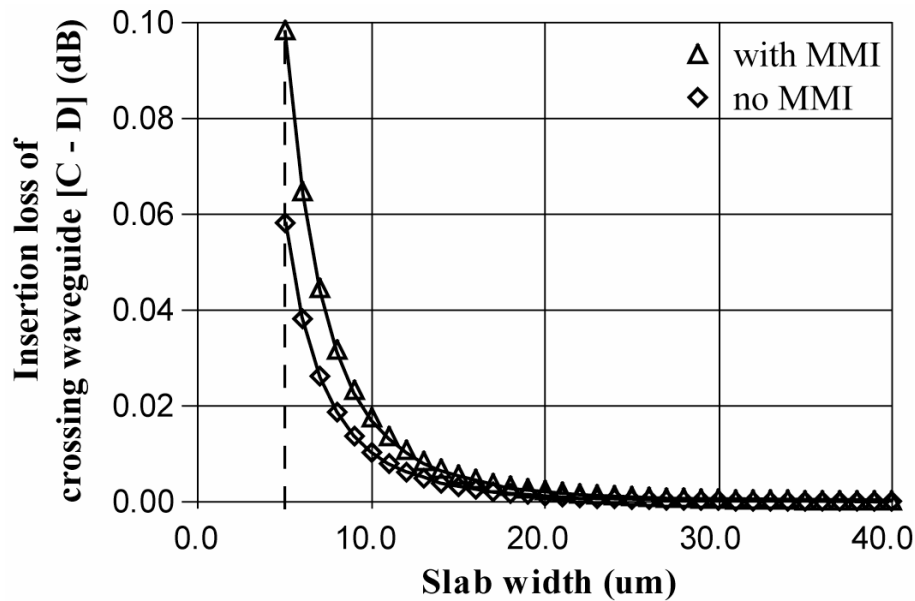
Fig. 3.4   Insertion loss of the feed waveguide [A-B in Figure 3.1] versus slab waveguide
widths with (triangle dots) and without (diamond dots) the MMI structure.

The additional loss incurred by the introduction of the MMI structure to the crossing

waveguide was also evaluated using two-dimensional BPM simulations.   Figure 3.5

shows the insertion loss of the crossing waveguide of different widths with (triangle

dots) and without (diamond dots) the MMI structure.   The additional loss introduced

to the crossing waveguide is less than 0.01 dB when its width is greater than 9 μm.

However, for slab width less than 9 μm, the insertion loss increases rapidly.   This

problem can be overcome by introducing an MMI structure to the crossing waveguide

as   well.   Coupling   loss   is   induced   by   radiation   mode   coupling   at   the

MMI-waveguide junctions and it increases when the MMI width increases. In this study, the slab width is chosen to be equal to the MMI width as shown in Figure 3.3 and varied between 7 μm to 9 μm. The results presented here are also true for waveguides with different refractive index delta, except that low index delta waveguide has longer focus length.
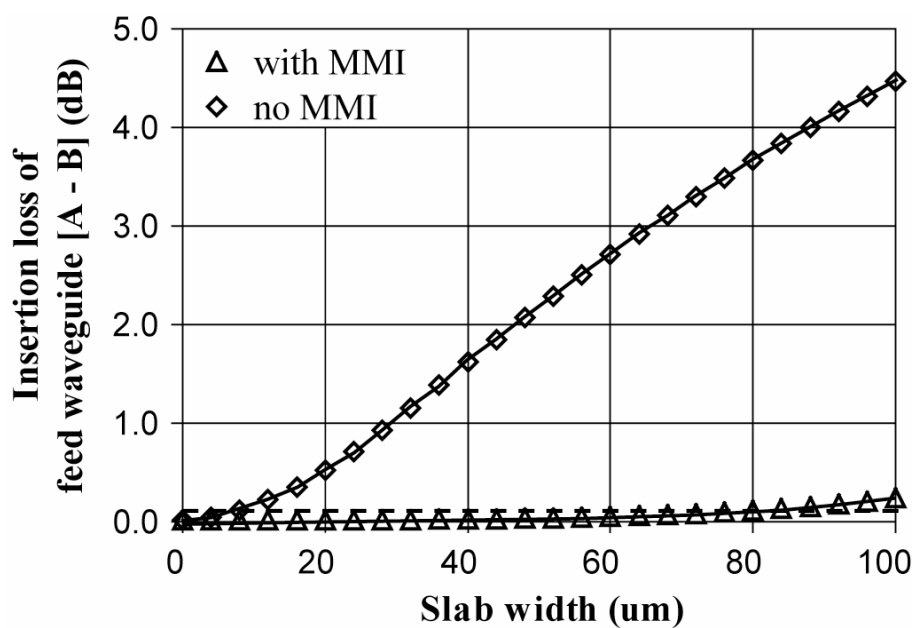
Fig. 3.5   Insertion loss of the crossing waveguide [C-D in Figure 3.1] versus slab waveguide widths with (triangle dots) and without (square dots) MMI structure.

The wavelength dependent loss of the complete structure was also simulated and the result is shown in Figure 3.6. In this case, the width of the crossing waveguide is the same as the MMI width. Increase of the insertion loss with wavelength is expected because the 1/e width of the optical field is larger for longer wavelength. The loss increase from 1530 nm to 1570 nm is less than 0.015 dB, indicating that this structure is fairly wavelength-independent.
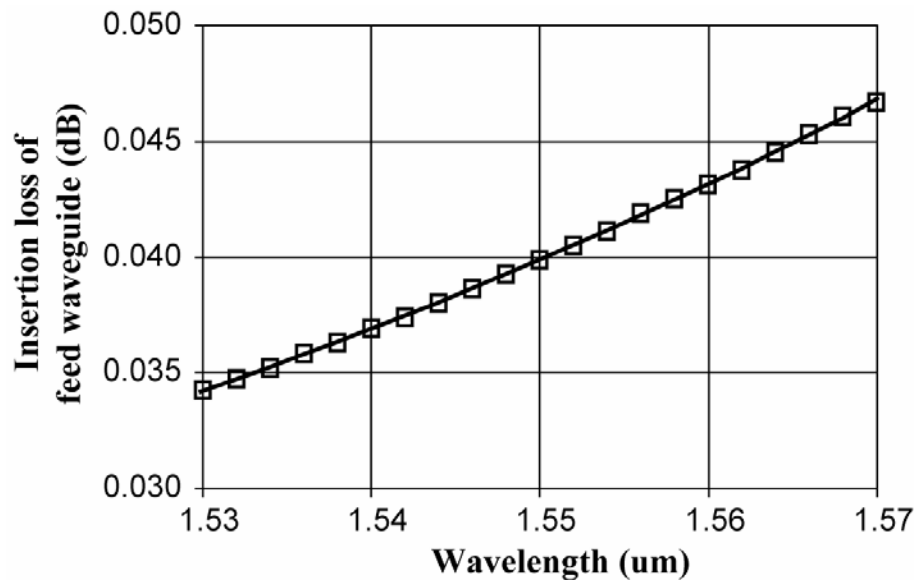
Fig. 3.6   Insertion loss of the MMI structure shown in Figure 3.1 versus transmission wavelength.

Moreover, the MMI width used for waveguide crossing can also be changed.   Table 3.1 lists the beat length, coupling loss and slab loss of MMI structures with width between 7 μm to 9 μm.   In all cases, the length of the MMI structure is kept at twice of that of the beat length and the width of the feed waveguide and index delta are 5 μm and 2 %, respectively.   The slab loss, which is mainly induced by the radiation mode coupling at the MMI-waveguide junctions increases slightly when the width of MMI structures is changed from 7 μm to 8.5 μm.   This simulation results also show that a nearly ideal Gaussian beam [2] is not necessary to attain low-loss, thus permitting larger tolerance in the length of the MMI structure.

Table 3.1 Insertion loss of MMI structures for low-loss slab crossing
(The slab length is 2 times the beat length.)

MMI width (um)	Beat length (um)	Coupling loss (dB)	Slab Loss (dB) (slab width = MMI width)
7	79.5	0.016	0.018
7.5	87.6	0.018	0.019
8	96.2	0.018	0.019
8.5	105.6	0.020	0.024
9	115.4	0.024	0.031

3.4   Comparison of the MMI Structure with the Taper Width Structure

In the following section, we compare the performance of the MMI cross-slab structure as shown in Figure 3.7 (a) with one that employed the taper width technology [1] which is commonly used to minimize intersection loss in waveguides.   It uses two tapers to taper up to a wide waveguide and then taper down again to a narrow waveguide.   The schematic of a cross waveguide using taper width technology to reduce loss is shown in Figure 3.7 (b).
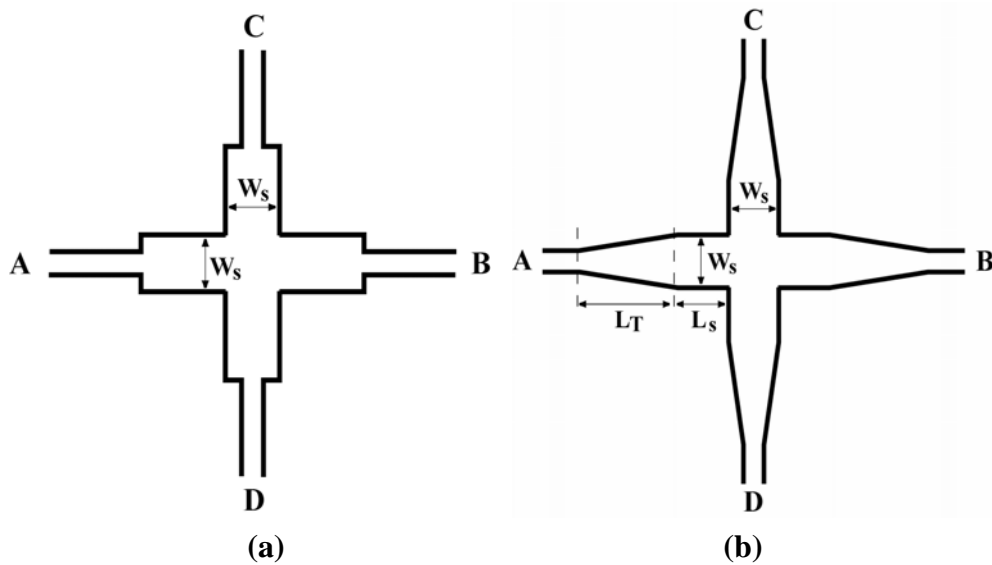
Fig. 3.7   (a) The structure of a cross waveguide with MMI structure to improve insertion loss.
              (b) The structure of a cross waveguide using taper width technology.

Using the same index delta as described in the previous section, we first determine the

insertion loss at the intersection of crossing waveguides without an MMI structure or

tapering.   The insertion loss was calculated to be 0.058 dB for 5 µm-width

waveguides and is indicated in Figure 3.8.   We used the same slab width, W_S, for the

waveguides at the intersection region for both cases (refers Figure 3.6 (a) and (b)) to

minimize the insertion loss.   In the tapered case, a taper length, L_T, of more than 140

µm was employed so as to achieve adiabatic coupling and the slab length, L_S, was

chosen to give the least loss (for example, $L_S = 52$ µm for $W_S = 7.5$ µm).   The

insertion loss of waveguide intersections that employ a MMI structure or taper width

structure with difference slab widths are shown in Figure 3.7.   The simulation results

show that the insertion loss is smaller for a taper width structure if the slab width is

greater than about 8.5 µm.   With a narrower slab width, however, the MMI structure

offers a lower insertion loss and could be 100 % better than the taper width case when the slab width is about 7 µm.
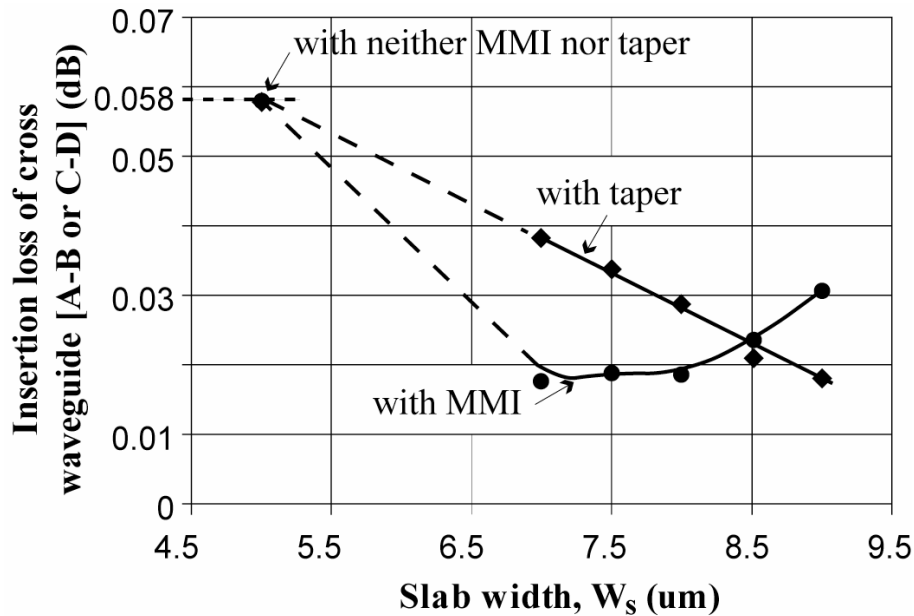
Fig. 3.8   Insertion loss of the cross waveguide [A-B or C-D in Figure 3.6] versus slab waveguide widths with MMI (circle dots) and with taper (diamond dots) structure.

The mechanism of the propagation for the optical field crossing the waveguide for the MMI structure and taper width structure are quite different.   The optical field in the MMI structure is refocused in the centre of the intersection of the waveguides and has a narrow optical field, whereas in the taper width structure, the mode field is expanded and some optical power is lost to the crossing waveguide.   Therefore losses mainly occurred in the waveguide-MMI junction for the MMI structure case but in the taper width case, it occurred in the intersection region.   The taper length is also fairly long (>140 µm in our case), so the taper width structure shown in Figure 3.7 (b) is about four times that of the MMI structure shown in Figure 3.7 (a).   In

practice, a narrower slab width and smaller structure size are preferred as they provide

a saving in the premium substrate estate. In our analysis, we did not consider any

material absorption loss; however, because of the much longer taper length, the taper

width structure will suffer even more loss in comparison to the MMI structure case.

3.5 Angled Intersection with the MMI Structure

Low-loss waveguide crossing with angle of intersection of less than 45° is crucial for

increasing the density of planar light-wave circuits. In this section, we demonstrate

that MMI structures could be employed in small angle crossing to improve the loss

performance. Figure 3.9 (a) and (b) show the cross waveguides with an intersection

angle of θ^o without and with the 7.5 µm-wide MMI structure, respectively.

(a)   **(b)**
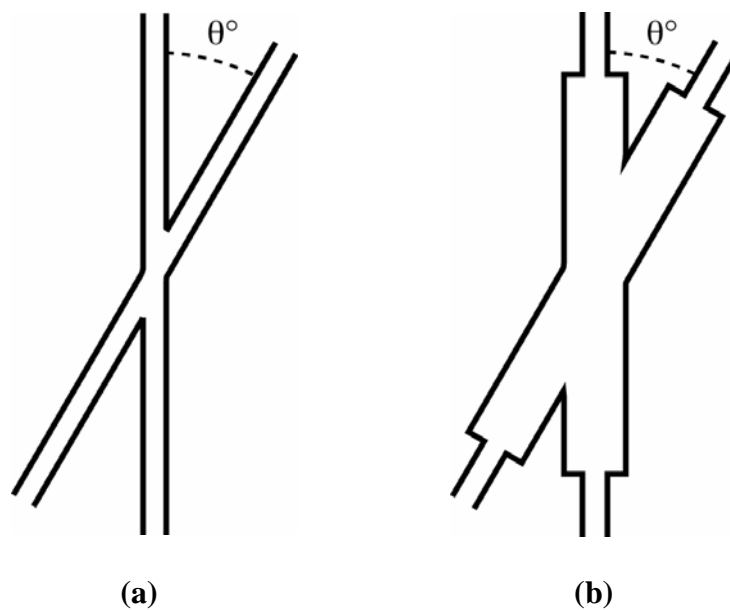
Fig. 3.9   (a) Crossing waveguides intersect at an angle of θ^o.   (b) Crossing waveguides with MMI structure intersect at an angle of θ^o.

Results obtained from wide-angle two-dimensional BPM simulations [8, 9] for the two cases are shown in Figure 3.10. As expected, the loss increases with decreasing θ^o, because more power is coupled to the adjacent waveguide. Without the MMI structure, the insertion loss is about 0.12 dB when θ^o is decreased to 40°. However, with the aid of the MMI structure, the performance improved significantly and for the same loss the angle can be decreased to as small as 23°. Another concern in crossing waveguide is the crosstalk. Simulation results in Figure 3.10 show that crosstalk of better than 30 dB is achievable when the intersection angle is greater than 17° and this is increased to about 37 dB when the angle is 23°. These results show that MMI structures provide a practical solution for waveguides with an angle of intersection as small as 20°.
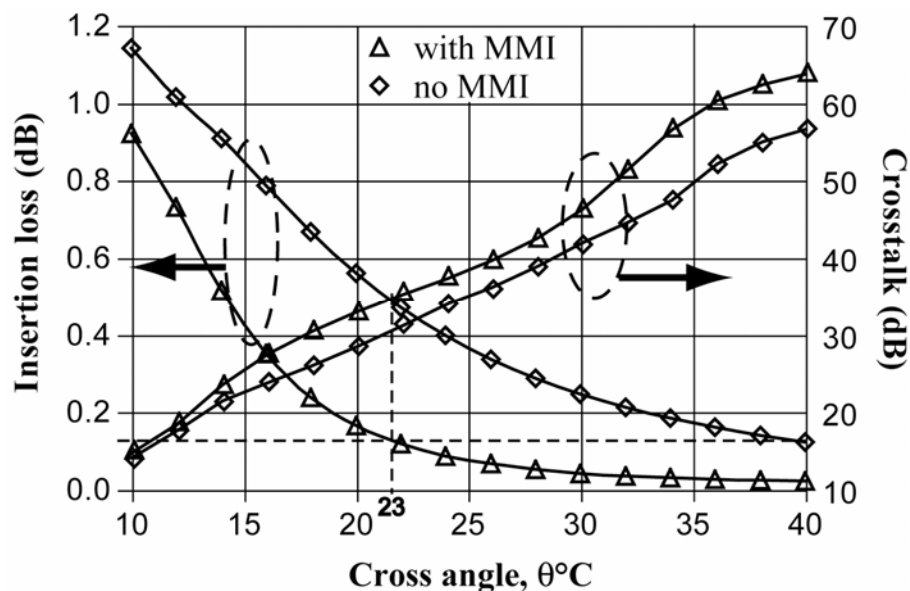
Fig. 3.10   Slab propagation loss and crosstalk versus cross angle for the cases shown in Figure 3.9 (a), indicates by diamond dots and in Figure 3.9 (b), indicates by triangle dots.

3.6   RVOA Array Design with MMI Structure Crossing Technique

As shown in Section 3.5, the minimal crossing angle for two MMI structure crossing waveguides can be as small as 20 degree for good crosstalk and acceptable insertion loss, therefore high channel-count waveguide-based RVOA array (refers to Figure 2.14 of Chapter 2) can be integrated in one chip to reduce the premium wafer space using the MMI structure crossing technique.   An example is shown in Figure 3.11. We assumed that the dimensions of the RVOAs in the array are equal and they are arranged such that the position of the next RVOA is displaced by -R/3 in the x- and y-direction, where R is the radius of curvature of the loops.   In this case, for any number of channel-count, the maximum number of overlapping will be 9 channels. In Figure 3.11, a 9-channel waveguide-based RVOA array is shown and the total occupied area is not much greater than that of a single RVOA.   In the following, we will calculate the variation of insertion loss and channel crosstalk among the 9 channels.
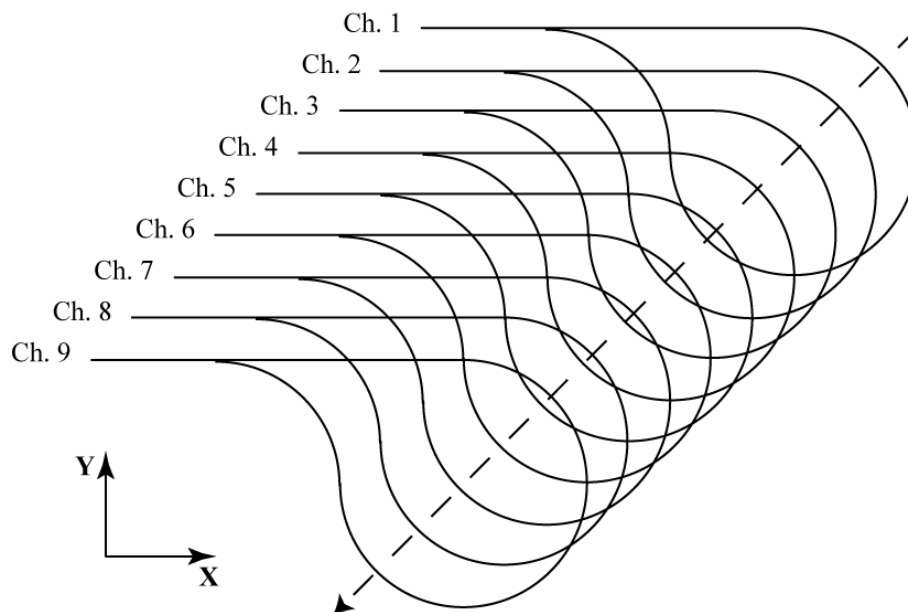
Fig. 3.11 The designed RVOA Array using MMI structure crossing technique

The total insertion loss in each channel is mainly due to waveguide crossing loss and waveguide loss which is directly proportional to the length of the waveguide. Channel 1 of the RVOA array intersects with 4 RVOAs in the array at 8 positions as shown in Figure 3.12.   There are two crossing points (labeled as 1 and 8) between channel 1 and channel 2 and the crossing angles at points 1 and 8 are denoted as angle A and B, respectively, as shown in Figure 3.12.   Since $L_1=L_2=R/3$, it is easy to determine angle A and B as

$$A = \arccos\left(\frac{R - L_1}{R}\right) = 48.2^0 \text{ , and} \tag{3.1}$$

$$B = 2\arcsin\left(\frac{\sqrt{L_1^{\,2} + L_2^{\,2}}}{2R}\right) = 27.3^0 . \tag{3.2}$$

The insertion loss due to waveguide crossing can be obtained from Figure 3.10. The insertion loss at points 1 and 8 are about 0.02 dB and about 0.06 dB, respectively. We assume an insertion loss of about 0.02 dB for crossing angle larger than 40^0. Similarly, we obtain the crossing angles at crossing points 2, 3, 6, 7 and they are 70.5^0, 90^0, 90^0, and 56.3^0, respectively. Therefore, the insertion losses at these points are 0.02 dB each.
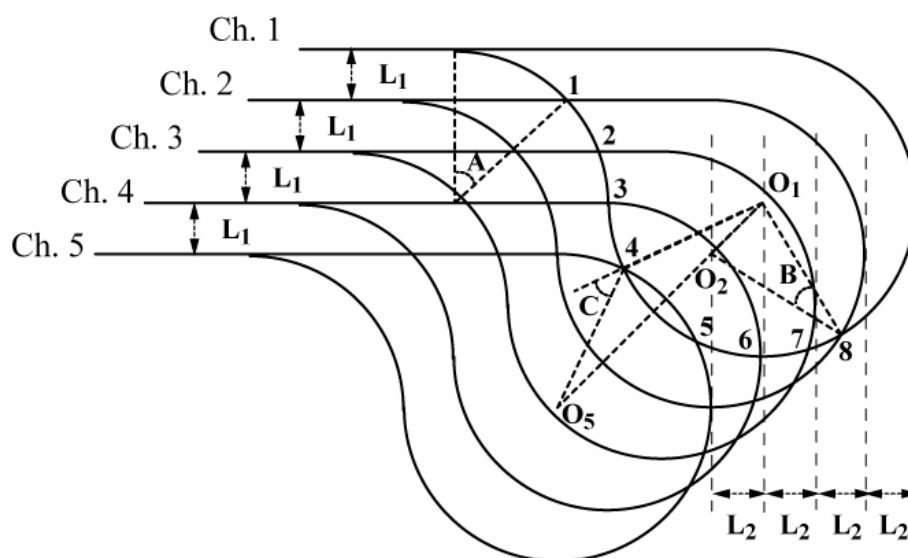
Fig. 3.12   Crossing points of channel 1 in the RVOA array.   For clarity, the MMI structures at waveguide crossings are not shown in the figure.

The crossing angle (C) at points 4 and 5 are equal and can be calculated as

$$C = 2\arccos\left(\frac{\sqrt{(4L_1)^2 + (4L_2)^2}}{2R}\right) = 38.9^0 . \tag{3.3}$$

As determined from Figure 3.10, the insertion loss at points 4 and 5 is about 0.023 dB. Therefore the total excess insertion loss of channel 1 caused by the 8 crossings is about 0.206 dB. The calculated waveguide crossing loss of the 9 channels is listed in Table 3.2. The total insertion loss and total channel crosstalk for each channel are listed in the last 2 columns of Table 3.2. It can be seen that the variation of the insertion loss and channel crosstalk among the 9 channels are 0.206 dB and 3 dB. These values are quite small and thus the uniformity of the RVOA array is quite good in terms of insertion loss and channel crosstalk

Table 3.2 Total excess insertion loss and crosstalk of the channels in a 9-channel RVOA array.

RVOA	Number of crossing	Insertion loss due to waveguide crossing (dB)	Total crosstalk (dB)
Ch. 1	8	0.206	~42
Ch. 2	10	0.286	~39
Ch. 3	12	0.326	~39
Ch. 4	14	0.366	~39
Ch. 5	16	0.412	~39
Ch. 6	14	0.366	~39
Ch. 7	12	0.326	~39
Ch. 8	10	0.286	~39
Ch. 9	8	0.206	~42
Maximum insertion loss and channel crosstalk variations		0.206	3

3.6   Chapter Summary

In this chapter, the self-imaging properties of MMI structures and the negligible effects of the absence of lateral guiding mechanism around the region, where the 1/e width of an optical field in the image reformed region is smaller than that of the MMI region, was explained.   A novel design technique exploits this property of MMI structure to achieve the low-loss waveguide crossing was also described.

Then the waveguide crossing using the MMI structure and the width taper structure was compared in orthogonal waveguide intersections.   Simulation results show the advantages of the MMI structure technique over the width taper structure technique in terms of structure size and insertion loss.

Finally the application of the MMI structure technique in small angle intersection, which is crucial for increasing the density of planar light-wave circuits, is presented. Simulation results show that MMI structure technology could be employed to decrease the angle of intersection while at the same time providing low insertion loss. The design of a RVOA array with nine channels using the proposed technique was also demonstrated.

Reference

1. H. G. Bukkems, C. G. P. Herben, M. K. Smit, F. H. Groen, I. Moerman, "Minimization of the loss of intersecting waveguides in InP-based photonic integrated circuits," *IEEE Photon. Technol. Lett.* vol. 11, pp. 1420-1422, 1999.

2. H. R. Stuart, "Waveguide lenses with multimode interference for low-loss slab propagation," *Opt. Lett.*, vol. 28, pp. 2141-2143, 2003.

3. L. B. Soldano and E. C. M. Pennings, "Optical Multi-Mode Interference Devices Based on Self-Imaging: Principles and Applications," *J. Lightwave Technol.*, vol. 13, pp. 615-627, 1995.

4. T. J. Tayag, D. M. Mackie and G. W. Bryant, "A Manufacturable Technique for Implementing Low-Loss Self-Imaging Waveguide Beamsplitters," *IEEE Photon. Technol. Lett.*, vol. 10, pp. 1262-1264, 1998.

5. L. B. Soldano, F. B. Veerman, M. K. Smit, B. H. Verbeek, A. H. Dubost, and E. C. M. Pennings, "Planar Monomode Optical Couplers Based on Multimode Interference Effects," *J. Lightwave Technol.*, vol. 10, pp. 1843-1850, 1992.

6. R. M. Jenkins, R. W. J. Devereux and J. M. Heaton, "A novel waveguide Mach-Zehnder interferometer based on multimode interference phenomena," *Optics Commun.*, vol. 109, pp. 410-424, 1994.

7. K. Okamoto, Fundamentals of Optical Waveguides, London : Academic, 2000.

8. http://www.rsoftdesign.com/

9. G. R. Hadley, *Opt. Lett.*, vol, 17 1426-1428, 1992.

Erbium-doped Fibre Ring Laser

4.1   Introduction

Wavelength division multiplexing (WDM) systems consisting of up to several hundreds wavelength channels in one fibre is an attractive approach to realize high-capacity optical fibre communication systems demanded by the recent explosive growth in the internet traffic [1].   Reserve laser sources for each of these channels are required to reduce system down time in the event of a primary laser failure. Although each transmitter source does not represent a major cost on its own, it is impractical to stock one or two lasers for each wavelength channel, particularly for WDM systems with high channel-count due to the overwhelming cost and large inventory, which could be many hundreds of lasers.   These issues could be circumvented by stocking much lower number of tunable laser sources whose wavelength cover the entire operating wavelength range of the WDM systems. Furthermore, with the advent of dynamic optical networks requiring wavelength switching and routing, tunable lasers may play a key role as an enabling technology in these systems [2].   Since fibre ring lasers (FRL) exhibit wide tunable range, narrow

---

linewidth and could be tuned at high speed allowing fast component characterization, more and more research is being done on fibre ring laser in recent years [3-21].

In this chapter, the background review about the fibre ring laser will be given, follows by the explanation of the theory of fibre ring laser, which is essential to understand the mechanism in fibre ring laser. Finally, linewidth measurement techniques to measure the narrow linewidth of fibre ring laser will also be described.

4.2   Background Review of FRL

Fibre ring laser has a ring configuration in which some of the output light is feed back to its input. The gain medium in a fibre ring laser can be provided by a section of excited rare-earth ions doped fibre or current-driven semiconductor optical amplifier or a combination of both [22]. Different rare-earth ions, such as erbium, neodymium, and ytterbium, can be used to make fibre ring lasers capable of operating over a wide wavelength range extending from 0.4 to 4 um. For optical fibre communications applications, erbium doped fibre ring lasers (EDFRL) are of interest because they operate in the 1.55-um spectral region, which coincides with the low-loss region of silica fibres. EDFRLs are pumped at 0.98 or 1.48 um wavelength because of the absence of excited-state absorption at these wavelengths. The choice between 0.98 and 1.48 um pump is not always clear since each pumping wavelength has its own merits. Both have been used for developing practical EDFRLs with excellent

performance characteristics.

Fibre ring laser can be broadly divided into continuous wavelength output fibre ring laser and pulsed output fibre ring laser. We focus on the continuous wavelength output fibre ring laser. Wide tunable wavelength range and narrow spectral width are two main important features of EDFRLs.

4.2.1   Tunable Range of FRL

In the early development of fibre ring laser, the wavelength tuning range was focused on the C-band and the largest tunable range was less than 60 nm using EDF pumped with 1480 nm laser diode [3]. With the demand of more information bandwidth and thus more wavelength channels, the wavelength range of fibre ring laser was extended to the L-band by using longer length of EDFs [23]. In 2001, Yamashita *et al.* report about 80 nm (1520-1600 nm) broad tuning range, covering the entire C-band and L-band, using 50-m length of 650 ppm erbium doped EDF pumped with 84 mW of 1480 nm laser diode [4]. In the same year, Bellemare *et al* [5] reported that the tunable range of fibre ring laser can be broadened if the cavity loss is reduced and had experimentally demonstrated a fibre ring laser with about 112 nm (1506.4- 1618.6 nm) tuning range using 27-m length of 6.8×10^{24} ions/m^3 erbium doped EDF pumped with 180 mW from a 980 nm laser diode. The loss-loss cavity was achieved by the integration of optical components as shown in Figure 4.1. As a result of the low

cavity loss (less than 5 dB), the gain required in the laser cavity is therefore small.

Since flat-gain over wide wavelength range can be obtained in the deeply saturated

EDFA, large tunable range can be obtained in the laser.
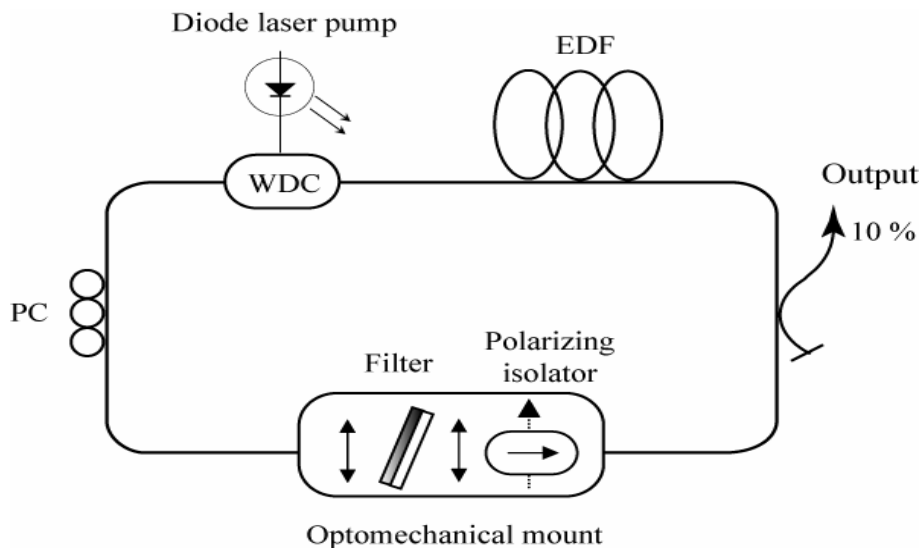
Fig. 4.1   Schematic diagram of the broadly tunable erbium-doped fibre ring laser [5].

Recently X. Y. Dong *et al.* [6] investigated the effects of erbium-doped fibre length

and pair-induced quenching (PIQ) on the tunable range of fibre ring laser and realized

about 102 nm (1514 – 1618 nm) of tunable range by active fibre length switching

method, as shown in Figure 4.2.   One length of erbium-doped fibre (17.5 m) can be

switched into the ring cavity by using a 1x2 fibre-optic switch.   Since longer active

fibre length extends the lasing wavelength into the longer wavelength, the total output

tuning range is broadened.   The main drawback of this technique is that wavelength

tuning is not entirely continuous.
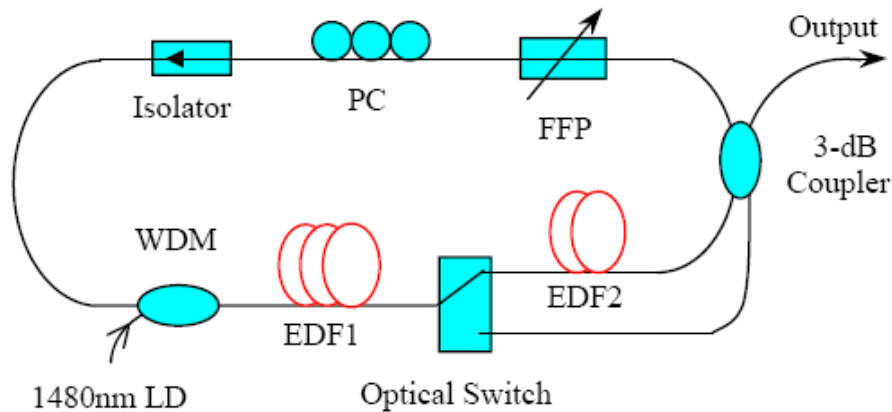
Fig. 4.2   The laser configuration reported in [6] to extend wavelength tuning range by EDF length switching.

4.2.2   Switchable FRL

Discretely wavelength tunable fibre lasers with emission light centred at the ITU frequency grid are useful for WDM systems.   They can be realized by step-tuning an optical filters or inserting a comb filter in the laser cavity.   T. Haber *et al.* [7] reported a thermally controlled fibre Fabry-Perot interferometer with 50-GHz ITU frequency grid in the cavity to realize the discretely tunable function and 50 nm tunable ranges was obtained with 0.4 nm wavelength spacing.   C. H. Yeh *et al.* [8] reported a laser whose output wavelength could be tuned with 1.12 nm steps by inserting a FP-LD in the laser cavity and 31.36 nm tunable ranges was obtained.

Y. W. Lee *et al.* [9] realized a two switchable-wavelengths output by using a long-period fibre grating written in the polarization maintaining fibre, as shown in

Figure 4.3. Due to the birefringence of the polarization maintaining fibre and the codirectional mode coupling of the long-period fibre grating, the long-period polarization maintaining fibre grating device (LP-PMFG) has different wavelength-dependent loss band at different polarization states and the two resonant wavelengths can be obtained at the orthogonal polarization conditions. Using another two FBG filters of these resonant wavelengths in the cavity, one wavelength laser output can be obtained by adjusting the polarization controller to introduce large insertion loss at the other wavelength. However, the number of switchable wavelengths attained with this laser is limited.
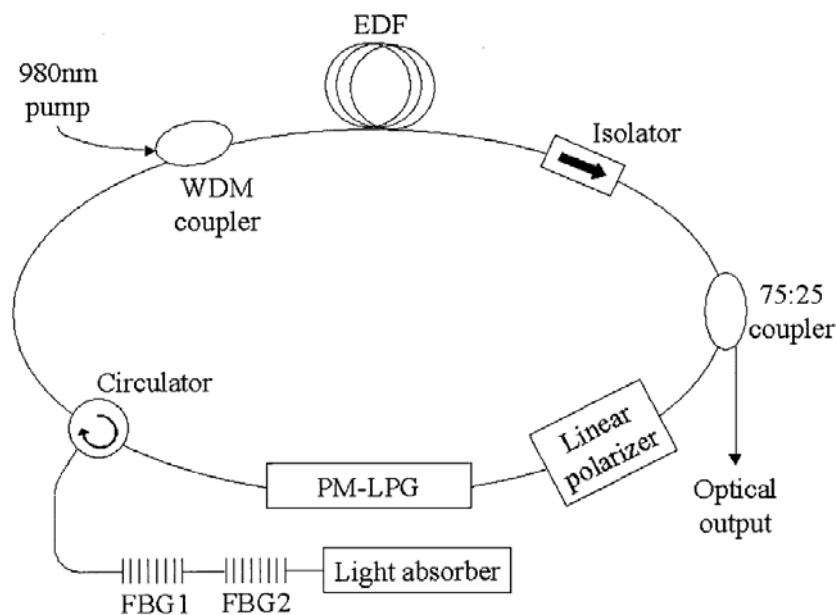
Fig. 4.3   Configuration of the two wavelengths switchable FRL using LP-PMFG [9].

M. Delgado-Pinar *et al.* [10] realized a wavelength-switchable fibre ring laser using a fibre Bragg grating modulated with an acoustooptics superlattice modulator (FBG-AOSLM). The laser configuration is shown in Figure 4.4. Since the

extensional acoustic wave propagating along the grating produces the periodic

stretching and compression of the FBG, which modulated the index profile of the FBG,

additional sidebands reflection appear on both sides of the original wavelength.   The

wavelength shifts of the different order sideband reflections are determined by the

acoustic frequency and the peak reflectivity depends on the amplitude of the acoustic

wave.   Wavelength switching was achieved by controlling the amplitude of the

acoustic wave and the wavelength spacing can be adjusted by changing the frequency

of the RF signal.   Three wavelengths-switchable outputs with 0.14 nm spacing were

obtained under three different amplitudes of the 1.017 MHz acoustic frequency.   But

the spacing range is limited by the low coupling efficiency of RF signal at high

frequency and the reported maximum wavelength shift for the first-order sideband is 3

nm [11].
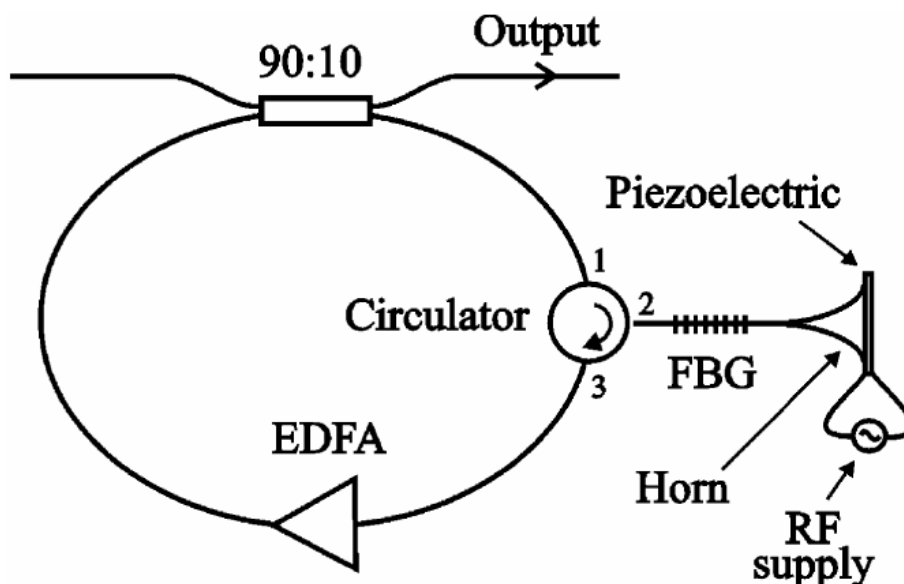
Fig. 4.4   Configuration of the wavelength-switchable FRL using FBG-AOSLM [10].

Recently L. Su *et al.* [12] realized a wavelength-switchable fibre ring laser using

multi-mode FBG (MMFBG), as shown in Figure 4.5. The fibre laser is able to switch between 31 wavelengths ranging from 1532.62 nm to 1556.43 nm with 0.8 nm spacing and the signal-to-ASE noise ratio is greater than 40 dB. The emission wavelength is determined by the effective refractive indexes of two adjacent mode groups. Since the distribution of the reflected power at different wavelengths is determined by the spatial distribution of the MMF modes, different wavelength spectra can be obtained by varying the launching position of the single-mode fibre against the multimode fibre Bragg grating. The main drawback of this laser is that it is very sensitive to the axial displacement between the SMF and the MMF.
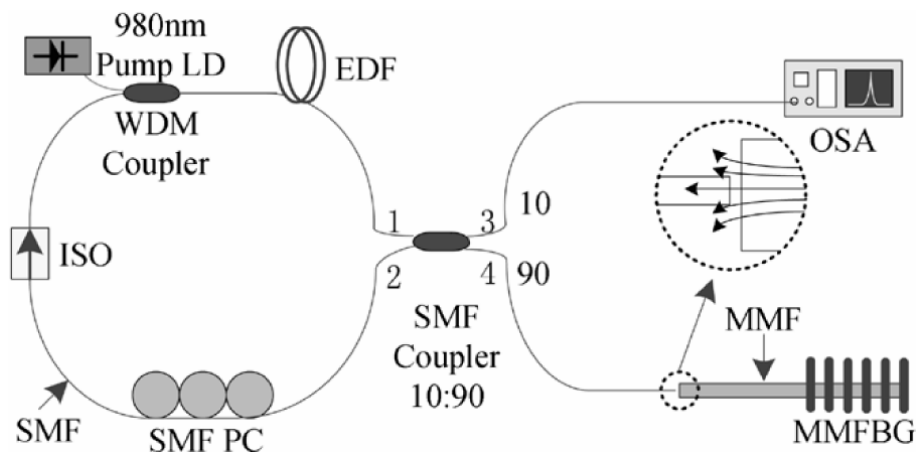
Fig. 4.5   Configuration of wavelength-switchable fibre ring laser based on MMFBG [12].

4.2.3   Single Longitudinal Mode FRL

Generally, the output of fibre ring lasers is multi-longitudinal mode because of the long cavity length. FRL would need to operate in single-longitudinal mode if narrow linewidth spectrum is required. One way to realize single-longitudinal mode

operation is to use a very narrow optical bandpass filter with bandwidth narrower than the wavelength spacing of the longitudinal modes. Another laser configuration to realize single-longitudinal mode operation is using a compound-ring cavity, as shown in Figure 4.6 [13]. Due to small ring length, dual-coupler fibre ring (DCFR) acts as a small FSR etalon filter, which combines with the tunable optical bandpass filter to select one longitudinal mode.
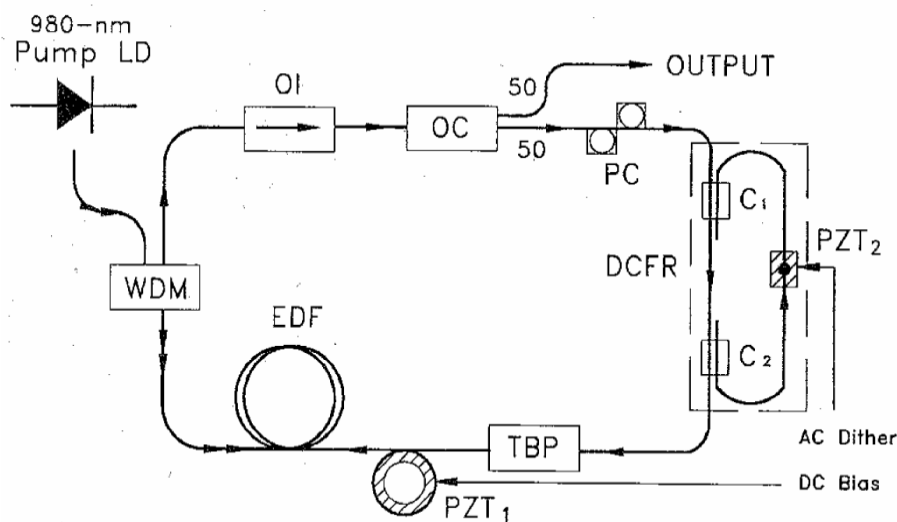
Fig. 4.6   Configuration of an SLM compound-ring laser [13].

Many co-workers reported [14-18] single-longitudinal mode operation of FRLs by using unpumped EDF as saturable-absorber based narrow-band filter. Different fibre laser configurations using unpumped EDF to realize single-longitudinal mode operation, such as combining with mirror [14], FBG filter [15-17] and 3-dB coupler [18], have been demonstrated. The principle of unpumped EDF acting as a narrow-band reflection filter is shown in Figure 4.7 [19]. When the frequency

difference is smaller than the cutoff frequency of the erbium-ion dynamics (including zero), these two frequency sources cooperatively form an interference pattern in the unpumped EDF which results in spatial hole burning (SHB). Since EDF exhibits absorption saturation effect, the absorption coefficient is smaller at the higher intensity parts of the interference pattern than that at the lower-intensity parts and the net absorption become minimum when two frequencies is equal. Therefore, the standing-wave saturation effects in the unpumped EDF can be used to form narrow-band reflection filter, which confines the lasing wavelength to a single-longitudinal mode.

Uniform intensity (uniform absorption coefficient)

I_1
f_1

I_1

I_2

I_2
f_2

(a)

Higher intensity (lower absorption coefficient)

I_1
f_1

$I_1 + I_2$

I_2
f_2

Lower intensity (higher absorption coefficient)

(b)
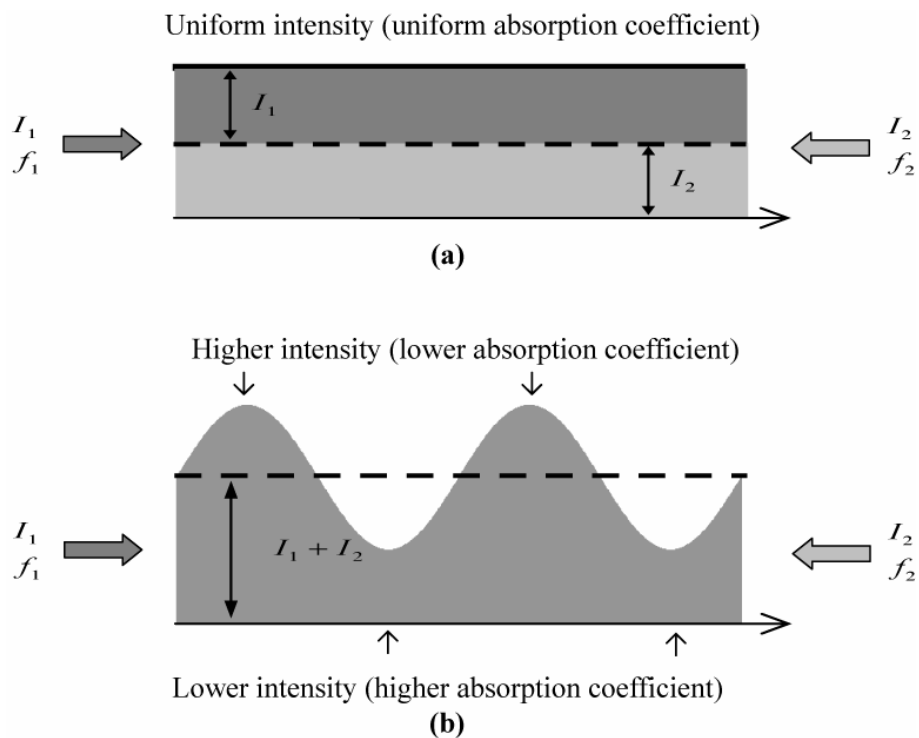
Fig. 4.7   Frequency dependent intensity distribution in unpumped EDF [19].   (a) Larger net absorption without SHB (frequency difference larger than the cutoff frequency).   (b) Smaller net absorption with SHB (frequency difference smaller than the cutoff frequency)

L. Xu *et al.* [20] demonstrated single-longitudinal mode operation FRL by inserting a SOA in a ring cavity, as shown in Figure 4.8. SOA can acts as a high-pass optical filter [21] because of its relatively fast carrier recovery rate and the gain saturation effect. Since the beating noise frequency related to the longitudinal modes is primarily in low-frequency region due to the long cavity length and hence narrow frequency separation between the different modes, the introduction of SOA in the ring cavity can dramatically suppresses the low-frequency induced by longitudinal modes beating and realizes the single-longitudinal mode operation.
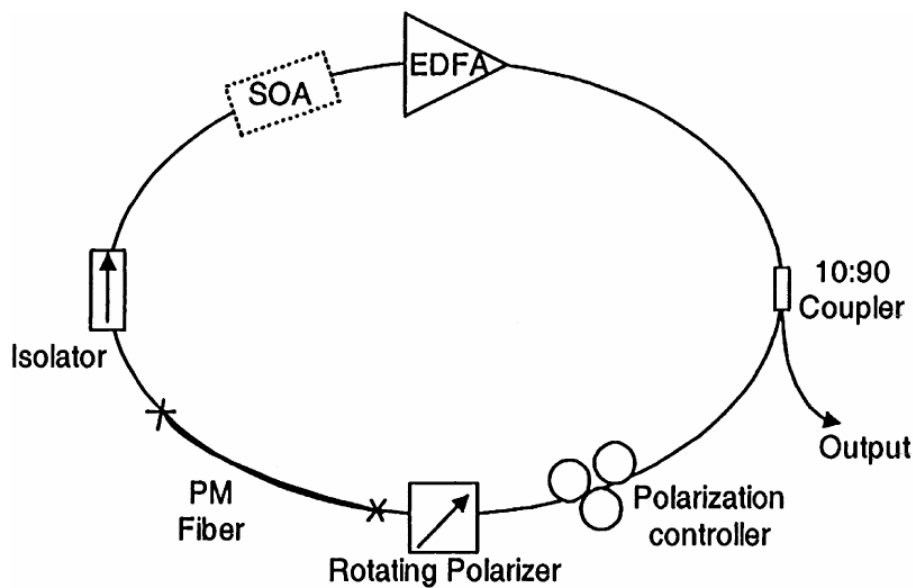
Fig. 4.8　Configuration of an SLM FRL with SOA [20].

4.3　Theoretical Modeling of FRL

In this section, the theoretical background of FRL will be explained. A schematic diagram of a fibre ring laser using bandpass optical filter is shown in Figure 4.9,

which has both forward and backward pumps that may be of the same or different wavelengths. The amplification medium in fibre ring laser is usually a piece of erbium-doped fibre, made from different glasses that act as hosts for erbium ions. The most common host is silica, but fluoride, tellurite and bismuth-based glasses are also used. These hosts and co-dopants may provide additional benefits, such as higher bandwidth, flat gain or gain in other wavelength regions. Co-doping with Yb^{3+} ions (ytterbium) can improve energy transfer from the pump to the signal for 980 nm pumping wavelength.
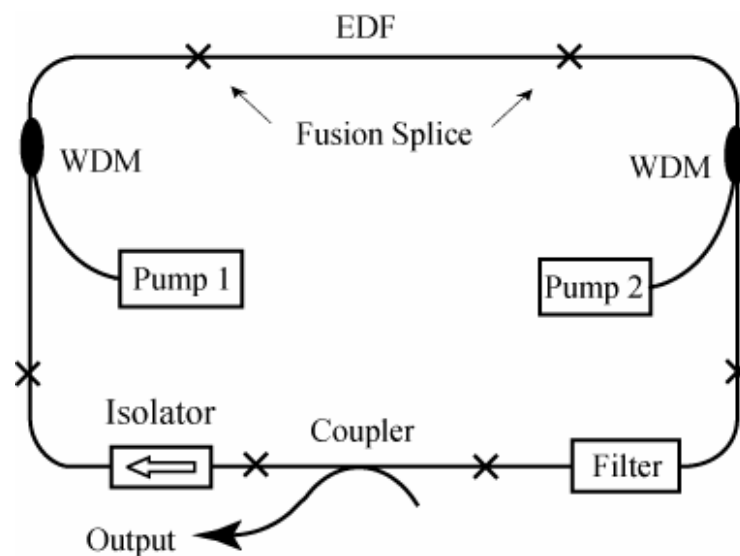
Fig. 4.9   A general configuration of fibre ring laser.

Many theoretical models are use to simulate fibre ring lasers. The erbium-doped fibre theoretical model adopted in this work is based on the Reference [24] used for modeling erbium doped fibre amplifiers. The EDFRL is described in an (r, f, z) cylindrical coordinate system with the z axis as the fibre axis. In this model, erbium

ions are described in a homogeneous two-level system approximation: the ground state, $^4I_{15/2}$ and the upper laser level, $^4I_{13/2}$. For pumping into the 980-nm absorption band, if the rapid transfer of the pump population to the excited state 2, the pump level 3 of the 3-level system remains nearly empty, i.e., the population in the $^4I_{11/2}$ manifold is negligible; hence a 2-level system can be considered. This assumption is valid for Si-EDF and Bi-EDF systems whereby the ion lifetime at the pumping level is much shorter than that at the metastable level.

To achieve high gain in silica glass fibre, high erbium ions concentration in Si-EDF was developed. But unfortunately, erbium ions are not very soluble in silica fibres and at such high erbium concentrations, ion clustering occurs. Therefore in high erbium-concentration silica-based fibres, the distance between erbium ions is small and electric dipole–dipole interactions between the different ions take place. The interaction strength is proportional to $1/r^6$, where r the distance between two erbium ions [25]. Due to the interactions of erbium ions in the EDF, high erbium concentration EDF results in reduced gain. Consequently, high erbium concentration EDFs are susceptible to gain quenching or concentration quenching. Several mechanisms of interaction are possible, such as upconversion between independent dopant ions, pair-induced quenching (PIQ), excited state absorption (ESA) etc. [26]. The upconversion process, also referred to as cross relaxation [27 - 29], is a result of nonradiative energy transfer owing to electric multipolar interactions, as shown in Figure 4.10. It starts with two erbium ions in the excited state, as shown in Figure

4.10 (a). As an effect of the interaction, one of the ions transfers its energy to the other promoting it to a higher energy state while the original ion decays to the ground state, as shown in Figure 4.10 (b). The ion that has transferred to the higher state rapidly relaxes down to the metastable state again where it can be used for amplification, as shown in Figure 4.10 (c). Only about 1/10,000 of the upconverted ion decay radioactively to the ground state, which is sufficiently small and can therefore be neglected in the theoretical model [27]. This process is much faster (one to tens µs [28]) than the pump rate, so the net result of the upconversion is that only one of two initially excited ions remains in the metastable level and can be used for amplification. This obviously leads to a loss in the population inversion and hence causes a decrease in the EDF's gain. Very efficient cooperative upconversion can occur when two (or more) ions form a pair (or cluster); resulting in almost immediate interaction of ions once both of them are excited. This is referred to as pair-induced quenching [30-32], which is confirmed by the observations that even at very high pump powers, there remain an unstable absorption at the pump wavelength, so a full inversion can not be achieved. To explain this, it is assumed that not all ions are independent, but some coupled in pairs. All the erbium ions exist as two distinct species: single ions (non-interacting with one another) and clustered ions. Of the ions that are coupled in pairs, only two states are possible. Either both ions are in the ground state (state 1) or one ion is in the excited state and the other is in the ground state (state 2), and two ions coupled in pair can never be in the excited state together. Therefore the net result is a lower gain because a full inversion is not

achievable. Usually it is assumed that the maximal number of the interacted ions is only two, which is valid when the doping concentration is under 5.5×10^{25} ions/m³, otherwise the behavior of the absorption should be interpreted with larger ion-pair clusters model [33]. When an erbium ion is already excited to the metastable level, it can still absorb a pump or signal photon and be promoted to higher energy levels [34-36]. This process is called excited-state absorption (ESA) and results in a loss of pump or signal power. ESA can be avoided by choosing the right pump wavelengths. For example, pumping at 980 nm and 1480 nm, do not exhibits ESA. Furthermore, in low erbium concentration doped-fibre, upconversion, pair-induced quenching and excited-state absorption can be disregarded.

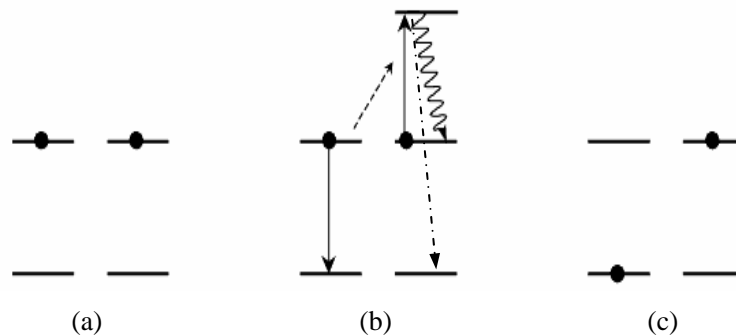Fig. 4.10   Upconversion process between two erbium ions: (a) initial state, (b) ion interaction, (c) final state

Ignoring the interactions of erbium ions in EDF, the effects of pump, signals and ASE intensities on the atomic population densities N_1 and N_2 (averaged over EDF cross section) at the ground and metastable energy levels are described by the population rate equations and by the population conservation law [24]:

$$\frac{\partial N_1(z,t)}{\partial t} = -\left[W_{sa}(z) + W_p(z)\right]N_1(z,t) + \left[W_{se}(z) + \frac{1}{\tau_{21}}\right]N_2(z,t), \qquad (4.1)$$

$$\frac{\partial N_2(z,t)}{\partial t} = -\left[W_{se}(z) + \frac{1}{\tau_{21}}\right]N_2(z,t) + \left[W_{sa}(z) + W_p(z)\right]N_1(z,t), \text{ and} \qquad (4.2)$$

$$N_1(z,t) + N_2(z,t) = N_T = const., \qquad (4.3)$$

where N_T is the total erbium dopant concentration in fibre. τ_{21} is the spontaneous emission lifetime of the metastable level. W_{sa}, W_{se} and W_p are the stimulated absorption, emission of the signal and transition rates of the pump respectively. The subscripts of the cited parameters indicate the involved transition levels.

$$W_{sa}(z) = \frac{1}{A_{eff}} \int_0^\infty \frac{\sigma_{12}(v)}{hv}\left[P_{ASE+}(z,v) + P_{ASE-}(z,v)\right]\eta(v)dv \qquad (4.4)$$

$$W_{se}(z) = \sigma_{21}(v_p)\frac{P_p^+(z) + P_p^-(z)}{hv_p A_{eff}}\eta_p + \frac{1}{A_{eff}} \int_0^\infty \frac{\sigma_{21}(v)}{hv}\left[P_{ASE+}(z,v) + P_{ASE-}(z,v)\right]\eta(v)dv$$

$$\qquad (4.5)$$

$$W_p(z) = \sigma_{12}(v_p)\frac{P_p^+(z) + P_p^-(z)}{hv_p A_{eff}}\eta_p, \qquad (4.6)$$

Where σ_{21} and σ_{12} are the emission and absorption cross section of the erbium doped fibre, respectively. h is Planck's constant. $P_p^\pm(z)$ and $P_{ASE\pm}(z,v)$ are the pump powers and ASE power at the frequency v in a frequency interval δv and the longitudinal fibre coordinate z, respectively. The + and - superscripts indicate the forward and backward direction, respectively. A_{eff} is the effective fibre core area, $\eta(v)$ is the overlap integrals between the LP$_{01}$ mode intensity distribution and the

erbium doping density function $\rho(r)$.

$$\eta(v) = \frac{\int_0^\infty \rho(r)|E(r,v)|^2\, r\, dr}{\int_0^\infty |E(r,v)|^2\, r\, dr} \tag{4.7}$$

In Equation 4.7, the overlap between optical mode and excited ions is assumed to be independent on optical power and equal to the overlap between the mode and total dopant distribution.   This effective overlap approximation is generally valid since the dopant ions are well confined to the center of the optical mode and the intensity changes insignificantly over the transverse dopant profile.   Otherwise in the full approach, the transverse distribution of the inversion must be calculated from the radial distribution of the intensity and dopant ion concentration at first, then the overlap between the optical mode and inverted ions is calculated exactly.

In practice, we only consider the stable operation of the fibre ring laser.   So it means the ion distribution does not change with time, i.e., $\dfrac{\partial N_i}{\partial t} = 0$, $i = 1,2$.   Therefore

$$N_2(z) = N_T \frac{W_p(z) + W_{sa}(z)}{W_p(z) + W_{se}(z) + W_{sa}(z) + \dfrac{1}{\tau_{21}}} \tag{4.8}$$

$$N_1(z) = N_T - N_2(z) \tag{4.9}$$

Equations 4.8 and 4.9 describe how the population inversion depends on the signals and pumps propagating in the EDF.   In order to describe the evolution of both

pump$\pm$ and ASE$\pm$ powers (denoted by $P_{p\pm}$ and $P_{ASE\pm}$), along the active fibre, the wavelength spectrum is divided into small frequency slots and the following standard propagation equations applied:

$$u_i^{\pm} \frac{dP_{P\pm}(z)}{dz} = -\gamma_P(z,v_p)P_{P\pm}(z) - l(v_p)P_{P\pm}(z) \text{, and} \qquad (4.10)$$

$$u_i^{\pm} \frac{dP_{ASE\pm i}(z)}{dz} = [\gamma_{se}(z,v_i) - \gamma_{sa}(z,v_i)]P_{ASE\pm i}(z) + mhv_i\delta v_i\gamma_{se}(z,v_i) - l(v_i)P_{ASE\pm i}(z) \qquad ,$$

$$(4.11)$$

where $l(v_i)$ is the background loss of the fibre without doping. δv_i is the width of the ith slot centered at frequency v_i and $P_{ASE\pm i}(z)$ is the power of the amplified spontaneous emission (ASE) or output laser in the frequency interval centered around v_i with δv_i bandwidth. m is the number of guided modes propagating at the signal wavelength, usually $m = 2$. $\gamma_P(z,v_p)$, $\gamma_{se}(z,v_i)$ and $\gamma_{sa}(z,v_i)$ represent the pump absorption, signal absorption and emission coefficients, respectively, determined from the emission and absorption cross sections and the overlap integral between the mode and ground states [24]. $\gamma_P(z,v_p)$, $\gamma_{se}(z,v_i)$ and $\gamma_{sa}(z,v_i)$ are defined as

$$\gamma_p(z,v_p) = \eta(v_p)\sigma_{sa}(v_p)N_1(z) \qquad (4.12)$$

$$\gamma_{se}(z,v) = \eta(v)\sigma_{se}(v)N_2(z) \text{, and} \qquad (4.13)$$

$$\gamma_{sa}(z,v) = \eta(v)\sigma_{sa}(v)N_1(z). \qquad (4.14)$$

In accordance with the setup schematically shown in Figure 4.9, appropriate boundary

conditions are imposed at the beginning and at the end of the active fibre ($z = 0, L$) on the co- and counter- pump power and the individual spectral components of forward and backward propagating ASE powers generated within the EDF.

$$P_p^+ (z = 0) = P_p^+$$
$$P_p^- (z = L) = P_p^-$$
$$P_{ASE+i}^1 (z = 0, v_i) = 0$$
$$P_{ASE-i}^1 (z = L, v_i) = 0$$

(4.15)

Equation 4.10 and 4.11 are a set of coupled differential equations that can be solved numerically by means of an iterative procedure based on the fourth-order Runge-Kutta algorithm whose convergence speed is influenced by the width and hence by the number of slots used for the spectrum discretization [37]. In common amplifier simulation, a uniform step, for example $\Delta\lambda = 0.2$ nm, is chosen. However in fibre ring laser, nonuniform spectrum subdivisions, i.e., outside laser wavelength with large slot width, for example $\Delta\lambda = 0.2$ nm, and near laser wavelength with small slot width, for example $\Delta\lambda = 0.002$ nm, can be used to reduce the simulation time and increase the wavelength resolution.

In order to model the ring laser operation, the output forward and backward ASE signals of the doped fibre amplifier become the boundary condition of the next amplifier iteration run, i.e. the feedback mechanism for the laser configuration [4 - 6, 38, 39]. According to the setup of fibre ring laser shown in Figure 4.9, the

counter-clockwise propagating (-) ASE power is suppressed by the optical isolator, while the clockwise propagating ASE (+) ASE is filtered, attenuated by the loss of the ring resonator and part of it is output via a directional coupler.

$$
\begin{aligned}
P_{ASE+}^{k}(z = 0, v) &= P_{ASE+}^{k-1}(z = L, v)\beta(v) \\
P_{ASE-}^{k}(z = L, v) &= P_{ASE-}^{k-1}(z = 0, v)\beta(v)\beta_{iso}
\end{aligned}
\tag{4.16}
$$

where k in $P_{ASE\pm}^{k}$ denotes the iteration step. $\beta(v)$ represents the total loss of the ring resonator which take into account the insertion loss of all the splicing and passive component, including optical filter, in the ring cavity except the EDF section. β_{iso} is the isolation of the optical isolator. At the output of each loop, the wavelength spectrum is compared, slot by slot, with the input one; the highest relative difference is assumed as the current convergence error. The procedure stops as soon as this error is lower than a given tolerance. After a few iterations, around 10 steps, depending on the EDF length and z-step used in propagation, convergence can be reached and the spectral component corresponding to the resonant frequency of the ring cavity is selected from the initial wideband amplified spontaneous emission noise spectrum.

4.4 FRL Linewidth Measurement Technologies

Laser linewidth is often defined by the full-width half-maximum (FWHM) of the optical field power spectrum and is an important parameter of the laser. A typical

grating-based commercial OSA can only measure 1550 nm spectrum with 0.01 nm wavelength resolution. Wavelength measurement using wavelength meter can achieve better than 1 pm accuracy but wavelength resolution is limited. However, typical linewidth of fibre ring laser is very narrow and can be less than 1 kHz, which is about one million times narrower than the resolution of the typical grating-based OSA. Therefore alternative measurement methods must be used. The alternative methods include the optical heterodyne method [40-42] and the delayed self-heterodyne method [43-45]. These optical mixing methods are capable of obtaining extremely high wavelength resolution required for laser linewidth measurement.

4.4.1 Power Spectrum of Two Stationary Uncorrelated Sources

Suppose two statistically uncorrelated laser sources with different optical carrier frequencies v_1 and v_2 are detected by the photodiode. The two electric fields of the lasers can be written as:

$$E_i\left(t\right) = \mathrm{Re}\{\overset{\omega}{E}_i(t)\} = \mathrm{Re}\{\overset{\omega}{A}_i(t)\exp(j2\pi v_i t)\}, \quad i = 1,2, \qquad (4.17)$$

where $\overset{\omega}{E}_i(t)$ and $\overset{\omega}{A}_i(t)$ are complex parameters. Thus the detector photo-current $I^D\left(t\right)$ can be obtained by lower-pass filtering the mean square total electric field:

$$I^D(t) = I(t) \otimes h_D(t)$$
$$= \eta \{ [E_1(t) + E_2(t)][E_1(t) + E_2(t)] \} \otimes h_D(t), \qquad (4.18)$$
$$= I_1^D(t) + I_2^D(t) + I_x^D(t)$$

where η is the conversion efficiency of photo-detector and $h_D(t)$ is the detector impulse response. The transfer function associated with this impulse response is assumed to have a cutoff frequency which is much lower than the optical frequency. $I_i^D(t)$ (i = 1,2) is the direct intensity detected by photo-detector and $I_x^D(t)$ is the heterodyne mixing cross-term intensity detected by photo-detector.

$$I_i^D(t) = \eta E_i^2(t) \otimes h_D(t) = \frac{1}{2}\eta \overline{E}_i(t)\overline{E}_i^*(t) = \frac{1}{2}\eta \overline{A}_i(t)\overline{A}_i^*(t), \qquad i = 1,2$$
$$I_x^D(t) = 2\eta[E_1(t)E_2(t)] \otimes h_D(t) = \eta \operatorname{Re}\{\overline{A}_1(t)\overline{A}_2^*(t)\exp(j2\pi(\Delta v)t)\}$$
$$(4.19)$$

where the high frequency terms are removed due to the lower-pass filter of the detector impulse response and $\Delta v = v_1 - v_2$ is the frequency difference between the two laser sources.

According to the Wiener-Kintchine theorem [46], the power spectrum of the photodetector current, which can be measured with an electrical spectrum analyzer (ESA), is the Fourier transform (FT) of its autocorrelation. The autocorrelation of the photodetector current (Equation 4.18) is

$$\Gamma(\tau) = < I^D(t+\tau)I^D(t) >$$

$$= \Gamma_1(\tau) + \Gamma_2(\tau) + \Gamma_x(\tau) + < I_1^D(t+\tau)I_2^D(t) > + < I_2^D(t+\tau)I_1^D(t) >$$

$$+ < I_1^D(t+\tau)I_x^D(t) > + < I_2^D(t+\tau)I_x^D(t) > \quad (4.20)$$

$$+ < I_x^D(t+\tau)I_1(t) > + < I_x^D(t+\tau)I_2^D(t) >$$

where the first three terms are the autocorrelations of the direct terms and cross-term:

$$\Gamma_i(\tau) = < I_i^D(t+\tau)I_i^D(t) >, \quad i = 1, 2, x. \quad (4.21)$$

Since E_1 and E_2 are independent (statistically uncorrelated), i.e. the mean of a product of functions of random independent processes may be expressed as the product of the means, and $<E_i>$ (i = 1, 2) equal to zero, the last four terms of equation 4.20 can be removed. Due to stationary statistical result, evaluating a mean at $t + \tau$ has the same result as evaluating it at t, the middle two terms turns out to be equal. So Equation 4.20 can be rewritten as:

$$\Gamma(\tau) = \Gamma_1(\tau) + \Gamma_2(\tau) + \Gamma_x(\tau) + 2 < I_1^D(t) >< I_2^D(t) >. \quad (4.22)$$

Taking a Fourier transform of Equation 4.22 and using the convolution theorem, we obtain the expression of the power spectrum of the photocurrent below [41]:

$$S(f) = FT\{\Gamma(\tau)\} = S_1(f) + S_2(f) + S_x(f) + 2 < I_1^D >< I_2^D > \delta(f), \text{ and} \quad (4.23)$$

$$S_i(f) = FT\{\Gamma_i(\tau)\} = FT(< I_i^D(t+\tau)I_i^D(t) >), \qquad i = 1,2$$
$$S_x(f) = FT\{\Gamma_x(\tau)\} = 4S_{E_1}^{\varpi}(f) \otimes S_{E_2}^{\varpi}(f)$$

$$(4.24)$$

where $S_1(f)$ and $S_2(f)$ are the ordinary direct optical spectrum detection and $S_x(f)$ is the useful heterodyne mixing product which is the convolution of two laser source spectrum. The convolution originates from the multiplication of time-varying local oscillator field with the signal field in the photodetector. Multiplication in the time domain is equivalent to convolution in the frequency domain. Equation 4.23 is the main result for the power spectrum of the photocurrent due to uncorrelated stationary optical field mixing on the photodetector.

4.4.2   Optical Heterodyne Method

A typical setup for optical heterodyne linewidth measurement of fibre ring laser is illustrated in Figure 4.11. In this setup, the tunable laser serves as the local oscillator (LO) to provide a stable, narrow linewidth optical source. Initially, its wavelength must be tuned close to the tested fibre ring laser wavelength, which is due to the finite detection bandwidth decided by the photodetector and the finite analysis bandwidth offered by the ESA. A coarse wavelength tuning of the LO is performed using an OSA and usually the LO wavelength is tuned higher than the FRL wavelength under test. Then its optical frequency is fixed during the measurement. Light from the local oscillator (LO) is combined with the tested FRL signal using a 3-dB coupler and the polarization state of the LO light is aligned to the same polarization state of the

tested FRL signal using the polarization state controller placed in the LO path. The photodetector converts the interference beat tone of the combined lights to the electrical signal, which is detected and displayed in the ESA.
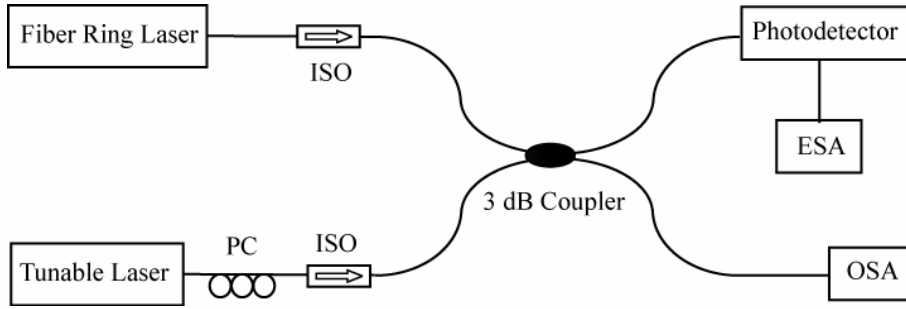
Fig. 4.11 Optical heterodyne setup for measuring laser linewidth.

According to the Equation 4.23, the displayed beat frequency (mixing term) ESA spectrum is given by:

$$S(f) \propto S_{\bar{E}_{LO}}(f) \otimes S_{\bar{E}_S}(f) \tag{4.25}$$

Therefore the lineshape of the laser, including any asymmetries, is replicated at a low frequency set by the optical frequency difference between the two lasers. If the LO laser linewidth is much smaller compared to the FRL under test, the lineshape spectrum of the local oscillator, $S_{\bar{E}_{LO}}(f)$ is approximated with a Dirac - Δ function: $P_{LO}\delta(f - f_{LO})$. Thus from Equation 4.25 the ESA will display:

$$S(f) \propto P_{LO} S_{\bar{E}_S}(f - f_{LO}) \tag{4.26}$$

Thus the ESA gives a measure proportional to the actual laser power spectrum $S_{\tilde{E}_S^{\varpi}}(\upsilon - \upsilon_{LO})$ translated to low frequencies which is easily measured using ESA. The key to the exceptional sensitivity of the heterodyne method is evident in Equation 4.26 where the detected spectrum amplitude increases with local oscillator power, P_{LO}. Larger local oscillator power translates to better sensitivity. Therefore the optical heterodyne method can characterize nonsymmetrical spectral lineshape and offer exceptional sensitivity and resolution, due to the narrow linewidth and large optical power of the LO.

4.4.3   Delayed Self-heterodyne Method

In the absence of a stable, narrow linewidth tunable local oscillator laser, the delayed self-heterodyne technique provides a simple way to perform linewidth measurement, as shown in Figure 4.12. The output beam of the fibre ring laser source is split into two paths by the coupler. One beam passes though the long length of fibre acting as the time delay and another beam passes though the frequency shifter. Then the two beams combine together using 3-dB coupler. If the delay time τ_0 of one path exceeds the coherence time τ_C of the source, the two combining beams interfere as if they originated from two independent laser offset in frequency by $\delta\upsilon$. The beat tone produced is displaced from 0 Hz by the shifted frequency $\delta\upsilon$ and displayed in the electrical spectrum analyzer.
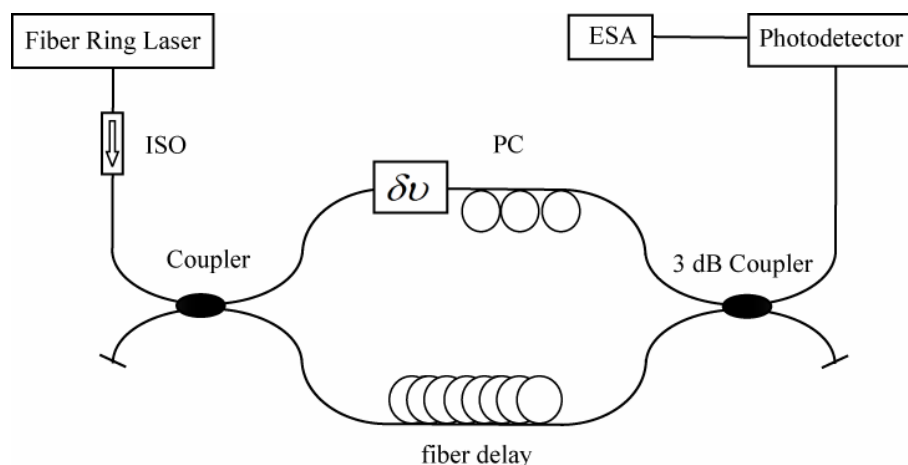
Fig. 4.12   Configuration of the delayed self-heterodyne method

In the delayed self-heterodyne technique, the frequency shifter is required for shifting the beat frequency away from the zero frequency.   Shifting the beat frequency from DC is useful to avoid instrumental limitations such as the DC response and more importantly to minimize the 1/*f* noise.   It is important that the shifted frequency in the frequency shifter must be larger than the optical spectral bandwidth of the laser under study, otherwise fold over effects near zero frequency will distort the observed spectrum.   Frequency shift can be attained by using either acousto-optic frequency shifters, phase modulators, or intensity modulators.   Since the shifted frequency does not depend on the laser source, the delayed self-heterodyne methods are less sensitive to slow wavelength drift.

The requirement for incoherent mixing sets a minimum delay requirement of the interferometer with respect to the laser's linewidth, $\tau_0 \geq \dfrac{1}{\Delta \upsilon}$.   When this condition is satisfied, the mixing becomes independent of the phases of the interfering light, leading to a more stable measurement.   For a linewidth of 1 MHz, the minimum

required differential time delay will be about 100 ns. This corresponds to approximately 200 m of single mode optical fibre. Note that given the large optical delays afforded by low-loss single mode optical fibre, linewidth measurements below 1 kHz are possible.

According to the Equation 4.23, the delayed self-heterodyne shifted frequency (mixing term) ESA spectrum is given by:

$$S(f) \propto S_{E_S}^{\varpi}(f - \delta\upsilon) \otimes S_{E_S}^{\varpi}(f)\}$$ (4.27)

Since the mixing term is essentially the test laser spectrum convolved with itself and displaced in the frequency by $\delta\upsilon$, the displayed lineshape will always be symmetrical even if the original lineshape is asymmetrical. In the case of a Lorentzian-shaped spectrum, the displayed ESA spectrum retains the Lorentzian shape and the FWHM linewidth will be twice of the actual FWHM linewidth.

4.4.4   Frequency Jitter

In both the heterodyne method and delayed self-heterodyne method, laser sources exhibiting frequency jitter or 1/f noise will yield larger measured linewidth [43]. The effects of frequency jitter on the linewidth measurement can be reduced by measuring further down on the displayed lineshape and transforming the measured

result into the correct FWHM linewidth. The advantages of the measuring further down on the lineshape can be understood by considering the effect of frequency jitter on the power spectrum [47]. The Lorentzian-optical power spectrum centered at f_0 with the frequency jitter can be written by:

$$S_E(f,t) \propto \cfrac{1}{1+\left[\cfrac{f - f_0 + \delta f(t)}{\Delta f / 2}\right]^2} \qquad (4.28)$$

where Δf is the FWHM linewidth and f is the optical frequency. When $f - f_0$ is larger than δf, the magnitude of the optical power spectrum depends more on the value of $f - f_0$ and less on the effect of δf. Thus the error due to frequency jitter decreases as the measurement is made further down the lineshape, such as 10 dB or 20 dB down. The correspondence between the measured bandwidth of the specific power and the FWHM linewidth of the Lorentzian-shaped spectrum is shown in Table 4.1. This technique assumes that the noise contribution at the 20-dB or 30-dB level is insignificant.

Table 4.1 Optical mixing technique linewidth relations

Measured Full-Width Point	Displayed width measured by delayed self-heterodyne method	Displayed width measured by heterodyne method
- 3 dB	$2\delta\upsilon$	$\delta\upsilon$
- 10 dB	$2\sqrt{9}\delta\upsilon$	$\sqrt{9}\delta\upsilon$
- 20 dB	$2\sqrt{99}\delta\upsilon$	$\sqrt{99}\delta\upsilon$
- 30 dB	$2\sqrt{999}\delta\upsilon$	$\sqrt{999}\delta\upsilon$

4.5   Chapter Summary

In this chapter, the background of the fibre ring laser is reviewed.   Different fibre ring lasers are introduced and explained.   It is then followed with the theoretical modeling of the fibre ring laser, which is very useful to understand the mechanism of the fibre ring laser.   The spectral behavior of the fibre ring laser can be simulated from the emission and absorption cross sections of the active fibre.

Furthermore, due to the narrow linewidth of the fibre ring laser, the theory and principle of optical mixing measurement is introduced.   The different configurations are explained including the heterodyne method and self delayed self-heterodyne method.

References

1. J. X. Cai, D. G. Foursa, C. R. Davidson, Y. Cai, G. Domagala, H. Li, L. Liu, W. W. Patterson, A. N. Pilipetskii, M. Nissov, and N. S. Bergano, "A DWDM demonstration of 3.73 Tb/s over 11 000 km using 373 RZ-DPSK channels at 10 Gb/s", *OFC 2003*, Atlanta, Georgia, post-deadline paper PD22, Mar. 2003.

2. D. Anthon, J. D. Berger, and A. Ashmead, "Tunable external cavity semiconductor lasers for network application", *ECOC 2002, 28th European Conference on Optical Communication*, Sep. 2002.

3. J. L. Zyskind, J. W. Sulhoff, J. Stone, D. J. Digiovanni, L. W. Stultz, H. M. Presby,A. Piccirilli, and P. E. Pramayon, "Electrically tunable, diodepumped erbium-doped fiber ring laser with fiber Fabry–Perot etalon", *Electron. Lett.*, vol. 27, no. 21, pp. 1950–1951, 1991.

4. S. Yamashita, and M. Nishinara, "Widely Tunable Erbium-Doped Fiber Ring Laser Covering Both C-band and L-band," *IEEE Photon. Technol. Lett.*, vol. 7, no. 20, pp. 41-43, Jan. 2001.

5. A. Bellemare, M. Karásek, C. Riviere, F. Babin, G. He, V. Roy, and G. W. Schinn, "A broadly tunable erbium-doped fiber ring laser: experimentation and modeling," *IEEE J. Select. Topics Quantum Electron.*, vol. 7, no. 1, pp. 22-29, Jan. 2001.

6. X. Dong., P. Shum, N. Q. Ngo, C. C. Chan, B. O. Guan, and H. Y. Tam, "Effect of active fiber length on the tunablility of erbium-doped fiber ring lasers," *Opt.*

Express, vol. 11, no. 26, pp. 3622-3627, Dec. 2003.

7. T. Haber, K. Hsu, C. Miller, and Y. Bao, "Tunable Erbium-Doped Fiber Ring Laser Precisely Locked to the 50-GHz ITU Frequency Grid", *IEEE Photon. Technol. Lett.*, vol. 12, no. 11, pp. 1456-1458, Nov. 2000.

8. C. H. Yeh, C. C. Lee, C. Y. Chen, and S. Chi, "A Stabilized and Tunable Erbium-Doped Fiber Ring Laser with Double Optical Filter", *IEEE Photon. Technol. Lett.*, vol. 16, no. 3, pp. 765-767, Mar. 2004.

9. Y. W. Lee, and B. Lee, "Wavelength-Swithable Erbium-Doped Fiber Ring Laser Using Spectral Polarization-Dependent Loss Element", *IEEE Photon. Technol. Lett.*, vol. 15, no. 6, pp. 795-797, Jun. 2003.

10. M. Delgado-Pinar, J. Mora, A. Diez, J. L. Cruz, and M. V. Andres, "Wavelength-Switchable Fiber Laser Using Acoustic Waves", *IEEE Photon. Technol. Lett.*, vol. 17, no. 3, pp. 552-554, Mar. 2005.

11. W. F. Liu, P. St. J. Russell, and L. Dong "100% efficient narrow-band acousto-optic tunable reflector using a fiber Bragg grating," *J. Lightwave Technol.*, vol. 16, no. 11, pp. 2006–2009, Nov. 1998.

12. L. Su, C. Lu, J. Z. Hao, Z. H. Li, and Y. X. Wang, "Design of wavelength-switching erbium-doped fiber lasers with a multimode fiber Bragg grating using spatial-mode excitation and selection techniques", *IEEE Photon. Technol. Lett.*, vol. 17, no. 2, pp. 315-317, Feb. 2005.

13. J. L. Zhang, C. Y. Yue, G. W. Schinn, W. R. L. Clements, and J. W. L. Lit, "Stable Single-Mode Compound-Ring Erbium-Doped Fiber Laser", *J.*

Lightwave Technol., vol. 14, no. 1, pp. 104 – 109, Jan. 1996.

14.   H. X. Chen, F. Babin, M. Leblanc, and G. W. Schinn, "Widely Tunable Singel-Frequency Erbium-Doped Fiber lasers", *IEEE Photon. Technol. Lett.*, vol. 15, no. 2, pp. 185-187, Feb. 2003.

15.   Y. Cheng, J. T. Kringlebotn, W. H. Loh, R. I. Laming, and D. N. Payne, "Stable single-frequency traveling-wave fiber loop laser with integral saturable-absorber-based tracking narrow-band filter", *Opt. Lett.*, vol. 20, no. 8, pp. 875-877, Apr. 1995.

16.   Y. W. Song, S. A. Havstad, D. Starodubov, Y. Xie, A. E. Willner, and J. Feinberg, "40-nm-wide Tunable Fiber Ring Laser With Single-Mode Operation Using a Highly Stretchable FBG", *IEEE Photon. Technol. Lett.*, vol. 13, no. 11, pp. 1167-1169, Nov. 2001.

17.   N. J. C. Libatique, L. Wang, and R. K. Jain, "Single-longitudinal-mode tunable WDM-channel-selectable fiber laser", *Opt. Exp.*, vol. 10, no. 25, pp. 1503-1507, Dec. 2002.

18.   J. Liu, J. P Yao, J. Yao, and T. H. Yeap, "Single-longitudinal-mode Multiwavelength Fiber Ring Laser", *IEEE Photon. Technol. Lett.*, vol. 16, no. 4, pp. 1020-1022, Apr. 2004.

19.   N. Kishi, and T. Yazaki, "Frequency Control of a Single-Frequency Fiber Laser by Cooperatively Induced Spatial-Hole Burning", *IEEE Photon. Technol. Lett.*, vol. 11, no. 2, pp. 182-184, Feb. 1999.

20.   L. Xu, I. Glesk, D. Rand, V. Baby, and P. R. Prucnal, "Suppession of beating

noise of narrow-linewidth erbium-doped fiber ring lasers by use of a semiconductor optical amplifier", *Opt. Lett.*, vol. 28, no. 10, pp. 780-782, May 2003.

21. K. Sao, and H. Toba, "Reduction of mode partition noise by using semiconductor optical amplifiers", *IEEE J. Sel. Top. Quantum Electron.*, vol. 7, no. 2, pp. 328-333, Mar. 2001.

22. D. N. Wang, F. W. Tong, X. H. Fang, W. Jin, P. K. A. Wai and J. M. Gong, "Multiwavelength erbium-doped fiber ring laser source with a hybrid gain medium," *Opt. Comm.*, vol. 228, Iss. 4-6, pp. 295-301, Dec. 2003.

23. Y. Sun, J. W. Sulhoff, A. K. Srivasta, J. L. Zyskind, T. A. Strasser, J. R. Pedrazzani, C. Wolf, J. Zhou, J. B. Judkins, R. P. Espindola, and A. M. Vengsarkar, "80 nm ultra-wideband erbium-doped silica fiber amplifier," *Electron. Lett.*, vol. 33, no. 23, pp. 1965–1967, 1997.

24. C.R. Giles, and E. Desurvire, "Modeling erbium-doped fiber amplifiers", *J. Lightwave Technol.*, vol. 9, no. 2, pp. 271-283, Feb. 1991.

25. G. N. Van den Hoven, E. Snoeks, A. Polman, C. Van Dam, J. W. Van Uffelen and M. K. Smit, "Upconversion in Er-implanted Al2O3 waveguides," *J. Appl. Phys.*, vol. 79, no. 3, pp. 1258-1266, Feb. 1996.

26. P. C. Becker, N.A. Olsson, J.R. Simpson, Erbium-Doped Fiber Amplifiers. Fundamentals and Technology, Academic Press 1999, Chapter 6.

27. P. Blixt, J. Nilsson, T. Carlnas, and B. Jaskorzynska, "Concentration-dependent upconversion in Er3+-doped fiber amplifiers: experiments and modeling," *IEEE*

Photon. Technol. Lett., vol. 3, no. 11, pp.996-998, 1991.

28. H. masuda, A. Takada, and K. Aida, "Modeling the gain degradation of high concentration erbium-doped fiber amplifiers by introducing inhomogeneous cooperative up-conversion," *J. Lightwave Technol.*, vol. 10, no. 12, pp. 1789-1799, 1992.

29. C. C. Ye, P. R. Morkel, E. R. Taylor, and D. N. Payne, "Direct observation of cooperative upconversion mechanisms in Erbium-doped fiber amplifiers," *ECOC 1993, 19th European Conference on Optical Communication*, Sep. 1993.

30. E. Delevaque, T. Georges, M. Monerie, P. Lamouler, and J.-F. Bayon, "Modeling of pair-induced quenching in erbium-doped silicate fibers", *IEEE Photon. Technol. Lett.*, vol. 5, no. 1, pp. 73-75, Jan. 1993.

31. T. Georges, E. Delevaque, M. Monerie, P. Lamouler, and J. F. Bayon, "Pair induced quenching in erbium-doped silicate fibers," *Proc. 3rd Top. Meet. Opt. Amplifiers*, Santa Fe, CA, paper WE4., 1992.

32. J. Nilsson, B. Jaskorzynska, and P. Blixt, "Performance reduction and design modification of erbium-doped fiber amplifiers resulting form pair-induced quenching," *IEEE Photon. Technol. Lett.*, vol. 5, no. 12, pp. 1427-1429, Dec. 1993.

33. B. N. Samson, W. H. Loh, and J. P. De Sandro, "Experimental evidence of differences in the absorption spectra of clustered an isolated ions in erbium-doped fibers," *Opt. Lett.*, Vol. 22, no. 23, pp.1763-1765, 1997.

34. E. Desurvire, Erbium-Doped Fiber Amplifiers: Principles and Applications, John

Wiley & Sons, N.Y., 1994.

35.   C. G. Atkins, J. R. Armitage, R. Wyatt, B. J. Ainslie, and S. P. Craig-Ryan, "Pump excited state absorption in Er3+ doped optical fibres", *Opt. Comm.*, vol. 73, iss. 3, pp. 217-222, Oct. 1989.

36.   R. S. Quimby, W. J. Miniscalco, and B. A. Thompson, "Upconversion and 980-nm excited state absorption in erbium doped glass", *Proc. SPIE*, 1993.

37.   W. H. Press, B. P. Flannery, S. A. Teukolsky, W. T. Vetterling, Numerical Recipes: The Art and Science of Scientific Computing, Cambridge University Press, New York, 1986.

38.   T. Pfeiffer, H. Schmuck, and H. Bulow, "Output power characteristics of erbium-doped fiber ring laser," *IEEE Photon. Technol. Lett.*, vol. 4, no. 8, pp. 847-849, Aug. 1992.

39.   S. Selvakennedy, M. A. Mahdi, M. K. Abdullah, P. Poopalan, and H. Ahmad, "Design optimisation of erbium-doped fibre ring laser through numerical simulation", *Optics Comm.*, vol. 170, iss. 4-6, pp. 247–253, Nov. 1999.

40.   S. Kawanishi, A. Takada and M. Saruwatari, "Wide-band frequency-response measurement of optical receivers using optical heterodyne detection," *J. of Lightwave Technol.*, vol. 7, no. 1, pp. 92-98, Jan. 1989.

41.   M. Nazarathy, W. V. Sorin, D. M. Baney and S. A. Newton, "Spectral analysis of optical mixing measurements," *J. of Lightwave Technol.*, vol. 7, no. 7, pp. 1083-1096, Jul. 1989.

42.   K. Iwatsuki, S. kawai, S. Nishi and M. Saruatari, "Timing jitter due to carrier

linewidth of laser-diode pulse sources in ulra-high speed soliton transmission," *J. of Lightwave Technol.*, vol. 13, no. 4, pp. 639-648, Apr. 1989.

43. L. E. Richter, H. I. Mandelbery, M. S. Kruger and P. A. Mcgrath, "Linewidth determination from self-heterodyne measurements with subcoherence delay times," *J. of Quan. Electron.*, vol. qe-22, no. 11, pp.2070-2074, Nov. 1986.

44. J. W. Dawson, N. Park and K. J. Vahala, "An improved delayed self-heterodyne interferometer for linewidth measurements," *IEEE Photon. Technol.*, Vol.4, no. 9, pp.1063-1065, Sep. 1992.

45. H. Joseph and D. Sadot, "A novel self-heterodyne method for combined temporal and spectral high-resolution measurement of wavelength transients in tunable lasers," *IEEE Photon. Tehcnol. Lett.*, vol. 16, no. 8, pp. 1921-1923, Aug. 2004.

46. Joseph W. Goodman, Statistical Optics, New York: Wiley, 1965.

47. D. Derickson, Fiber Optic Test and Measurement, New York: Prentice Hall PTR, 1998.

Chapter **5**

Fibre Ring Laser with Wide Tuning Range

5.1 Introduction

In Section 4.2, several wavelength-tunable fibre ring laser configurations were introduced. These include the technology of pumping the erbium-doped fibre (EDF) to deep saturation regime [1], and the use of optical switch to alter the length of EDF in a fibre ring laser cavity [2]. Most fibre ring lasers employ silica-based erbium-doped fibres (Si-EDFs) as gain medium, however, pair-induced quenching and clustering effects [3] limit the concentration of erbium ions that can be doped into silicate fibre and therefore long length of Si-EDF is normally needed in the construction of fibre ring lasers. The long cavity length makes them more susceptible to environmental influence. Furthermore, fibre ring lasers based on Si-EDF is difficult to tune to wavelength beyond 1610 nm.

In this chapter, a new type of active fibre based on bismuth oxide glass will be introduced and its application in fibre ring laser will be described. The characteristics of erbium-doped bismuth oxide based fibre, Bi-EDF, will be outlined.

The design of a fibre ring laser using a short length of Bi-EDF, achieving an extremely large tuning range over 100 nm using tunable MEMS filter or scanning fibre Fabry-Perot filter will be described. Finally, a single-longitudinal mode fibre ring laser realized by using an unpumped EDF saturable absorber will be described. The laser linewidth of single-longitudinal mode fibre ring laser was measured to be about 1.17 kHz by the delayed self-heterodyne technique.

5.2 Bismuth Oxide Based Erbium-doped Fibre

Recently developed Bi-EDF by Asahi Glass Corp. of Japan, offers many advantages. The main advantage of Bi-EDF over Si-EDF is its high solubility to erbium ions, permitting high erbium ion concentration doping in bismuth oxide fibres and therefore leading to the realization of very short-length optical fibre amplifiers [4, 5]. Due to the pair-induced quenching and clustering effects of erbium ions, the doped concentration of erbium ions in silica-based fibre can not be very high (typical less than 1,000 wt-ppm). However, Bi-EDF can be highly doped with erbium ions up to 26,000 wt-ppm, which is more than one order of magnitude higher than that in Si-EDF, without suffering from the pair-induced quenching and clustering effects. The reason is that the bismuth oxide can extend the distance between erbium ions and reduce the concentration quenching significantly [6] due to its high solubility to erbium ions. Consequently, shorter fibre-length of Bi-EDF will be needed to attain similar amplification of the much longer silica-based erbium-doped fibres. In

addition, the normalized emission intensity of Bi-EDF is higher than that of Si-EDF, particularly in the L-band, as shown in Figure 5.1 [7]. This implies that Bi-EDF provides broader optical gain bandwidth than Si-EDF. Another advantage is that low nonlinearity optical amplifiers based on Bi-EDF can be constructed [8]. Although the intrinsic nonlinear refractive index n_2 of bismuth oxide based fibre is 12 times higher than that of the silica fibre [9], due to its very short fibre length the total nonlinearity of Bi-EDF is smaller than Si-EDF under similar gain condition.
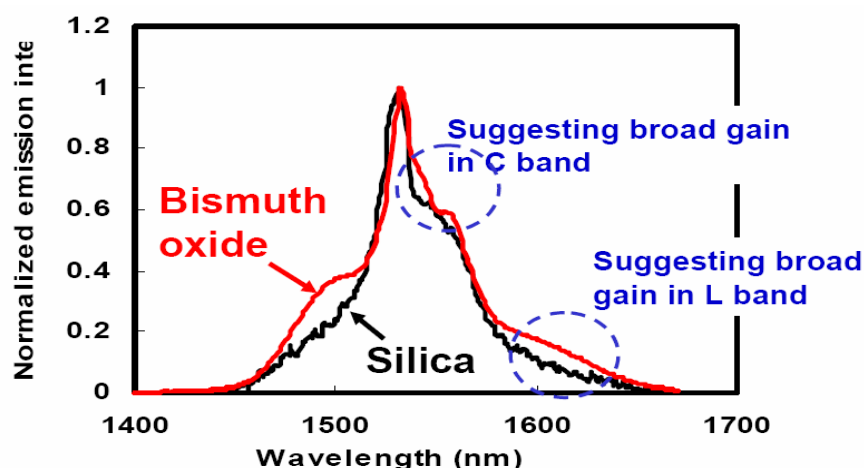

Fig. 5.1   Normalized emission intensity of the Bi-EDF and Si-EDF [7].

The major problem of Bi-EDF is fusion splicing to standard silica fibres. The melting point of Bi-EDF (~600 deg C) is much lower than that of Silica fibre (>1000 deg C) and therefore commercial fusion splicers can not be used to fusion splice Bi-EDF to standard telecommunication fibre. Furthermore, the refractive index of the core and cladding of Bi-EDF are ~2.03 and ~2.02 while the refractive index of the core and cladding of the silica single mode fibre (SMF) are ~1.45 and ~1.44.

Consequently, joining of Bi-EDF to standard singlemode fibre will introduce Fresnel reflection loss of ~2.8% (~0.12 dB). Angled splicing is thus needed to reduce reflection back to the fibres.
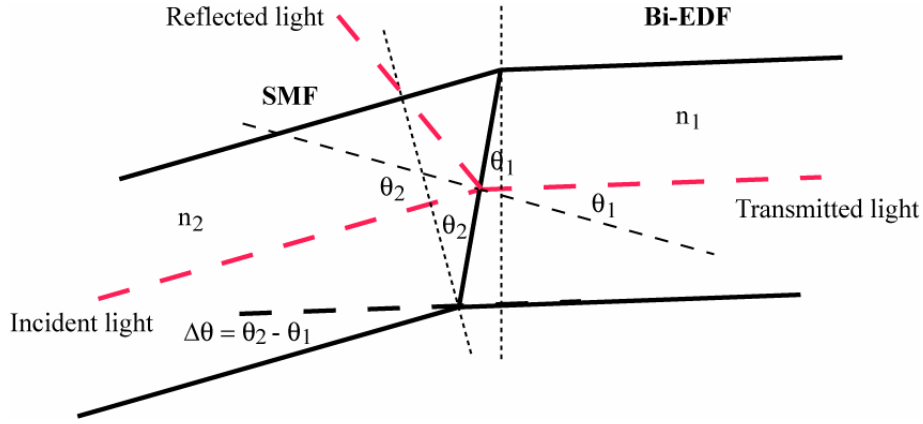

Fig. 5.2   Angled splicing configuration between Bi-EDF and SMF [7].

The configuration of angled splicing between Bi-EDF and SMF is shown in Figure 5.2.   We assume light propagates along the optical fibre axis.   To avoid reflected light back to the fibre, the incident angle, θ_2, must be greater than θ, given below [10].

$$\theta = 45^o - \frac{1}{2}\arcsin\left(\frac{n_{clad}}{n_{core}}\right)$$

(5.1)

From equation 5.1, we obtain the incident angle $\theta_2 \geq 3.36^o$ in SMF and the refractive angle $\theta_1 \geq 2.84^o$ in Bi-EDF.   However, the incident angle can not be too large as it would increasing splicing loss and induce large polarization-dependent loss (PDL) between the SMF and Bi-EDF.   For simplicity, we assume no extra coupling loss is introduced between the couplings of two fibres.   According to the Fresnel

Equations, the transmittance of light through a interface can be expressed as [10]:

$$T_\perp = 1 - \left(\frac{\sin(\theta_2 - \theta_1)}{\sin(\theta_2 + \theta_1)} \right)^2 , \text{ and} \tag{5.2}$$

$$T_{//} = 1 - \left(\frac{\tan(\theta_2 - \theta_1)}{\tan(\theta_2 + \theta_1)} \right)^2 , \tag{5.3}$$

where $T_\perp$ and $T_{//}$ are the transmittance of the light in parallel and perpendicular direction respectively. θ_2 and θ_1 are the incident angle in SMF and the refraction angle in Bi-EDF, respectively. θ_2 and θ_1 must satisfy the Snell's Law as follow.

$$n_2 \sin(\theta_2) = n_1 \sin(\theta_1), \tag{5.4}$$

where n_2 and n_1 are the refractive index of the core of silica fibre and bismuth fibre, respectively. From Equation 5.2 - 5.4, we obtained the relationship between the light transmittance and incident angle, as shown in Figure 5.3. The diamond line is the parallel component transmittance versus different incident angles and the triangle line is the perpendicular component transmittance.
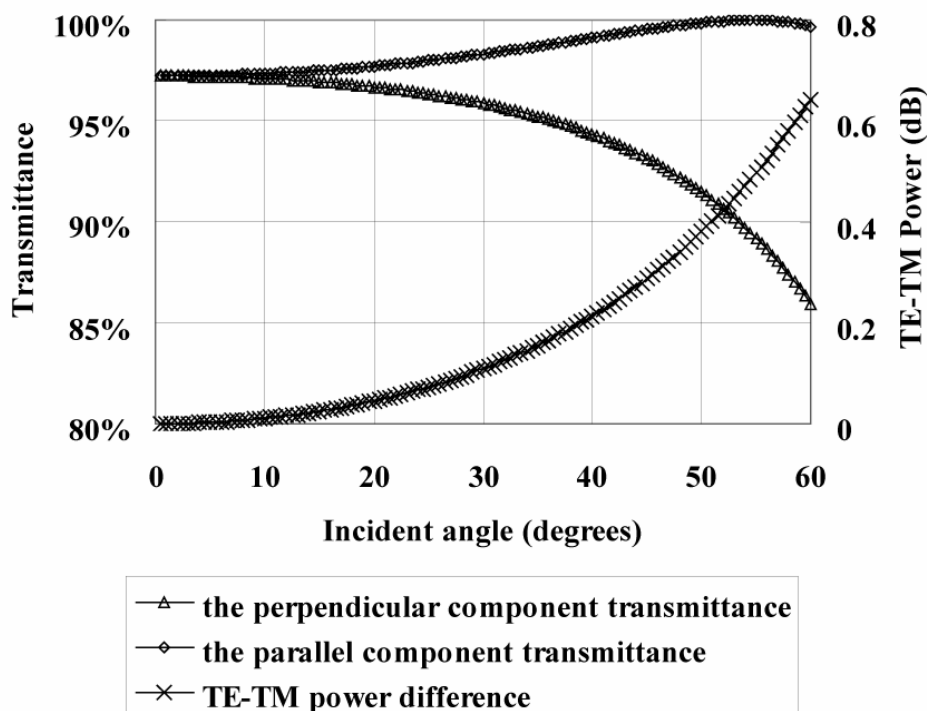
Fig. 5.3   Transmittance and TE-TM power difference versus incident angle.

It can be seen clearly from Figure 5.3 that when the incident angle is less than 50

degrees, the parallel component transmittance increases with the incident angle,

whereas the perpendicular component decreases with the incident angle.   Therefore

the TE-TM power difference (i.e. PDL) increases with the incident angle, which

should be small in practical application and is about 0.01 dB when the incident angle

is 10 degrees.   Therefore the incident angle should be less than 10 degrees, i.e.

$\theta_2 \leq 10^o$, to ensure that PDL is less than 0.01 dB.   That is $3.36^o \leq \theta_2 \leq 10^o$.   It was

found experimentally that $\theta_2 = 8.2^o$ and $\theta_1 = 6^o$ is the optimum, as shown in

Figure 5.4 [7].
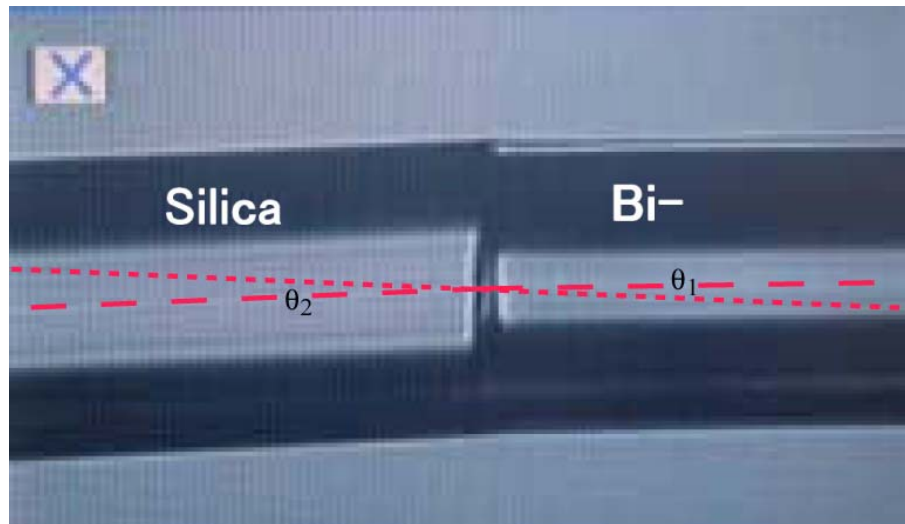
$\theta_1 = 6.0^0$, $\theta_2 = 8.2^0$ is the optimum

Fig. 5.4   Optimum fusion angles between Bi-EDF and SMF [7].

In the above analysis, mode mismatch between the fibres was not considered.   The diameter of the core of Bi-EDF and SMF are 4.0 µm and 9.0 µm, respectively, therefore it will introduce large coupling loss due to the large different in mode field diameter.   To reduce the coupling loss, the Bi-EDF was angle spliced to a short length of high numerical aperture fibre (Corning HI980), which was then spliced to SMF-28 fibre, providing better mode field diameter matching, as shown in Figure 5.5 [7].   By applying the aforementioned technique, splicing loss less than 0.2 dB for one angled splice and return loss (reflection loss) larger than 60 dB were achieved.
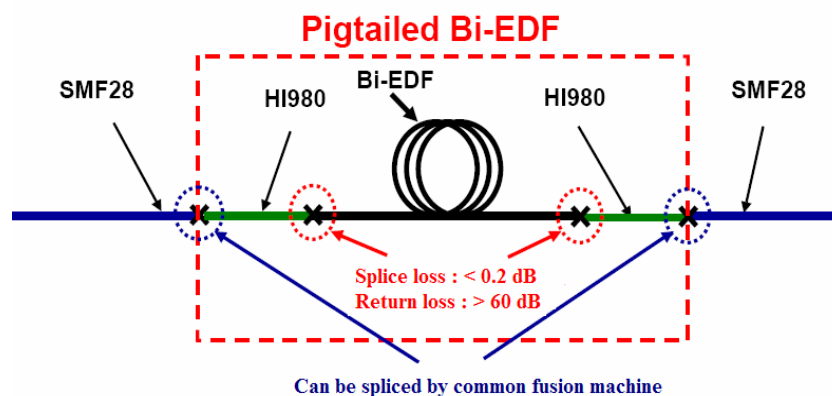
Fig. 5.5   Splicing detail of the pigtailed Bi-EDF [7].

5.3   Wide Wavelength Tuning Range FRL

The configuration of a traveling wave tunable fibre ring laser constructed with Lanthanum-codoped Bi-EDF is shown in Figure 5.6.   Lanthanum was doped in Bi-EDF to increase the solubility of erbium ions in bismuth glass.   The Bi-EDF was pumped by 1480 nm semiconductor laser diode via port 1 of a four-port optical circulator, which exhibits a fairly flat pass-band in the wavelength range of 1460 nm to 1630 nm.   Of course the pump laser diode can also enter cavity via the 1480 nm port of the wideband thin-film wavelength-division multiplexer (WDM) filter, which has flat pass-band in the signal port for wavelength ranges from 1520 nm to 1630 nm, as used in Figure 5.6 to monitor the unabsorbed pump power.   If the backward pump energy is not enough, the pump monitor can also used to add 1480 nm semiconductor laser diode to cavity as the forward pump source.   The length of the Bi-EDF was 84.6 cm long. The erbium concentration in the Bi-EDF is 6,470 wt-ppm and the Lanthanum concentration is 4.4 %wt.   The peak absorption of the Bi-EDF at 1480

nm and 1530 nm are 167 and 267 dB/m, respectively. The circulator (from port 3 to

port 2) and the optical isolator were used to reduce the reflection from the filter back

to the Bi-EDF as well as to ensure unidirectional operation of the ring laser.

Reflection from the input end of the filter was employed for the laser output and exit

from port 4 of the circulator. A 20 % fused fibre taper was included in the laser
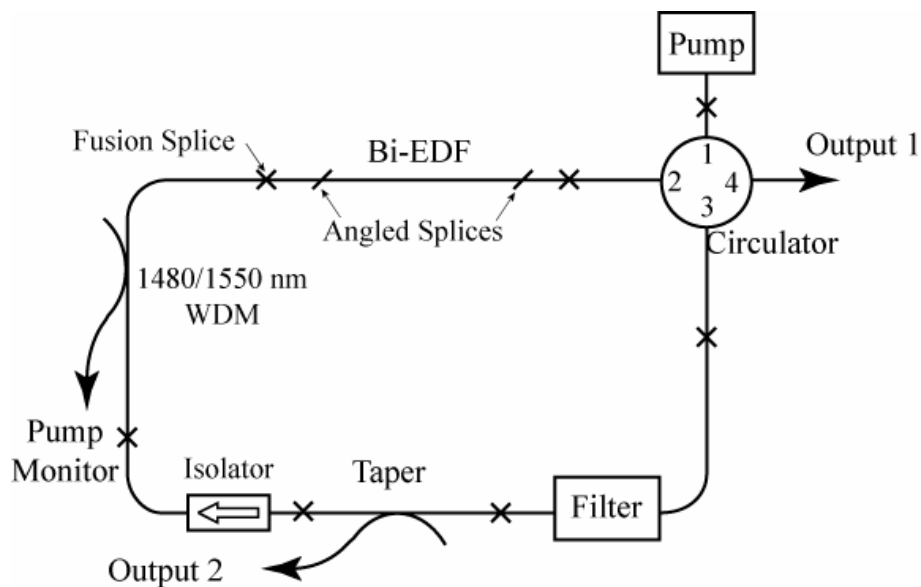
cavity to provide a second laser output.

Fig. 5.6 Configurations of the Bi-EDF tunable fibre ring laser.

5.3.1   Experimental Results with MEMS Filter

A narrowband, wide tunable range MEMS filter was employed to tune the laser

wavelength. By varying the input voltage from 10 V to 32 V, the MEMS filter can

be tuned over 120 nm, from 1630 nm to 1510 nm respectively. The MEMS filter

also exhibits very high scanning speed (greater than 100,000 nm/s). The 3-dB

optical bandwidth of the MEMS filter is about 20 pm (~2.5 GHz) and the typical

transmission and reflection spectra are shown in Figure 5.7, which the wavelength is

fixed at 1564.02 nm. The insertion loss of the MEMS filter at the peak of the

pass-band is less than 1.5 dB and the out-of-band reflection from both ends of the
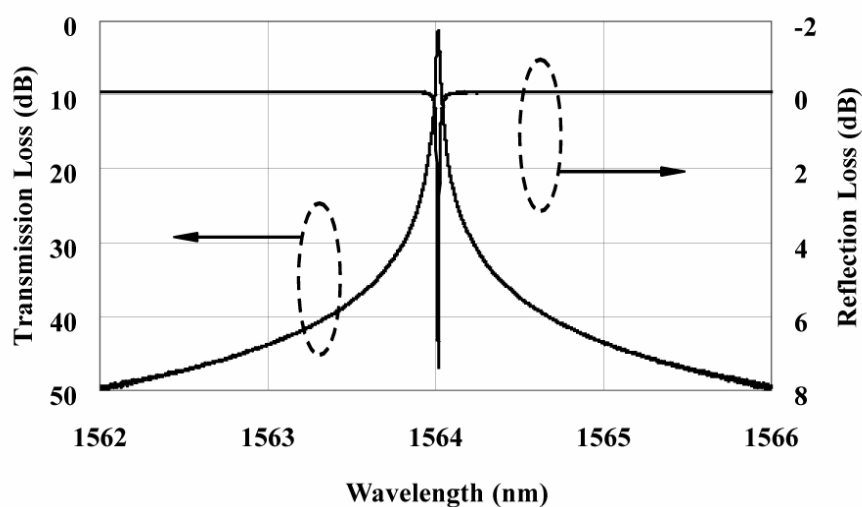
MEMS filter is very high (> 95 %).

Fig. 5.7 The typical transmission and reflection spectra of the MEMS filter.

Figure 5.8 (a) and (b) show the output spectra of the fibre ring laser obtained from

port 4 of the circulator and taper respectively, which is measured with an optical

spectrum analyzer (OSA) with 0.1 nm resolution. The fibre ring laser was pumped

with 120 mW of optical power. By varying the pass-band of the MEMS filter, the

laser wavelength was tuned from 1520 nm to 1626 nm, exhibiting a large tuning range

of 106 nm. From the output 1 fibre ring laser, over the *C*-band region (from 1530

nm to 1570 nm), the extinction ratio is over 45 dB and the output power is greater

than +7 dBm. Outside the *C*-band, both the output power and the extinction ratio

reduce.   The ASE in both outputs increase when the lasing wavelength is tuned away from the wavelength range where the Bi-EDFA provides higher optical gain.   It is more pronounced for output 1 because of the extremely high out-of-band reflection of the MEMS filter which reflects virtually all the ASE to output 1 whereas in output 2, the ASE is filtered by the MEMS filter.   Note that the 106 nm tuning range was achieved without the 20% taper inside the laser cavity.   With the inclusion of the 20% taper, the cavity loss was slightly increased and both the output power and wavelength tuning range from output 1 were reduced slightly to 104 nm.
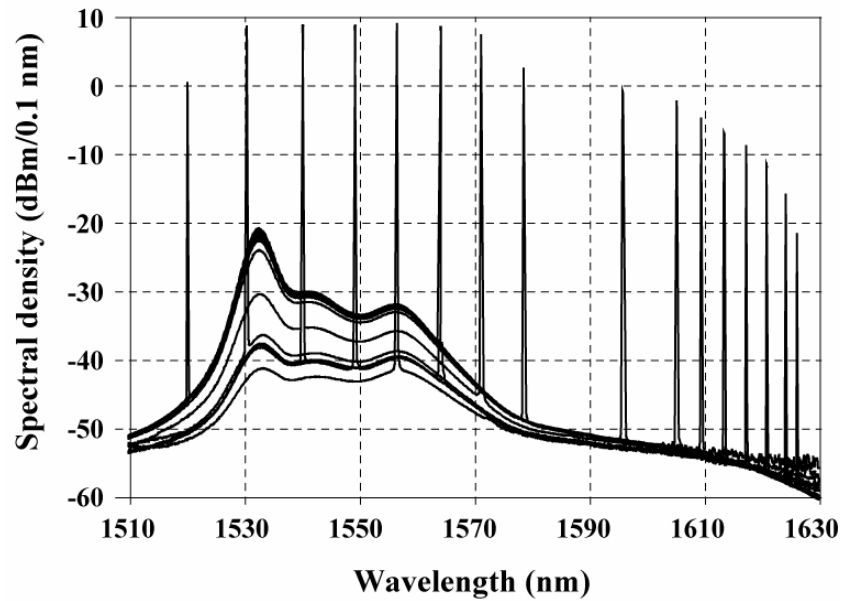
(a)
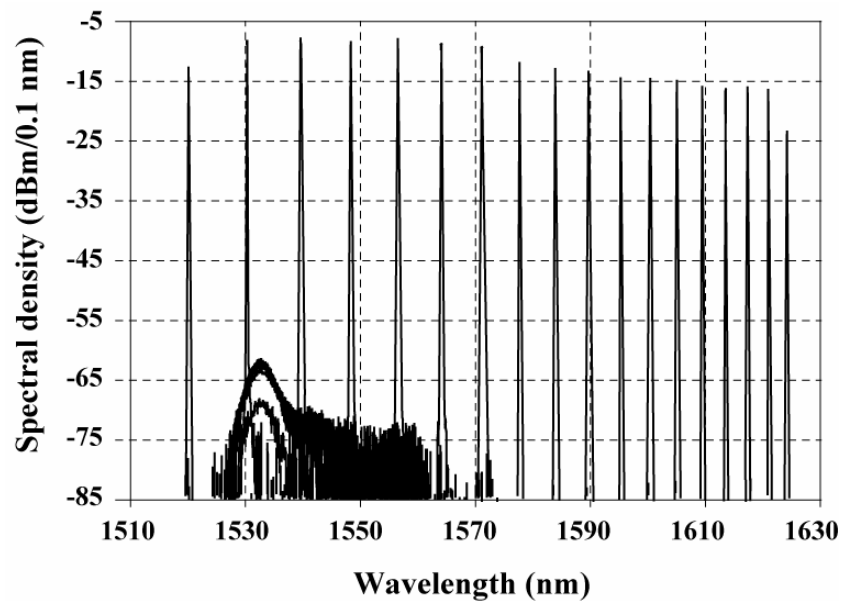
(b)

Fig. 5.8   Laser output spectra measured with an OSA with 0.1 nm resolution.   (a) From port 4 of the circulator of the tunable fibre ring laser.   (b) From the 20 % taper of the tunable fibre ring laser.

The laser output from the taper exhibits very high extinction ratio of better than 60 dB throughout the entire 104 nm wavelength tuning of the fibre ring laser.   The improvement in the extinction ratio is because the laser output was taken from the

output of the MEMS filter which filters the out-of-band ASE. Whereas in the former case, the output was taken from the reflection at the input of the MEMS filter which reflects both the lasing wavelength as well as the out-out-band ASE. The low optical output power from the taper is induced by the nonlinear behaviour of the MEMS filter. The taper output power will not increase greatly but the linewidth of spectrum becomes wider when the pump power is increased. This is a fully reversible process (reversed by the reduction of power) and according to the manufacturer this nonlinear behaviour is related to the temperature increase in the cavity. Figure 5.9 shows the different output spectra of the laser at the different pump powers. The diamond dots, the triangle dots and the cross dots lines were measured by OSA with 0.01 nm resolution at pump power of 80 mW, 110 mW and 140 mW, respectively from the taper port.
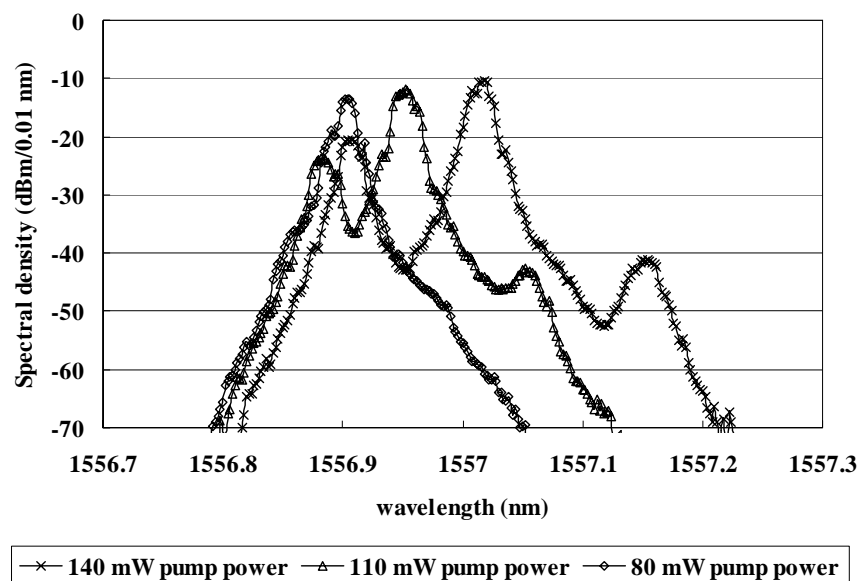
Fig. 5.9 Output spectra of the fibre ring laser tuned at different pump power.

5.3.2 Experimental Results Using Scanning Fibre F-P Filter

Due to the low output power of the taper port using the MEMS filter, a scanning fibre F-P filter (manufactured by Micron Optics) was employed to tune the laser wavelength. The optical bandwidth of the scanning fibre F-P filter is about 0.09 nm (~ 11.68 GHz) and the FSR is 61 nm (~ 7630 GHz). The finesse of this fibre F-P filter (~ 700) is lower than that of the MEMS filter (~ 10,000) and thus can handle large input power before the onset of the filter's nonlinear behaviour. The insertion loss of the scanning fibre F-P filter at the peak of the pass-band is about 1.8 dB. Since the FSR is 61 nm, a C-/L-band WDM filter is added in the cavity to attain single wavelength lasing. The output wavelength is in the C-band when the scanning fibre F-P filter is connected to the C-band port of the C-/L-band WDM filter, which exhibits an insertion loss of 0.14 dB in the wavelength range from 1500 nm to 1562 nm. The output wavelength is in the L-band when the scanning fibre F-P filter is connected to the L-band port of the C-/L-band WDM filter, which exhibits an insertion loss of 0.27 dB in the wavelength range form 1570 nm to 1640 nm, as shown in Figure 5.10.
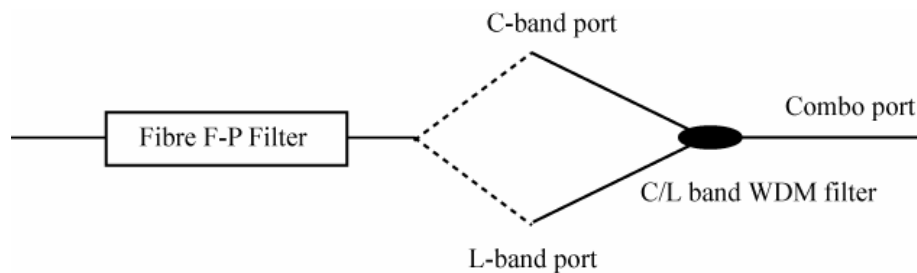

Fig. 5.10   Combined filter for C+L tunable range.

Figure 5.11 show the total C- and L-band output spectra of the fibre ring laser obtained from the taper port, which is measured with an optical spectrum analyzer (OSA) with 0.1 nm resolution. The fibre ring laser was pumped with 82 mW of optical power. By varying the pass-band of the F-P filter, the minimal lasing wavelength in C-band is 1517 nm and the maximum lasing wavelength in L-band is 1621 nm, exhibiting a large tuning range of 104 nm. The laser output exhibits very high extinction ratio of better than 60 dB throughout the entire 104 nm wavelength tuning of the fibre ring laser and the output power is greater than 0 dBm. A larger tunable range and higher output power can be obtained if the pumped power is increased. Since the reflection of the scanning fibre F-P filter is small, the output power from port 4 of the circulator is less than -20 dBm.
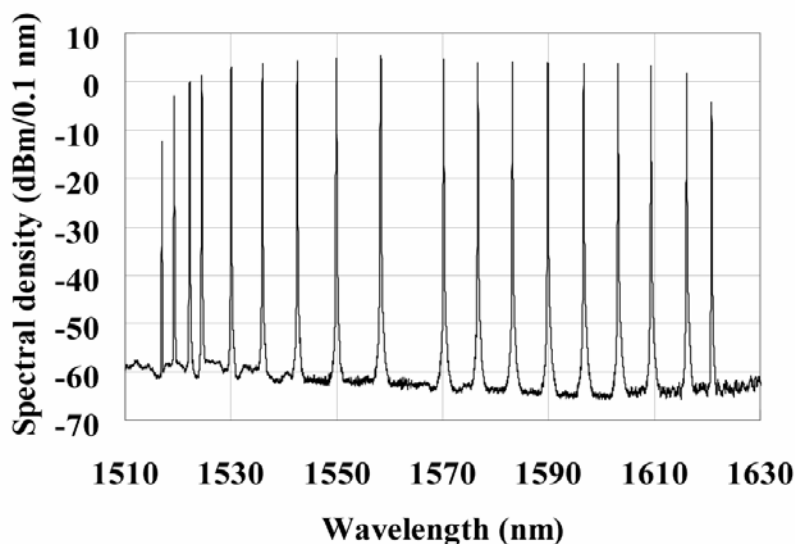

Fig. 5.11 Laser output spectra measured with an OSA with 0.1 nm resolution.

A typical lasing spectrum was measured by an OSA using 0.01 nm resolution and is

shown in Figure 5.12. The asymmetric shape of the laser is mainly caused by the

optical spectrum analyzer response. The centre wavelength is 1574.45 nm and the 3

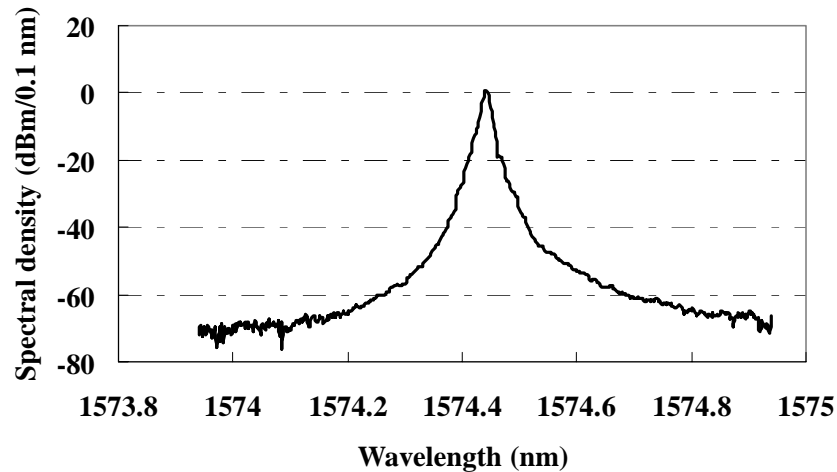dB bandwidth is about 0.02 nm, limited by the resolution of OSA.

Fig. 5.12   Typical output spectra measured with an OSA with 0.01 nm resolution.

5.3.3   Single Longitudinal Mode Operation and Linewidth Measurement

Due to the long ring cavity length, the output of the laser is multi-longitudinal mode.

Single longitudinal mode can be attained by modifying the laser configuration slightly,

as shown in Figure 5.13. Comparing to Figure 5.4, ports 3 and port 4 of the optical

circulator were reconfigured. A 2.5-m long un-pumped Si-EDF, whose peak

absorption at 1480 nm is about 3 dB/m, was spliced to port 3 of the circulator and the

other end of the Si-EDF was spliced to an FC/PC connector which was gold coated to

serve as a mirror. The purpose of this additional arm in the ring cavity is to produce

a periodic spatial hole burning by the light passing into and out of the Si-EDF, thereby

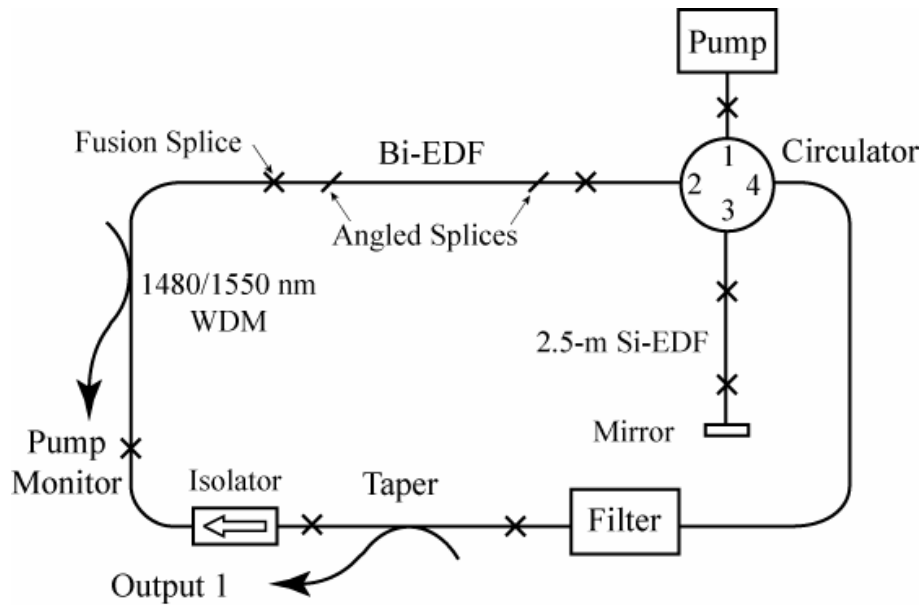generating an intra-cavity narrow-band filter [11].

Fig. 5.13 Single-longitudinal mode output fibre ring laser.

A typical RF spectrum of the fibre ring laser with and without un-pumped Si-EDF was measured with a 25 GHz Newfocus photodiode detector together with a RF electrical spectrum analyzer, as shown in Figure 5.14 (a) and (b) respectively.   In this case, ~ 10 MHz beat frequency component means ~ 15 m ring cavity length.   Figure 5.14 (a) has many frequency components, which is generated by the beating effect of the multi-longitudinal modes.   The minimum beat frequency component is decided by the longitudinal mode spacing, which depends on the ring cavity length.   The absence of the tones in Figure 5.14 (b) implies that all the side modes are suppressed, which means only one longitudinal mode operating in the ring cavity.   Due to the large insertion loss induced by the un-pumped EDF, both the output power and tunable range are reduced.
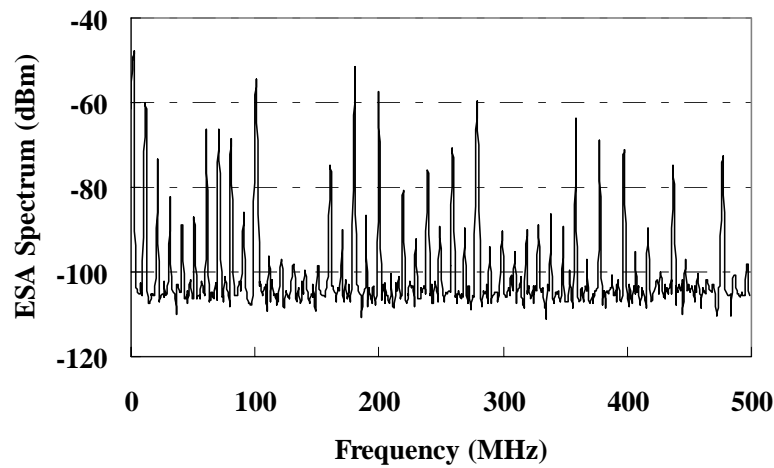
(a)
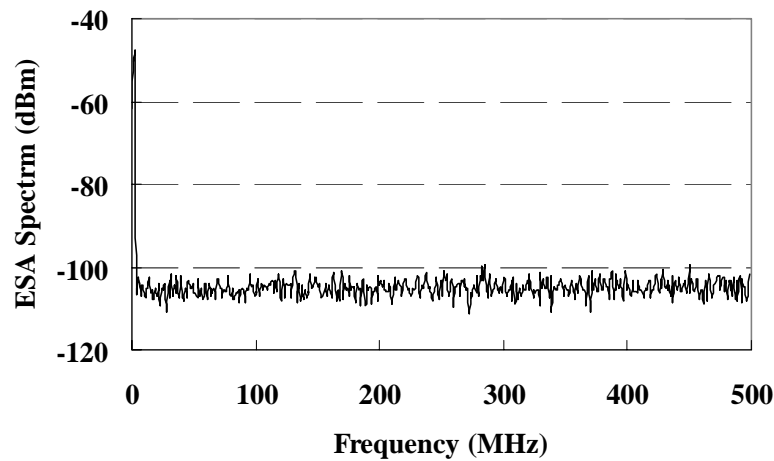
(b)

Fig. 5.14 RF spectrum of the fibre ring laser (a) without and (b) with the saturable absorber

The laser linewidth at this single-longitudinal operation condition was also measured by heterodyning the ring laser with a tunable external cavity laser (manufactured by Agilent).   The measure setup is same as that shown in Figure 4.11 of Chapter 4. Figure 5.15 shows the beating tone generated by these two lasers and the Inset of Figure 5.15 shows the expanded spectrum.   The linewidth of the fibre ring laser is

measured to about 280 kHz, which is limited by ~ 300-kHz linewidth of the external

cavity laser.   The actual linewidth of the fibre ring laser should be much narrower

than this value.
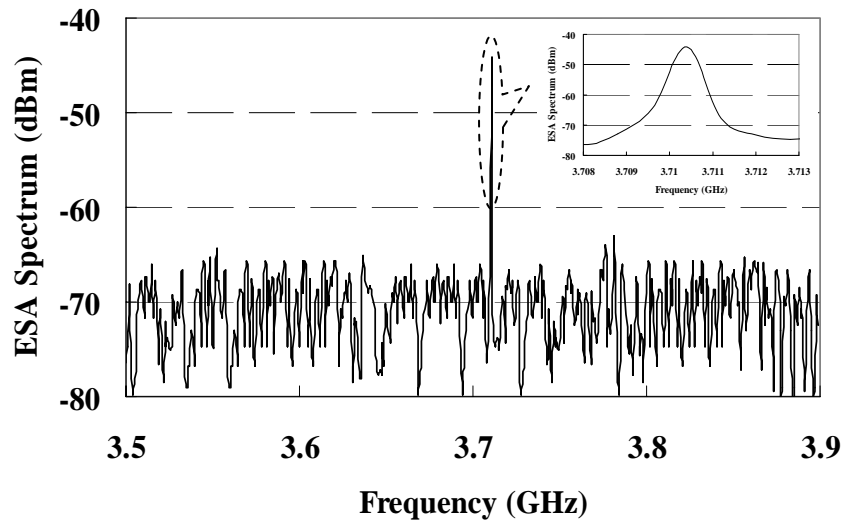
Fig. 5.15   Measured laser linewidth of the single-longitudinal mode fibre ring laser

Since no narrower linewidth tunable laser source can be available, we use the delayed

self-heterodyne technique to measure the linewidth of the fibre ring laser.   By using

the two diffracting beam outputs of the acousto-optic frequency shifter (AOFS), the

delayed self-heterodyne method can be simplified to Figure 5.16.   The 1st order

diffracting beam will have the frequency shifter and the power is higher than the zero

order transmitted beam.   The 25 km delayed fibre is placed in the path of the 1st

order diffracting beam and the polarization controller (PC) is placed in the path of the

zero order diffracting beam.   The two beams are combined by a 3-dB coupler and

detected by 1 GHz photodiode detector which is connected to an RF electrical

spectrum analyzer.
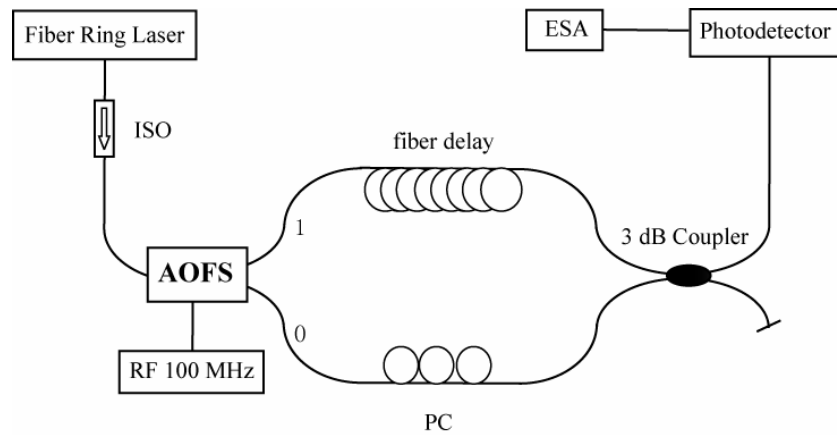
Fig. 5.16   Configuration of the self-heterodyne laser linewidth measurement

A typical linewidth measurement result of the single-longitudinal mode fibre ring laser is shown in the Figure 5.17, which is the result of 10 average spectra. Assuming that the laser spectrum is Lorentzian-shaped, the 3-dB linewidth of the fibre ring laser is about 1.17 kHz, which is calculated from the 7 kHz of the 10-dB linewidth from Figure 5.17 using the relationship shown in the Table 4.1 of Chapter 4.

Fig. 5.17   Measured laser linewidth of the single-longitudinal mode fibre ring laser

5.4   Chapter Summary

In this chapter, the advantages of Bi-EDF, especially over Si-EDF, were explained. Due to the large difference with SMF in refractive index and numerical aperture, special fusion angle splicing between Bi-EDF and SMF is theoretically analyzed. A high numerical aperture fibre is added between Bi-EDF and SMF to provide better mode field diameter matching to achieve low insertion loss, small PDL and high reflection loss connection.

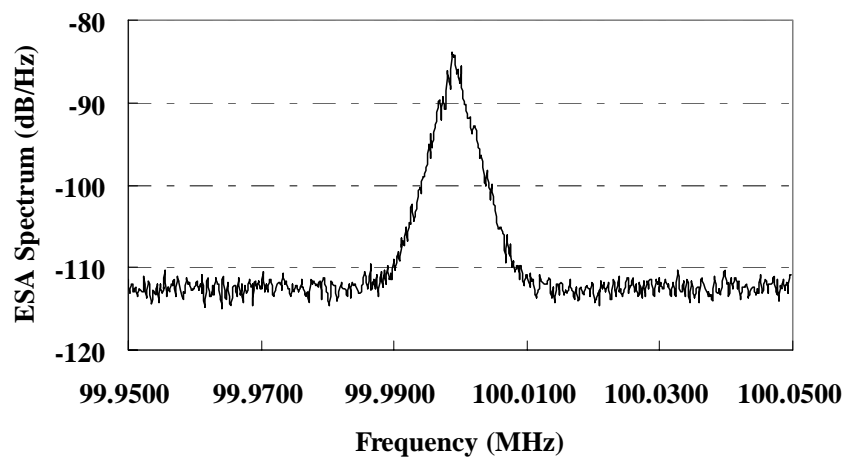Then a short-cavity fibre ring laser by employing only 84.6-cm long Bi-EDF and a broad wavelength tunable MEMS-based filter was demonstrated. Ultra-wide continuous wavelength tuning of up to 106 nm was obtained. A second laser output extracted from a 20% taper in the laser cavity exhibits very high extinction ratio of better than 60 dB but with much lower output power and slightly reduced tuning range of 104 nm. A scanning fibre Fabry-Perot filter with 61 nm FSR combined with C-/L-band WDM filter in place of the MEMS filter to construct a tunable fibre ring laser was also investigated. Large tunable range of over 100 nm was attained.

To obtain narrower linewidth, a single-longitudinal mode operation laser was also demonstrated by using a 2.5-m unpumped Si-EDF as saturable absorber. The linewidth of the fibre ring laser was measured by two optical mixing methods and 1.17 kHz linewidth was measured with the delayed self-heterodyne technique.

References

1. A. Bellemare, M. Karásek, C. Riviere, F. Babin, G. He, V. Roy, and G. W. Schinn, "A broadly tunable erbium-doped fiber ring laser: experimentation and modeling," *IEEE J. Select. Topics Quantum Electron.*, vol. 7, no. 1, pp. 22-29, Jan. 2001.

2. X. Dong, P. Shum, N. Q. Ngo, C. C. Chan, B. O. Guan, and H. Y. Tam, "Effect of active fiber length on the tunablility of erbium-doped fiber ring lasers," *Opt. Express*, vol. 11, no. 26, pp. 3622-3627, Dec. 2003.

3. X. Dong, N. Q. Ngo, P. Shum, B. O. Guan, H. Y. Tam and X. Dong "Concentration-induced nonuniform power in tunable erbium-doped fiber lasers," *Opt. Lett.*, vol. 29, no. 4, pp. 358-360, Feb. 2004.

4. N. Sugimoto, Y. Kuroiwa, K. Ochiai, S. Ohara, Y. Fukasawa, S. Ito, S. Tanabe, and T. Hnnada, "Novel short-length EDF for C+L band amplification", *OAA2000 Technical Digest*, Canada, post-deadline paper PD-3, 9-12 Jul. 2000.

5. S. Y. Set, M. Jablonski, T. Kotake, K. Furuki, M. Tojo, Y. Tanaka, N. Sugimoto, K. Kisuchi, "Low Nonliearity Bismuth Oxide-based Erbium-doped Fiber Amplifiers for Short Pulse Amplification", *OFC 2003*, Atlanta, Georgia, paper PL2, Mar. 2003.

6. N. Sugimoto, "Ultrafast optical switches and wavelength division multiplexing (WDM) amplifiers based on Bismuth oxide glasses," *J. Am. Ceram. Soc.*, vol. 85, no.5, pp. 1083-1088, May 2002.

7. http://www.agc.co.jp/english/biedf/bi5web.pdf

8. H. Sotobayashi, J. T. Gopinath, and E. P. Ippen, "23cm long Bi_2O_3-based EDFA for picosecond pulse amplification with 80 nm gain bandwidth", *Electron. Lett.*, vol. 39, no.19, pp. 1374-1375, Sep. 2003.

9. N. Sugimoto, T. Nagashima, T. Hasegawa, and S. Ohara; "Bismuth-based optical fiber with nonlinear coefficient of 1360 $W^{-1}km^{-1}$", *OFC 2004*, Los Angeles, New York, paper PDP26, Feb. 2004.

10. E. Hecht, Optics (Third Edition), Addison Wesley, New York, 1998.

11. N. Kishi, and T. Yazaki, "Frequency Control of a Single-Frequency Fiber Laser by Cooperatively Induced Spatial-Hole Burning", *IEEE Photon. Technol. Lett.*, vol. 11, no. 2, pp. 182-184, Feb. 1999.

Chapter **6**

Wavelength-switchable Fibre Ring Laser

6.1   Introduction

Ultrawide wavelength-tunable fibre ring laser were introduced in Chapter 5.   Due to the need of continuous wavelength tunable outputs in many applications such as sensing and optical component characterization, the filter used in ring cavity must be continuously tunable.   However, in certain applications such as DWDM systems, a discrete-wavelength tunable laser is sufficient.   In this case, less costly filters can be used to realize wavelength-switchable fibre ring lasers.

Different filter devices including cascaded fibre Bragg grating (FBG) cavities [1], FBG written in birefringent fibre [2], long-period fibre grating written in polarization maintaining fibre [3] and Sagnac loop reflector [4], have been used to realize the oscillating wavelength switching in the fibre laser.   However, all these reported lasers require additional wavelength selective elements that match the switchable-wavelengths of the laser, therefore, the configuration of these lasers are complicated and hence, the number of switchable wavelengths is also limited.

In this chapter, we present new kinds of wavelength-switchable fibre ring laser using the polarization wavelength selection principles. The theoretical background of polarization wavelength selection, which is essential to understand the wavelength selection mechanism in a switchable fibre ring laser, will be explained. Then two new kinds of wavelength-switchable fibre ring laser are present. The first laser is based on an unbiased Fabry-Perot laser diode (FP-LD) and its output can be switched between 8 different wavelengths with 1.1 nm spacing. The second laser design consist of a Fabry-Perot etalon filter, a polarizer, a programmable electric-actuated polarization controller and its output can be switched between 35 different wavelengths from 1545 to 1573 nm with 0.8 nm spacing. Wavelength switching of the two kinds of wavelength-switchable lasers was achieved by suitably changing the polarization state inside the cavity.

6.2   Polarization Wavelength Selection in Wavelength-switchable Laser

In this section, the theoretical background of polarization wavelength selection will be explained based on the Jones matrix calculus [5, 6].

6.2.1   Principle of Polarization Wavelength Selection

The light propagation in ring laser cavity can be represented by a system shown in

Figure 6.1. It includes two polarizers (to represent the effect of one polarizer in the ring cavity), one polarization controller, one fibre with birefringence index due to fibre bend and one etalon filter. The first four optical devices together behave as an "etalon filter" whose FSR depends on the fibre length [7, 8] and is different from the real etalon filter used in the cavity. The two etalon filters with different FSR combine together forming a narrow bandpass filter. The peak wavelengths of the first "etalon" can be altered by adjusting the polarization state of the polarization controller. Consequently, the combination of the first "etalon" and the second etalon formed a wavelength-switchable filter with its peak wavelength located at one of the transmission peaks of the second etalon filter.
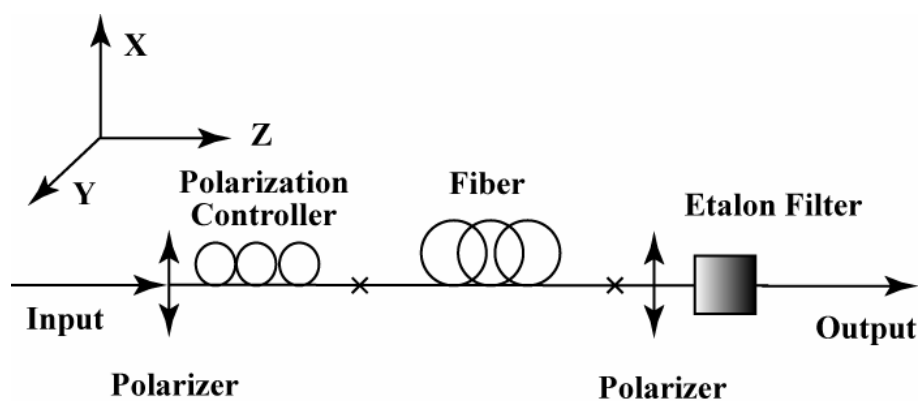

Fig. 6.1   Schematic diagram to illustrate the principle of polarization wavelength selection.

6.2.2   Jones Matrix Analysis of Polarization Wavelength Selection

We assume that the optical axis of the polarizer is align to the x-axis, i.e. the polarization of output light after passing through the polarizer is linear polarized in the

x-direction. The two polarizers shown in Figure 6.1 are actually the same polarizer and thus their optical axes are parallel. For x direction linear polarizer, its Jones transition matrix can be written as:

$$\mathbf{J}_{LPx} = \begin{pmatrix} 1 & 0 \\ 0 & 0 \end{pmatrix}. \tag{6.1}$$

The polarization controller used in Figure 6.1 consists of two quarter waveplates and one half waveplate as shown in Figure 6.2. This type of polarization controller can transform any arbitrary input state of polarization (SOP) into any arbitrary output SOP [9, 10]. All the waveplates are endlessly rotatable, and Fred Heismann shown that endless polarization transformations between any two general polarization states can be achieved by rotating the second QWP synchronously with the first QWP in the crossed position, i.e. $\delta = 90^0$, as shown in Figure 6.2 [11, 12]. This offset reduces the number of control variables, while still providing access to all polarization states. In Figure 6.2, although any angle is possible for θ_1, its functional range is from 0° to 180°. Similarly, the functional range for θ_2 and δ is from 0° to 180°.
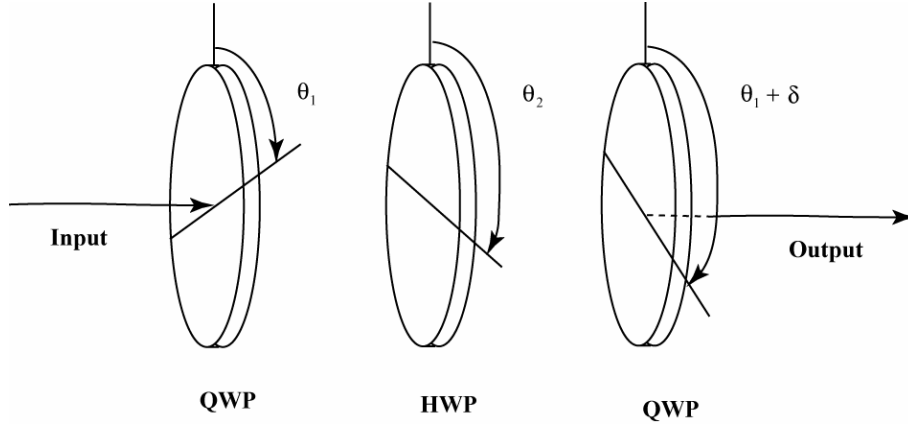
Fig. 6.2   Operation of a 3-waveplates polarization controller.

Consider a waveplate with its fast axis aligned at an angle θ with the x-axis, its Jones transition matrix can be written as: [6]

$$
\begin{aligned}
J_{WP} &= \begin{pmatrix} \cos\theta & -\sin\theta \\ \sin\theta & \cos\theta \end{pmatrix} \begin{pmatrix} e^{j\Delta\varphi/2} & 0 \\ 0 & e^{-j\Delta\varphi/2} \end{pmatrix} \begin{pmatrix} \cos\theta & \sin\theta \\ -\sin\theta & \cos\theta \end{pmatrix} \\
&= \begin{pmatrix} e^{j\Delta\varphi/2}\cos^2\theta + e^{-j\Delta\varphi/2}\sin^2\theta & (e^{j\Delta\varphi/2} - e^{-j\Delta\varphi/2})\sin\theta\cos\theta \\ (e^{j\Delta\varphi/2} - e^{-j\Delta\varphi/2})\sin\theta\cos\theta & e^{j\Delta\varphi/2}\sin^2\theta + e^{-j\Delta\varphi/2}\cos^2\theta \end{pmatrix} \\
&= \begin{pmatrix} \cos(\Delta\varphi/2) + j\sin(\Delta\varphi/2)\cos 2\theta & j\sin(\Delta\varphi/2)\sin 2\theta \\ j\sin(\Delta\varphi/2)\sin 2\theta & \cos(\Delta\varphi/2) - j\sin(\Delta\varphi/2)\cos 2\theta \end{pmatrix}
\end{aligned}
\quad , \quad (6.2)
$$

where $\Delta\varphi$ is the total phase shift between the fast and slow axes of the waveplate [6]. A phase shift of 360 degrees retards the slow axis by one wavelength with respect to the fast axis.   Equation 6.2 can be used to model quarter waveplate and half waveplate by setting the phase shift angle to 90 degrees and 180 degrees, respectively. The Jones transition matrix of quarter-wave plate and half-wave plate can be written, respectively, as:

$$J_{QW}(\theta) = \begin{pmatrix} \dfrac{1}{\sqrt{2}} + \dfrac{j}{\sqrt{2}}\cos 2\theta & \dfrac{j}{\sqrt{2}}\sin 2\theta \\[4mm] \dfrac{j}{\sqrt{2}}\sin 2\theta & \dfrac{1}{\sqrt{2}} - \dfrac{j}{\sqrt{2}}\cos 2\theta \end{pmatrix} \text{, and} \qquad (6.3)$$

$$J_{HW}(\theta) = \begin{pmatrix} j\cos 2\theta & j\sin 2\theta \\ j\sin 2\theta & -j\cos 2\theta \end{pmatrix}. \qquad (6.4)$$

Using Equation 6.3 and Equation 6.4, the Jones transition matrix of the polarization controller shown in Figure 6.2 can be written as:

$$\begin{aligned} \mathrm{J}_{PC} &= J_{QW}(\theta_1 + \delta)J_{HW}(\theta_2)J_{QW}(\theta_1) \\ &= \begin{pmatrix} A + jB & C - jD \\ -C - jD & A - jB \end{pmatrix} \\ &= \begin{pmatrix} \cos\theta' e^{j\phi_1'} & \sin\theta' e^{-j\phi_2'} \\ -\sin\theta' e^{j\phi_2'} & \cos\theta' e^{-j\phi_1'} \end{pmatrix} \end{aligned} \qquad (6.5)$$

where $A = -\cos\gamma\cos\delta$, $B = \sin\gamma\sin(2\theta_1 + \delta)$, $C = -\cos\gamma\sin\delta$,

$D = \sin\gamma\cos(2\theta_1 + \delta)$, $\gamma = 2\theta_1 - 2\theta_2 + \delta$, $\theta' = \arccos(\sqrt{A^2 + B^2})$,

$\phi_1' = \arccos(A/\sqrt{A^2 + B^2})$, and $\phi_2' = \arccos(C/\sqrt{C^2 + D^2})$.

From Equation 6.5, we can see that the polarization controller can change the amplitude and phase difference between the two orthogonal polarizations of input SOP. $\Delta\phi' = \phi'_1 - \phi'_2$ is the phase shift between the wave components in the two orthogonal x- and y-axes. $\cos\theta'$ and $\sin\theta'$ are the splitting ratio to x- and y-axes, respectively.

In Figure 6.1, we assume the fibre has a beat length of L_b and the fast fibre optical axis is aligned at an angle θ_3 with the x-direction, so its Jones transition matrix can be written as:

$$\mathbf{J}_{fiber} = \begin{pmatrix} \cos\theta_3 & -\sin\theta_3 \\ \sin\theta_3 & \cos\theta_3 \end{pmatrix} \begin{pmatrix} e^{j\Delta\phi/2} & 0 \\ 0 & e^{-j\Delta\phi/2} \end{pmatrix} \begin{pmatrix} \cos\theta_3 & \sin\theta_3 \\ -\sin\theta_3 & \cos\theta_3 \end{pmatrix},$$ (6.6a)

where $\Delta\phi$ is the linear phase shift between two main orthogonal polarization components and can be expressed as:

$$\Delta\phi = 2\pi(1 - \frac{\Delta\lambda}{\lambda_s})\frac{L}{L_b}.$$ (6.6b)

Therefore the total transformation is given by:

$$\mathbf{J}_{total} = \mathbf{J}_{LPx}\mathbf{J}_{fiber}\mathbf{J}_{PC}\mathbf{J}_{Lpx}$$
$$= \begin{pmatrix} \cos(\theta' + \theta_3)\cos\theta_3 e^{j(\phi_1' + \Delta\phi/2)} - \sin(\theta' + \theta_3)\sin\theta_3 e^{j(\phi_2' - \Delta\phi/2)} & 0 \\ 0 & 0 \end{pmatrix}.$$ (6.7)

Consequently, the total power transmission, T, of the cavity is given by

$$|T|^2 = \cos^2(\theta' + \theta_3)\cos^2\theta_3 + \sin^2(\theta' + \theta_3)\sin^2\theta_3$$
$$+ \frac{1}{2}\sin 2(\theta' + \theta_3)\sin 2\theta_3 \cos(\Delta\phi + \Delta\phi').$$ (6.8)

6.2.3 Explanation of the Polarization Wavelength Selection

From Equation 6.8, one can see that the power transmission of the laser cavity depends on the phase shift between the two polarization components introduced by the polarization controllers and the fibre birefringence. The peak transmission depends on the $\theta' - \theta_3$ and θ_3. Since the phase shift is different for different wavelengths, as indicated in Equation 6.6b, different wavelength has different power transmission in the cavity when all the optical devices are fixed. Figure 6.3 shows the curves of optical power transmission versus wavelength shift $\Delta\lambda$ for different L/L_b at fixed polarization, for example, $\Delta\phi' = 0$, $L/L_b = 0.1$. It shows that the linear system transmission is a periodic function of $\Delta\lambda$, which is the same as the FSR of the etalon filter. The period of the system transmission can be changed with L/L_b and the shorter length of fibre will have larger FSR.
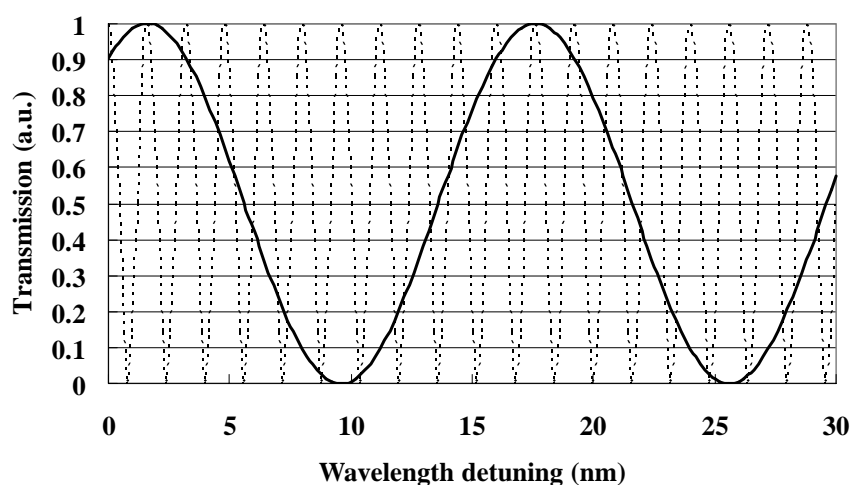

Fig. 6.3   System transmission of the ring cavity versus wavelength detuning (solid line for $L/L_b=1$ and dotted line for $L/L_b=0.1$).

For ease of explanation, in the case of fixed L/L_b, we assume the polarization controller does not change the splitting ratio of the orthogonal polarization components but only induces a phase shift, $\Delta\phi'$, between them, and would shift their peak wavelengths as shown in Figure 6.4 (a). Therefore, if a different FSR etalon filter is added in the setup, under different phase shift of the polarization controller, then different single wavelength, which is the peak wavelength in both filter spectrums, will be selected, as shown in Figure 6.4 (b).
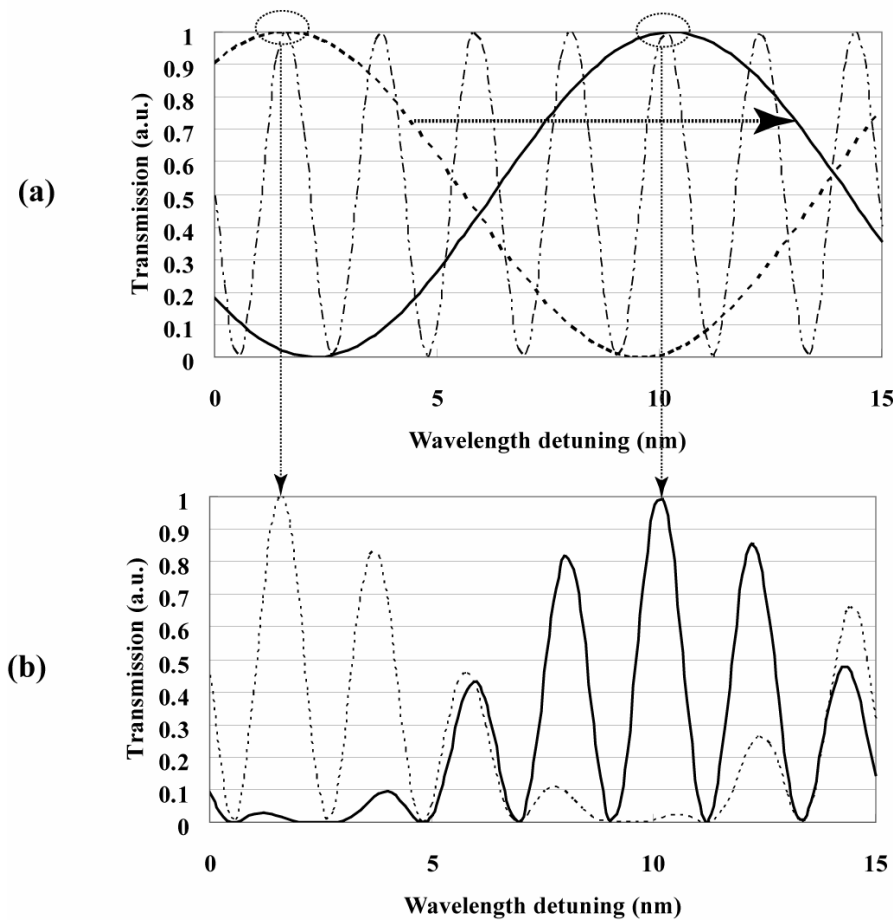

Fig. 6.4   Operation principle of the polarization wavelength selection.

6.3   Wavelength-switchable FRL Using the Unbiased FP-LD

As explained in Section 6.2.3, polarization wavelength selection requires the polarization effect plus etalon or Fabry-Perot cavity.   Fortunately, FP-LD possesses both functions.   Since the FP-LD consists a linear gain cavity with a pair of end mirrors, which act as an F-P etalon filter.   The output spectrum of the FP-LD can be seen as the etalon filter spectrum plus optical gain of the device materials, as shown in Figure 6.5 [13].
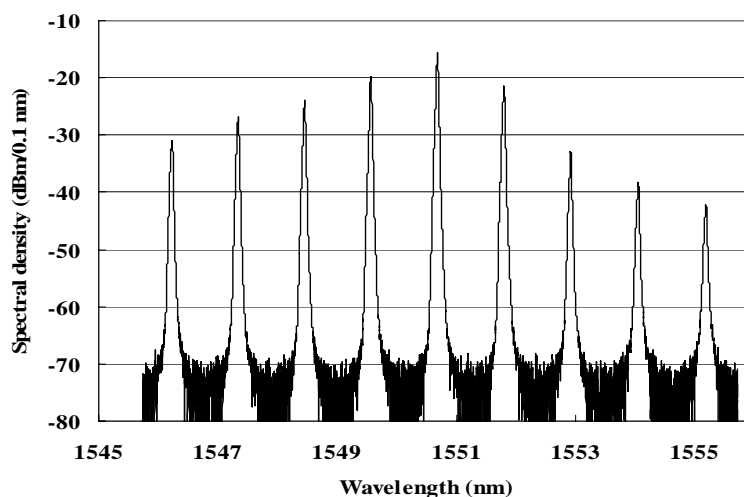

Fig. 6.5   Typical spectrum of a FP-LD.

The double-channel planar-buried heterostructure of FP-LD favors the TE mode and the power of the TM mode is less than 0.1% [14].   Figure 6.6 (a) and (b) show the output spectra of the FP-LD when injected by a TE and a TM polarized signal, respectively.   The minimum and maximum loss occurs when the injected signal is

spectrally aligned with a longitudinal mode of the FP-LD in TE and TM mode, respectively. Therefore, for any injected signal that is spectrally aligned with a wavelength at which the TE and the TM modes of the FP-LD coincide, the TE component of the injected signal will be amplified with its intensity clamped and stabilized by injection locking if the power of the TE component is above the injection-locking threshold. The TM component, however, is always suppressed. As a result, an injection-locked FP-LD acts as a linear polarizer [14], only allowing TE-polarized light to pass through, as well as an etalon spectral filter.
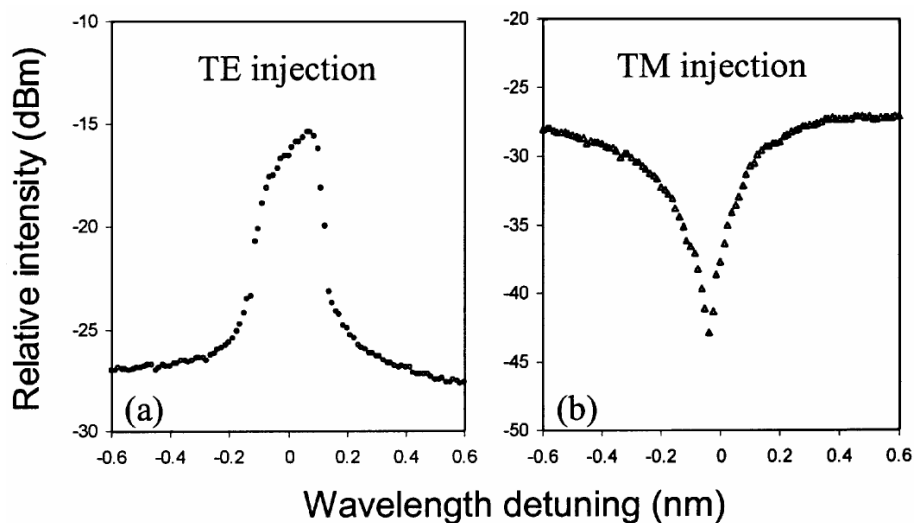

Fig. 6.6   The output spectra of FP-LD when injected with laser light of different wavelengths. (a) TE polarized. (b) TM-polarized CW signal [14].

6.3.1   Experimental Setup

Figure 6.7 shows the experimental configuration of the wavelength-switching fibre ring laser using an unbiased FP-LD. An 11-m long silica-based erbium-doped fibre

(Si-EDF) was employed as the gain medium. The peak absorption of the EDF at 980 nm and 1530 nm are 4.8 and 6.7 dB/m, respectively. The EDF was backward-pumped by one 980 nm semiconductor laser via the 980 nm port of a wavelength-division multiplexer (WDM) constructed with fused taper fibre. The optical circulator in the cavity couples light to the unbiased FP-LD via port 2 and then couples light from the FP-LD back to the cavity via port 3. The optical circulator also ensured unidirectional operation of the ring cavity. The polarization controller was used to adjust the polarization state of the light in the fibre laser to inject into the unbiased FP-LD to select the different lasing wavelengths. The lasing output of the fibre laser was obtained from a 3-dB fused fibre coupler inserted in the fibre laser cavity. An optical spectrum analyzer (OSA) and a polarization analyzer (PA) were used to record the laser output and the states of polarization (SOP) for different tunable lasing wavelengths.
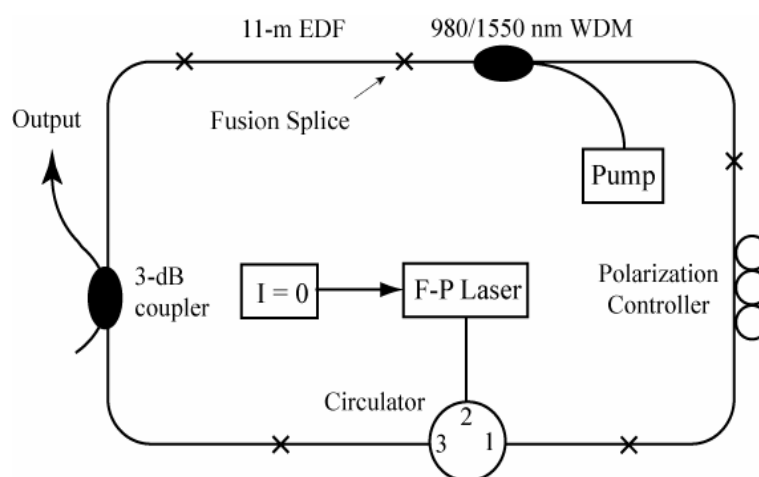

Fig. 6.7   Configuration of the switchable fibre ring laser with an unbiased FP-LD.

6.3.2 Performance and Discussions

Figure 6.8 shows the superimposed output spectra of the fibre ring laser using an unbiased FP-LD at eight different polarization states by adjusting the polarization controller. The spectra were measured with an optical spectrum analyzer (OSA) with 0.1 nm resolution. The fibre ring laser was pumped with 100 mW of optical power and only single wavelength is excited in this pump power level. If the pump power is lower, the laser cannot be excited because of insufficient gain. On the other hand, if the pump laser diode power is too large, many FP-LD modes will be excited, and multi-wavelength lasing will occur. In our experiment, the threshold of FP-LD is about 11 mA and the FP-LD was temperature stabilized at 22 °C, to prevent wavelength drift.

The unbiased FP-LD, which acts as a linear polarizer [14] and an etalon filter, strongly favours light that is TE-polarized and with wavelength that matches one of the etalon's FP modes. The combination of the polarization controller (PC) and the FP-LD serve as the wavelength selection device in the lasing cavity. Wavelength separation between the different wavelengths at different polarization states depends on the FP-LD mode spacing which in our case is 1.1 nm. According to the polarization wavelength selection principle, the wavelength-dependent cavity loss is determined by the fibre bend birefringence and the scalar product polarization state of

all the optical devices in the cavity. Therefore, the light with its wavelength close to one of the longitudinal modes of the FP-LD and its TE-polarization component experience the least loss will lase. If the polarization state of the PC is changed, the wavelength-dependent cavity loss will change and a different wavelength which is close to a different FP-LD longitudinal mode and its TE-polarization component experience the least loss will lase, resulting in wavelength switching in the laser output.
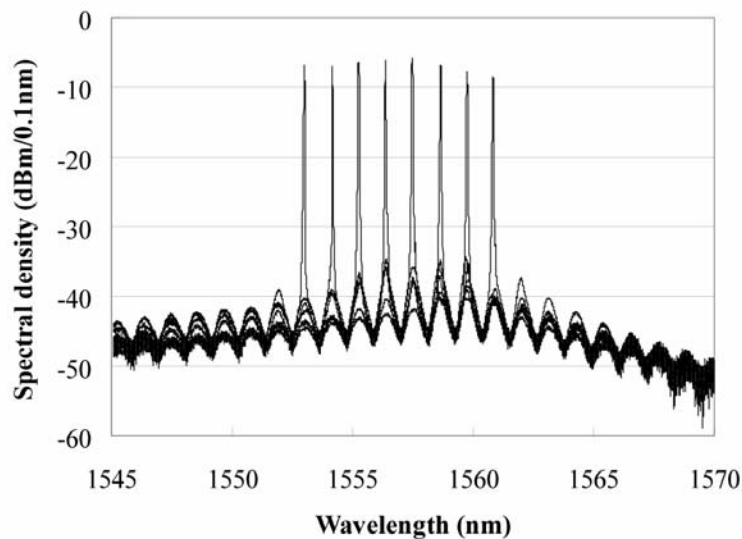
Fig. 6.8   Superimposed output spectra of the eight lasing wavelengths.

Laser with output switches among eight different wavelengths spaced at 1.1 nm apart (from 1552.98 nm to 1560.84 nm) was achieved by varying the polarization controller. The number of lasing wavelengths is limited by the gain profile of the ring cavity which is mainly determined by the EDF and the insertion loss of unbiased FP-LD. The output power is about -7 dBm and the SMSR of this fibre ring laser is larger than

30 dB.   The measured 3-dB linewidth of this fibre ring laser using an OSA with 0.01 nm resolution is about 0.02 nm.   The polarizations of the laser outputs corresponding to the eight lasing wavelengths were measured with a polarization analyzer and displayed in Poincaré sphere profile as shown in Figure 6.9.   Due to the polarization introduced by the optical path between the output of the FP-LD and the input of the polarimeter is fairly constant during the measurement period (this is confirmed by the relatively small size of the spot on the Poincaré sphere), the results show that eight polarization states were injected into the FP-LD to produce the eight different lasing wavelengths.   The polarizations in Figure 6.9 show the stable polarization operation for different lasing wavelengths and the results is not a point which is mainly due to the vibration of the test environment and the non-polarization maintained coupler whose polarization is sensitive to wavelength.   Two other important parameters that determined the performance of the laser are wavelength stability and output power stability.
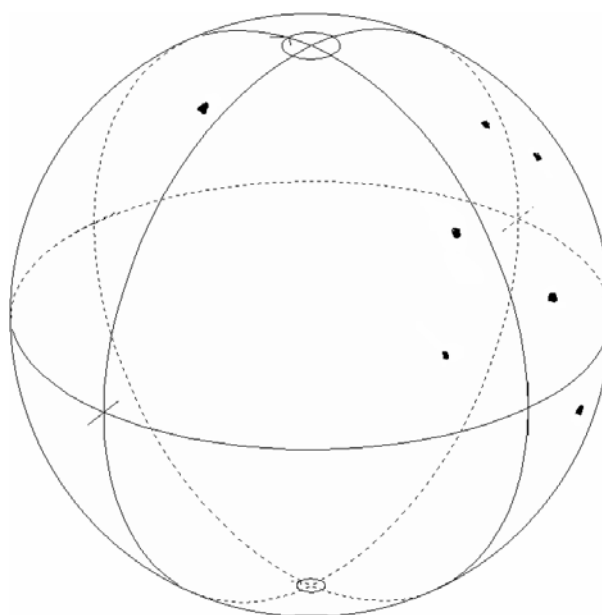

Fig. 6.9   Measured polarization states of the eight different output lasing wavelengths.

Figure 6.10 shows the measured wavelength variation and the peak power fluctuation of the fibre laser when its output was switched and maintained at one lasing wavelength for a period of 2 hours. The wavelength fluctuation is about 0.03 nm, measure with an OSA with 0.01 nm resolution and the peak power fluctuation is about 0.8 dB.
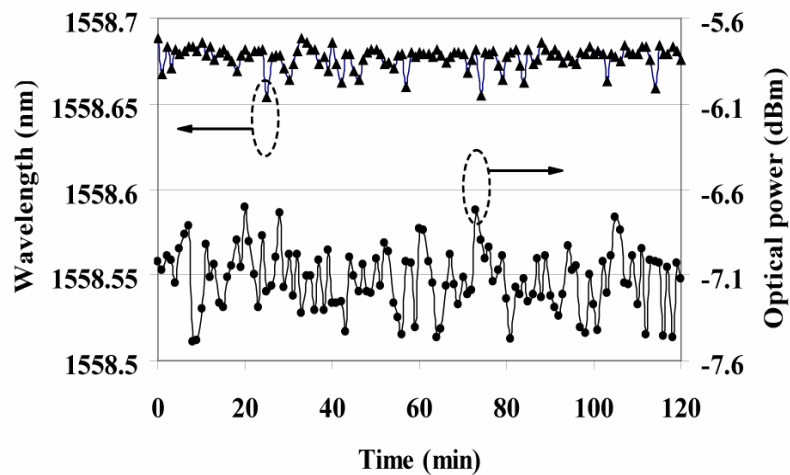
Fig. 6.10 Measured wavelengths and peak power fluctuation of the fibre ring laser over 2 hours.

6.4 Wavelength-switchable FRL Using Polarizer and F-P Etalon Filter

Due to the large insertion loss of the unbiased FP LD, the output power is low. In addition, because of the pair-induced quenching and clustering effects occurring in silica-based erbium-doped fibres (Si-EDF) [15], much longer length of Si-EDF, about 11 m, is required in the construction of switchable fibre ring laser. However, bismuth oxide-based glass fibre can extend the distance between erbium ions and

reduce the concentration quenching significantly [16], only a short length of bismuth

oxide based erbium-doped fibre (Bi-EDF), less than 1 m, is enough because of higher

concentration of erbium ions in Bi-EDF.

In the following section, we present a new kind of wavelength-switchable fibre ring

laser whose output can be switched between 35 different wavelengths in the range

from 1545 to 1573 nm with a 0.8 nm spacing using only a Fabry-Perot etalon filter, a

polarizer, a programmable electric-actuated polarization controller and a short length

of Bi-EDF.   The Bi-EDF used in the ring laser is about 84.6-cm long and doped with

very high concentration of erbium ions due to negligible ion quenching effect.

Wavelength switching of the laser is achieved by suitably changing the polarization

state inside the cavity, since no additional component is required, fast switching speed

and excellent wavelength stability are demonstrated.

6.4.1   Experiment Setup

Figure 6.11 shows the configuration of the wavelength-switchable Bi-EDFRL.   The

Bi-EDF is pumped by one 1480 nm semiconductor laser diode via port 1 of the

circulator, which exhibits a fairly flat pass-band in the wavelength range from 1460

nm to 1630 nm.   The length of the La-codoped Bi-EDF was 84.6 cm long.   The

erbium concentration in the Bi-EDF is 6,470 wt-ppm and the La concentration is 4.4

%wt.   The peak absorption of the Bi-EDF at 1480 nm and 1530 nm are 167 and 267

dB/m, respectively. Both ends of the Bi-EDF was first angle spliced to high numerical aperture fibre (Corning HI980) before splicing to port 2 (SMF-28 fibre) of the circulator and to the signal port (SMF-28 fibre) of the isolator, providing better mode field diameter matching. The splicing loss attained was less than 0.2 dB for the angled splices. The angled splices reduce the reflection in the laser cavity to less than 60 dB. The F-P etalon filter used in the configuration has a free spectral range of 100 GHz. The insertion loss and bandwidth of the wavelength peaks of the etalon filter are less than 1 dB and about 0.1 nm, respectively. The linear polarizer and the programmable polarization controller are employed to switch the lasing wavelengths. The programmable polarization controller of General Photonics$^{®}$ contains three fibre squeezers that are driven by three applied voltage signals and can be programmed separately to alter the birefringence of the fibres and subsequently change the polarization states of the light passing through the fibres. The extinction ratio of the linear polarizer is larger than 30 dB and its insertion loss is less than 1 dB. The circulator (from port 3 to port 2) and the optical isolator were used to ensure unidirectional operation of the fibre ring laser. The 20% port of a fused fibre taper was added to the laser cavity to provide the laser output.
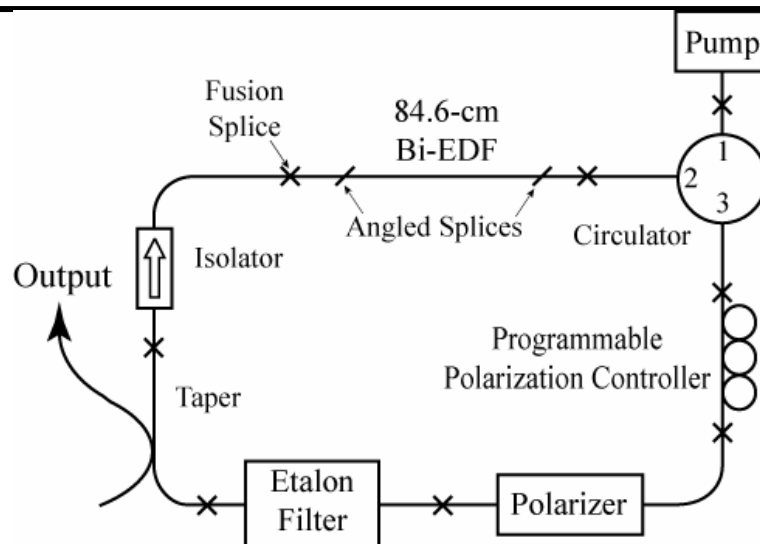
Fig. 6.11   Configuration of wavelength-switchable Bi-EDFRL.

6.4.2   Performance and Discussions

The fibre ring laser was pumped with 67 mW of optical power from a 1480 nm semiconductor pump laser.   By manually adjusting the three voltages applied to the polarization controller, the laser wavelength was switched from about 1545 nm to 1573 nm, exhibiting 35 different wavelengths.   In order to characterize the wavelength-switchable laser, the polarization controller and the OSA were programmed such that each voltage applied to the actuators is increased at a step of 1 V, and the OSA performed a single measurement sweep.   Figure 6.12 (a) shows the superimposed output spectra of fibre ring laser measured by the OSA with 0.1 nm resolution in maximum hold mode.   The measured 3-dB linewidth of this fibre ring laser using the OSA with 0.01 nm resolution is about 0.02 nm, this moderate coherence laser is suitable for test and measurement applications [17].   The output power of the laser is quite uniform across the entire switched wavelength range

(variation less than 3 dB) and has an average value of about 0 dBm.   The laser output

power can be increased by increasing the pump power.   However, if the pump power

is too large, multiple wavelength lasing was observed.   The typical output spectrum

of the fibre ring laser correspond to one applied voltage setting measured with 0.1 nm

resolution is shown in the Figure 6.12 (b).   The side mode suppression ratio (SMSR)

of the laser is greater than 45 dB.

(a)

(b)
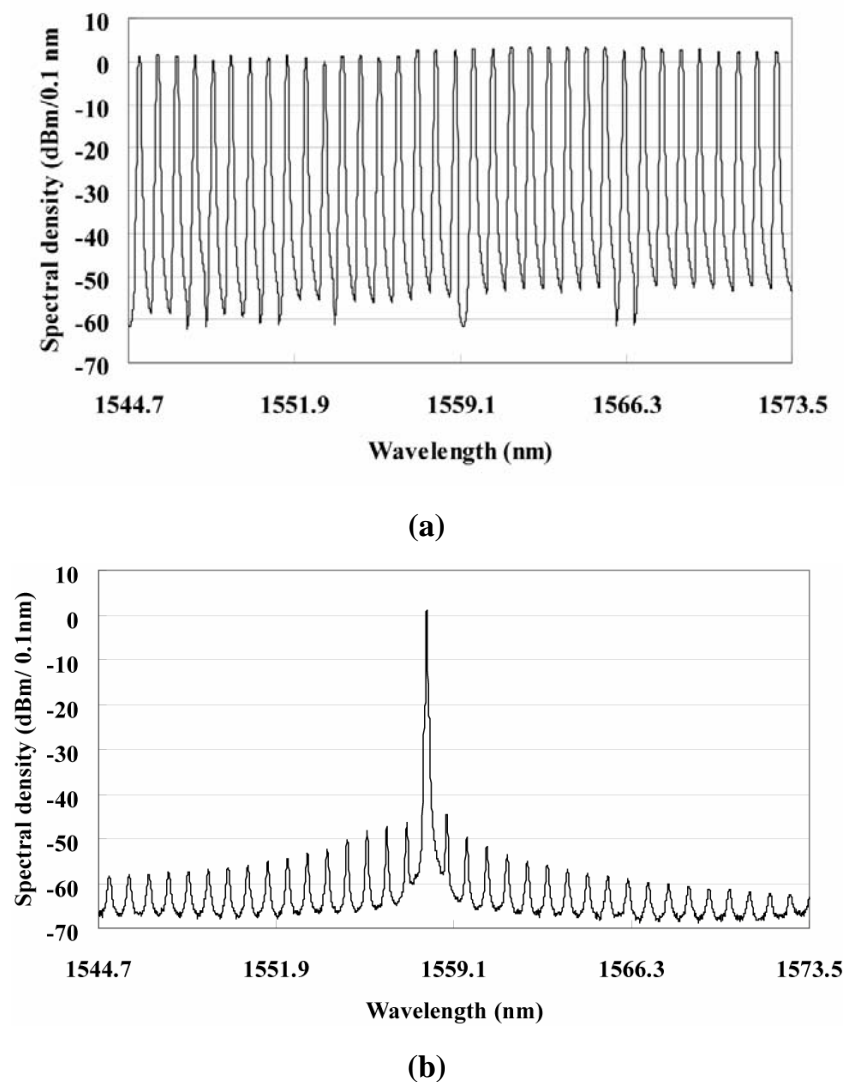
Fig. 6.12   (a) Superimposed output laser spectra (35 lasing wavelengths) measured with an OSA
with 0.1 nm resolution.   (b) One output laser spectrum measured by OSA with 0.1
nm resolution.

The combination of the linear polarizer and polarization controller in the fibre ring laser functions as a wavelength selective element. The lasing wavelength is determined by the peak wavelengths of the F-P etalon filter as well as by the gain bandwidth of the Bi-EDF. The roundtrip loss of the cavity experience by different wavelength mainly depends on the loss of the linear polarizer which is proportional to the scalar product between the polarization of the incoming wavelength beam and the polarization of the polarizer. Therefore, by adjusting the polarization controller, only light having its wavelength matches one of the peaks of the etalon filter and its polarization state most closely aligned to the linear polarizer will lase.

(a)

(b)
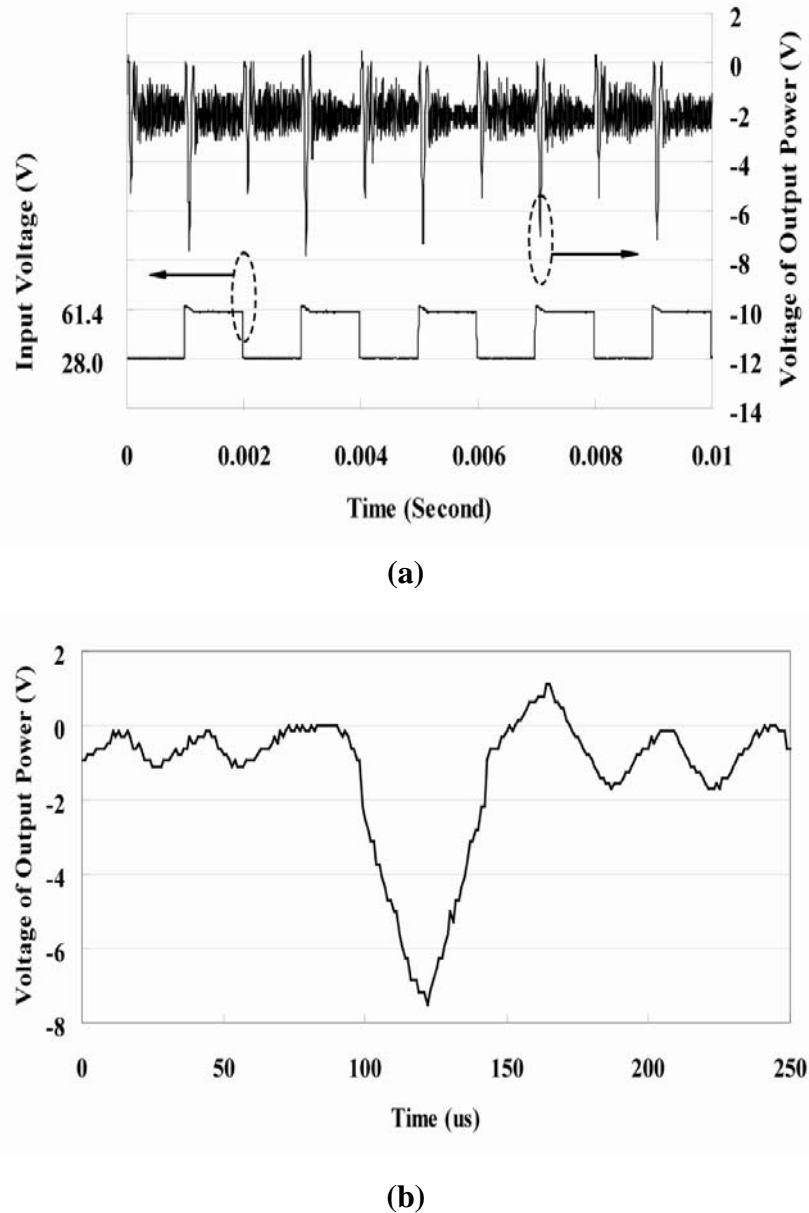
Fig. 6.13　(a) Laser output power variation during wavelength switching.　(b) Expanded view
of relaxation oscillation during wavelength switching.

The wavelength switching speed of the laser was evaluated by applying a 500 Hz

square wave with voltage levels at (28, 0, 0) V and (61.4, 0, 0) V to drive the

polarization controller.　The corresponding lasing wavelengths generated at these

two voltages are 1555.175 nm and 1555.985 nm.　The laser output was monitored by

a 1 GHz photo-detector which was connected to a 200 MHz sampling oscilloscope.

Figure 6.13 (a) shows the voltage generated by the photo-detector under this switching condition; the laser becomes stable after a short period of relaxation oscillation. Figure 6.13 (b) shows that the relaxation oscillation time is around 100 μs, this implied that the maximum switching frequency of the laser is ~10 kHz. The wavelength stability and output power stability of the wavelength-switchable fibre ring laser were also evaluated. Figure 6.14 shows the measured wavelength and power fluctuation of the laser operating at 1561.708 nm for 2 hours. The measured wavelength stability is around 1 pm (display resolution of the OSA). The initial wavelength decrease in the first 10 minutes was due to the warm-up time of the OSA. The power stability was measured to be better than 0.15 dB. It is worth noting that the experiment was conducted under a laboratory environment and no precautions were taken to isolate the setup from thermal and vibration perturbations, therefore better stability is expected if the short-cavity fibre ring laser is properly packaged.
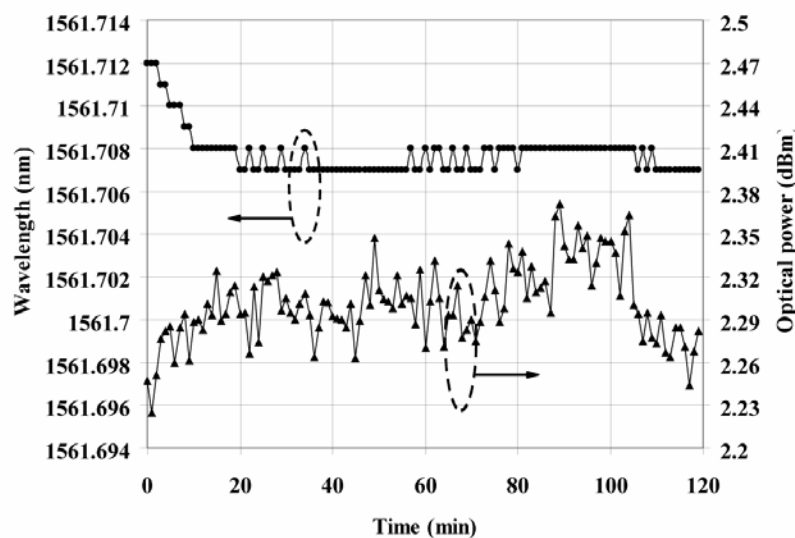

Fig. 6.14   Wavelength and peak power variations of the fibre ring laser versus time over a
2-hour period

6.5 Chapter Summary

In this chapter, the operating principle of polarization wavelength selection is explained with the aid of the Jones matrix approach. In addition, a simple model was proposed to explain the mechanism of polarization wavelength selection.

An Unbiased FP-LD can behave as a polarization as well as an etalon filter. A new and simple fibre ring laser configuration by inserting an unbiased FP-LD in an erbium-doped fibre ring cavity was successfully demonstrated. The laser can switch its output wavelength among one of eight lasing wavelengths in the range from 1552.98 nm to 1560.80 nm with a separation of 1.1 nm, which is defined by the FP mode of the FP-LD. The output power is about -7 dBm and the SMSR of the ring laser was better than 30 dB. The wavelength variation and peak power fluctuation of the relatively long-cavity laser were measured to be about 0.03 nm is about 0.8 dB in a 2-hour stability test.

A short-cavity wavelength-switchable fibre ring laser using bismuth oxide based erbium-doped fibre was also successfully demonstrated. The lasing wavelength can be switched to one of 35 wavelengths in the range of 1545 nm to 1573 nm with a wavelength separation of 0.8 nm. The laser exhibits high output power of about 0 dBm, high SMSR better than 45 dB and output power flatness of 3 dB. The laser is

capable of switching at 10 kHz. Excellent wavelength and power stability of 1 pm

and less than 0.15 dB, respectively, were observed during a 2-hour stability test.

References

1. Q. Mao, and W.Y. Lit John, "Switchable Multiwavelength Erbium-Doped fiber laser with Cascaded Fiber Grating Cavities," *IEEE Photon. Technol. Lett.*, vol. 14, no. 5, pp. 612-614, Nov. 2000.

2. J. Hernandez-Cordero, V.A. Kozlov, A.L.G. Carter, and T.F. Morse, " Fiber Laser Polarization Tuning Using a Bragg Grating in a Hi-Bi Fiber," *IEEE Photon. Technol. Lett.*, vol. 10, no. 7, pp. 941-943, Jul. 1998.

3. Y. W. Lee and B. Lee, "Wavelength-Switchable Erbium-Doped Fiber Ring Laser Using Spectral Polarization-Dependent Loss Element." *IEEE Photon. Technol. Lett.*, vol.15, pp.795-797, 2003.

4. G. Das and W. Y. Lit John, "Wavelength Switching of a Fiber Laser with a Sagnac Loop Reflector," *IEEE Photon. Technol. Lett.*, vol.16, pp.60-62, 2004.

5. E. Collett, Polarized Light: Fundamentals and Applications, Marcel Dekker Inc., New York, USA, 1993.

6. S. Huard, Polarization of Light, Masson, John Wiley & Sons Ltd., West Sussex, UK, 1997.

7. U. Ghera, N. Konforti, and M. Tur, "Wavelength Tunability in a Nd-Doped Fiber Laser with an Intracavity Polarizer," *IEEE Photon. Technol. Lett.*, vol.4, pp.4-6, 1992.

8. W. S. Man, H. Y. Tam, M. S. Demokan, P. K. A. Wai and D. Y. Tang, "Mechanism of intrinsic wavelength tuning and sideband asymmetry in a

passively mode-locked soliton fiber ring laser," *J. Opt. Soc. Am. B.*, vol. 28, pp. 28-33, 2000.

9.   G. R. Walker and N. G. Walker, "Polarization Control for Coherent Communications," *J. Lightwave Technol.*, vol. 8, pp.438-458, 1990.

10. T. Okoshi, "Polarization-State Control Schemes for Heterodyne or Homodyne Optical Fiber Communications," *J. Lightwave Technol.*, vol.3, pp. 1232-1237, 1985.

11. F. Heismann and M. S. Whalen, "Broadband Reset-Free Automatic Polarization Controller," *Electron. Lett.*, vol. 27, pp. 377-379, 1991.

12. F. Heismann, "Analysis of a reset-free polarization controller for fast automatic polarization stabilization in fiber-optic transmission systems," *J. Lightwave Technol.*, vol. 12, pp. 690–699, 1994.

13. H. J. R. Dutton, Understanding Optical Communications, Prentice Hall Ptr., New Jersey, USA, 1998.

14. L. Y. Chan, W. H. Chung, P. K. A. Wai, B. Moses, H. Y. Tam, and M. S. Demokan, "Simultaneous Repolarization of two 10 Gb/s Polarization-scrambled wavelength channels using a mutual-injecion-locked laser diode," *IEEE Photon. Technol. Lett.*, vol.14, pp.1740-1742, Dec. 2002.

15. X. Dong, N. Q. Ngo, P. Shum, B. O. Guan, H. Y. Tam, and X. Dong, "concentration-induced nonuniform power in tunable erbium-doped fiber lasers," *Opt. Lett.*, vol. 29, no. 4, pp. 358-360, Feb. 2004.

16. N. Sugimoto, "Ultrafast optical switches and wavelength division multiplexing

(WDM) amplifiers based on Bismuth oxide glasses," *J. Am. Ceram. Soc.*, vol. 85, no.5, pp. 1083-1088, May 2002.

17. Y. L. Yu, L. F. Lui, H. Y. Tam, and W. H. Chung, "Fiber-laser-based wavelength division multiplexed fiber Bragg grating sensor system," *IEEE Photon. Technol. Lett.*, vol.13, pp. 702-704, July 2001.

<div align="right">

Chapter 7

</div>

Conclusion and Future Work

7.1   Conclusion of the Research Project

This thesis reports the works and results of the investigations on fibre ring lasers with a wide wavelength tuning range and discretely-tunable or wavelength-switchable fibre ring lasers with more switchable wavelengths to cover the ITU wavelength grids of WDM systems.   Three kinds of fibre ring laser configurations, one with wide tunable range of over 100 nm and the other two were discretely-tunable lasers, were investigated theoretically and experimentally.   The basic principle of the operation of the fibre ring lasers and the narrow linewidth measurement techniques of the fibre ring laser were presented.   In addition, novel reflective variable optical attenuators (RVOA) based on fibre coupler and polymer waveguide were also studied and its application in dynamic gain equalization (DGE) of WDM systems was proposed.   A novel low-loss waveguide crossing technique was also proposed for the design of waveguide-based RVOA array which has the potential to integrate to array waveguides, economically.

In the project an entirely new type of bismuth-oxide based erbium-doped fibres were studied for the construction of wide wavelength tunable range fibre ring lasers. Bi-EDF can be highly doped with erbium ions without suffering from pair-induced quenching and clustering effects, just 0.85-m of Bi-EDF was used, resulting in highly stable operation due to its short-cavity. An ultrawide 106 nm continuously tunable Bi-EDF ring laser was achieved with the aids of a tunable MEMS filter. Due to the onset of the nonlinear behaviour of the MEMS filter at low handling optical power, the output power of the ring laser is quite low. High output power was attained by replacing the MEMS filter with a scanning fibre Fabry-Perot filter. Single-longitudinal mode fibre ring laser with very narrow linewidth was realized by using a piece of unpumped EDF which acted as a saturable absorber in the laser cavity. The linewidth of the fibre ring laser was measured by two optical mixing methods and a linewidth of 1.17 KHz was measured by the delayed self-heterodyne technique.

Two kinds of wavelength-switchable fibre ring laser based on polarization wavelength selection were also investigated and demonstrated experimentally. One laser employed an unbiased FP-LD which behaves both as a polarizer and as an etalon filter, and eight lasing wavelengths switching was achieved. The wavelengths of the laser output are from 1552.98 nm to 1560.80 nm with a separation of 1.1 nm, which is defined by the FP mode of the FP-LD. The wavelength variation and peak power fluctuation of the relatively long-cavity laser were about 0.03 nm and 0.8 dB, respectively, in a 2-hour stability test. The second configuration of wavelength-

switchable fibre ring laser employed a short length (about 0.85 m) of Bi-EDF as the gain medium to realize a short cavity. Thirty-five switchable wavelengths were achieved in the range of 1545 nm to 1573 nm with a wavelength separation of 0.8 nm, which is defined by the peaks of an F-P etalon filter. The laser exhibited high output power of about 0 dBm, high SMSR better than 45 dB and output power flatness of 3 dB. The switching frequency of this fibre ring laser was measured to be as high as 10 kHz. Excellent wavelength and power stability of 1 pm and less than 0.15 dB, respectively, were observed during a 2-hour stability test.

In the research of RVOA, two types of RVOA were demonstrated. One type was based on fibre couplers. The measured attenuation range was about 9 dB for the 2-coupler RVOA and about 22 dB for the 3-coupler RVOA as well as for the coupler RVOA with a Faraday rotator mirror. Typical PDL of the fibre coupler RVOAs was about 5 dB, which can be reduced to 0.5 dB by using the configuration with a Faraday rotator mirror. The second type of RVOA investigated in this project was fabricated with polymer waveguide. The negative tone epoxy Novolak resin (ENR) polymer was used as the core waveguide material and UV-cured resin Norland Optical Adhesive 61 (NOA61) polymer was used as the cladding layer material. The design cross section of RVOA was 2.7x2.7 um^2, which support single mode operation, and the total effective area occupied by the RVOA is about 4x7 mm^2. A dynamic range of 15 dB attenuation range was achieved and the PDL was less than 0.2 dB. The measured insertion loss of waveguide was about 18 dB, which was too large and it

was mainly caused by coupling loss, unsmooth edges of waveguide and imperfect position alignment.

In this project, an entirely new design technique based on MMI structure for the construction of low-loss waveguide crossings was proposed. The technique was verified by the two-dimensional beam propagation method. Waveguide crossings designed with the new technique and that with the width taper structure were compared in orthogonal waveguide intersections. Simulation results showed some advantages of the MMI structure technique over the width taper structure technique. The application of MMI structure in small angle intersection, which is crucial for increasing the density of planar lightwave circuits, was also demonstrated and the small angle intersection with low insertion loss can be realized with MMI structure technology.

7.2   Future Work

During the course of this investigation, some promising directions have been identified but could not be followed due to the time limit and the lack of equipment. We have the following suggestions for future work.

1.   Reduce the insertion loss of the polymer waveguide RVOA.

The insertion loss of the designed polymer waveguide RVOA was very high,

which can be reduced by using a taper structure in waveguide design. Moreover, inverse taper structure [1] can also be used to reduce the insertion loss greatly, but high precision fabrication is needed which was not available during the course of the project.

2.   Reduce the effective area of the polymer waveguide RVOA.

The radius of the designed curve waveguides was about 2 mm, which could be reduced if larger refractive index material was used.   The recent emergence of the interest in photonic band-gap (PBG) material suggested that even smaller waveguides could be achieved with this technology.   Linear defects waveguides in PBG can transmit electromagnetic waves efficiently through sharp corners without appreciable losses [2].

3.   Add heat electrode on the top of RVOA waveguide

In this project, the RVOA coupler region was heated through the substrate from the thermoelectric cooler.   This is a slow process and the power consumption is large.   It is more effective and faster if a metalized electrode is deposited on top of the polymer waveguide to heat it directly.

4.   More RVOA integrated with AWG to realize the DGE in one chip.

The ultimate goal of the polymeric RVOA array is integrate them to AWG. Future work on this front would require a good fabrication facility.

5.   Wavelength-switching based on phase-changed device in the cavity.

A polarization controller was used in the laser cavity to realize wavelength-switching, but the polarization controller is difficult to select the wavelength of the laser because the polarization controller varies both the polarization state and phase difference simultaneously.   According to the polarization wavelength selection principle, wavelength switching in fibre ring laser can be realized by the phase change in two orthogonal waves.   It would be more easily to switch the wavelength if a phase-changed device is employed in the cavity.

References

1. V. R. Almeida, R. R. Panepucci and M. Lipson, "Nanotaper for compact mode conversion," *Opt. Lett.*, vol. 28, no. 15, pp. 1302-1304, Aug. 2003.

2. A. Mekis, S. Fan and J. D. Joannopoulos, "Bound states in photonic crystal waveguides and waveguide bends," *Physical Review B*, vol. 58, no. 8, pp. 4809-4817, Aug. 1998.

Appendix I

Publications arising from this Project

1. **Heliang Liu**, Hwayaw Tam, Edwin Pun and P. K. A. Wai, "Research on the Reflective Variable Optical Attenuator," *Regional Inter-University Postgraduate Electrical & Electronic Engineering Conference*, RIUPEEC' Hong Kong, (August 29-30, 2003) Paper B1-4

2. **Heliang Liu**, Hwayaw Tam, W. H. Wong, Edwin Pun and P. K. A. Wai, "Polymeric Reflective Variable Optical Attenuator," *The Fourth IEEE (Hong Kong) AP/MTT and LEOS Postgraduate Conference*, (October 18, 2003) Paper C-4.

3. **Heliang Liu**, Hwayaw Tam, P. K. A. Wai and Edwin Pun, "Low-loss waveguide crossing using a multimode interference structure," *Optics Comm.*, vol. 241, iss. 1-3, pp. 99-104, Nov. 2004.

4. **H. L. Liu**, H. Y. Tam, W. H. Chung, P. K. A. Wai and N. Sugimito, "La-Codoped Bismuth-Based Erbium-Doped Fiber Ring Laser With 80-nm Tuning Range," *ICOCN 2004*, Hong Kong, Nov. 2004.

5. **H. L. Liu**, H. Y. Tam, W. H. Chung, P. K. A. Wai and N. Sugimito, "La-Codoped Bismuth-Based Erbium-Doped Fiber Ring Laser With 106-nm Tuning Range," *OFC 2005*, Anaheim, California, Feb. 2005.

6. **H. L. Liu**, H. Y. Tam, W. H. Chung, P. K. A. Wai and N. Sugimito, "La-Codoped Bismuth-Based Erbium-Doped Fiber Ring Laser With 106-nm Tuning Range," *IEEE Photon. Technol. Lett.*, vol. 17, no. 2, pp. 297-299, Feb. 2005.

7. **H. L. Liu**, H. Y. Tam, W. H. Chung, P. K. A. Wai and N. Sugimito, "Wavelength-switchable Fiber Ring Laser," *CLEO/QELS 2005*, Baltimore, Maryland, May 2005.

8. **H. L. Liu**, H. Y. Tam, W. H. Chung, P. K. A. Wai and N. Sugimito, "Wavelength-switchable La-Codoped Bismuth-Based Erbium-Doped Fiber Ring Laser," *IEEE Photon. Technol. Lett.*, vol. 17, no. 5, pp. 986-988, May 2005.